July 2017

SYNTHESIS, CHARACTERIZATION AND APPLICATION OF BLOCK COPOLYMER AND NANOPARTICLE COMPOSITES

Yue Gai
University of Massachusetts Amherst

SYNTHESIS, CHARACTERIZATION AND APPLICATION OF BLOCK COPOLYMER AND NANOPARTICLE COMPOSITES

A Dissertation Presented

by

YUE GAI

Submitted to the Graduate School of the
University of Massachusetts Amherst in partial fulfillment
of the requirements for the degree of

DOCTOR OF PHILOSOPHY

May 2017

Polymer Science and Engineering

SYNTHESIS, CHARACTERIZATION AND APPLICATION OF BLOCK COPOLYMER AND NANOPARTICLE COMPOSITES

A Dissertation Presented

by

YUE GAI

Approved as to style and content by:

James J. Watkins, Chair

Samuel P. Gido, Member

Jae-Hwang Lee, Member

E. Bryan Coughlin Department Head
Polymer Science and Engineering

DEDICATION

This dissertation is dedicated to my uncle, aunt and their families for their kind and endless support to my strong faith in seeking truth of science.

Also to Mrs. Gao, whose passion in life and teaching reveals the fantastic world for me and enlightens my minds with brave heart and chemistry.

ACKNOWLEDGMENTS

First of all, I would like to acknowledge Professor Watkins for his guidance and support during the last five years. As my advisor, he has been always encouraging me to overcome the difficulties and develop skills in hands-on experimental techniques, professional writing and scientific presentation. His academic network enables me to collaborate with fantastic people of different backgrounds and enrich my view of the polymer study. I also would like to extend my acknowledgements to my committee members Professor Gido and Professor Lee for their invaluable patience, insightful suggestions and inspiring questions.

Appreciations need to be given to lovely Watkins group members for creating wonderful group dynamics and versatile collaborations, specifically to Dr. Ying Lin, Dr. Dong-Po Song, Dr. Xinyu Wang and Dr. Cheng Li for their patience and inspiring discussion at my early Ph.D. stage and great thanks to Benjamin Yavitt, Dr. Huafeng Fei, Irene Howell, Feyza Dundar and Shengkai Li for their constructive suggestions.

I would like to recognize the contribution from my collaborators for their time and work, specifically to Professor Robert A. Norwood, Dr. Palash Gangopadhyay and Alexander Miles from University of Arizona for their expertise in material optical response, enriching my knowledge other than polymer; and to Professor H. Henning Winter for his expertise in polymer rheological studies.

At the same time, I would like to appreciate all professors and staffs in PSE department for delivering the frontier polymers knowledge to us and developing professional skills; Dr. Alexander Ribbe, Louis Raboin and Sekar Thirunavukkarasu for their technical training and support in electron microscopy and X-ray scattering; Jo-Ann

Bourguignon and Lisa Gorth for taking care of ordering chemical, paperwork and documentation of each milestone in PSE Ph.D. program. It is their professional support and warm heart that makes me better focus on solving the puzzles in the polymeric world.

Finally, I am grateful to my PSE classmates of year 2012 and PSE friends for my adjustment to a new environment and culture. I remember the every moment with you when I was first year. Your sincere favors provide me a better understanding of American culture, holidays, driving rules and taking order in American restaurant. Special thanks to my uncle, aunt and Dr. Yinyong Li, your endless care embraces me and forwards me to finish the journey in PSE.

ABSTRACT

SYNTHESIS, CHARACTERIZATION AND APPLICATION OF BLOCK COPOLYMER AND NANOPARTICLE COMPOSITES

MAY 2017

YUE GAI, B.S., NANJING UNIVERISTY

M.S., UNIVERSITY OF MASSACHUSETTS, AMHERST

Ph.D., UNIVERSITY OF MASSACHUSETTS AMHERST

Directed by: Professor James J. Watkins

The "bottom-up" fabrication of functional hybrid material can be achieved by using directed self-assembly of functional nanoparticles (NP) and block copolymers (BCP) as templates. The versatile nanostructures of BCP provide possibilities to precisely control NPs spatial distribution and the resulting hybrid materials exhibit enhanced electrical, mechanical and optical functionalities. Three main topics related to BCP/NP composites are discussed in this dissertation: I) the spatial distribution of large NP in linear BCP; II) the morphology control of BCP templates with new architectures; and III) the magneto-optical properties of hybrid material using magnetic NPs.

For well-ordered BCP/NP composite, the ratio of NP core diameter (d_{core}) and BCP domain width (L) has been generally limited with $d_{core}/L < 0.3$ when BCP/NP interactions are relatively neutral or weak. By modifying the Au NPs with hydrogen bonding (H-bonding) donor group, the selective spatial distribution of Au NPs ranges in size up to 0.8 times that of the target domain width in symmetric polystyrene-*block*-poly (2-vinylpyridine) (PS-*b*-P2VP). In addition, H-bonding meditated 15 nm NPs can be directed by linear BCP of d_{core}/L up to 0.4 at 20wt % loading. The H-bonding interactions

between NP and BCP provide favorable enthalpic interaction to overcome the inherent entropy penalties mainly arising from polymer chain stretching upon the sequestration of large particles.

On the other hand, the extensive chain entanglements of linear BCP still remain a challenge for hybrid materials with the consequence of long processing duration, many defects and lack of orientation. Bottlebrush BCPs (BBCPs) exhibit much lower degree of chain entanglement due to the highly extended confirmation. A systematic study was conducted to investigate the morphology transitions that occur in polystyrene-*block*-poly (ethylene oxide) (PS-*b*-PEO) BBCPs upon varying PEO volume fraction (f_{PEO}) from 22 % to 81 %. Either symmetric or asymmetric lamellar morphologies were observed in the BBCPs over an exceptionally wide range of f_{PEO} from 28 % to 72 %. A microphase transition temperature T_{MST} was observed over a temperature range of 150-180 °C.

Finally, enhanced magneto-optical (MO) composites with excellent Faraday rotation (FR) response were fabricated using iron platinum (FePt) NPs and PS-*b*-P2VP linear BCP. Gallic acid (GA) functionalized FePt NPs with average d_{core} from 1.9 to 9.3 nm were selectively incorporated into a P2VP domain through H-bonding interactions. The use of copolymer template to selectively arrange the magnetic NPs enabled high MO performance with limited trade-off of scattering loss, providing a simple strategy to prepare functional materials for MO applications. Verdet constants of a 10 wt % loaded 4.9 nm FePt NP composite reached absolute magnitudes as high as ~ -6×10^4 °/T·m at 845 nm, as determined by FR measurements at room temperature, which is comparable to today's benchmark materials.

TABLE OF CONTENTS

Page

ACKNOWLEDGMENTS v

ABSTRACT vii

LIST OF TABLES xii

LIST OF FIGURES xiii

CHAPTER

1 INTRODUCTION 1

1.1 Self-Assembly of Block Copolymers 1
1.2 Functional Nanoparticles of Size-dependent Physical Properties 2

1.2.1 Gold Nanoparticles 2
1.2.2 Magnetic Nanoparticles 4
1.2.3 Dielectric Nanoparticles 5

1.3 Hybrid Material Containing Nanofillers Arrays Using Block Copolymers as Templates 6
1.4 Dissertation Overview 7
1.5 Reference 9

2 STRONG LIGAND-POLYMER INTERACTION FOR INCORPORATION OF LARGE NANOPARTICLES IN ORDERED COMPOSITE 16

2.1 Introduction 16

2.1.1 Block Copolymer Based Nanocomposite Application 16
2.1.2 Size Limitation of Large Nanoparticles in Ordered Composite 16
2.1.3 Strong Interaction Meditated Self-Assembly of Block Copolymer and Nanoparticles 18
2.1.4 Project Overview 19

2.2 Experimental 20

2.2.1 Materials 20
2.2.2 Preparation and Surface Modification of Gold Nanoparticles 21
2.2.3 Preparation of Symmetric Block Copolymer and Gold Nanoparticles Composite 22

2.2.4 Characterization 22

2.3 Results and Discussions 23

2.3.1 Size Distribution and Surface Stabilizer of Gold Nanoparticles 23
2.3.2 Gold Nanoparticles Distribution in Terms of Size Variation 26
2.3.3 Gold Nanoparticles Distribution in Terms of Loading 29
2.3.4 Summary 32

2.4 References 35

3 MORPHOLOGY EVOLUTIONS OF BOTTLEBRUSH BLOCK COPOLYMERS: INFLUENCE OF SIDE CHAIN AND VOLUME FRACTIONS 39

3.1 Introduction 39

3.1.1 Chain Entanglement of Linear Block Copolymer 39
3.1.2 Architecture and Application of Bottlebrush Block Copolymers 39
3.1.3 Current Morphology Study Progress of Bottlebrush Block Copolymers 40
3.1.4 Project Overview 41

3.2 Experimental 42

3.2.1 Materials 42
3.2.2 Preparation of Macromonomers and Third-Generation Grubbs Catalyst 43
3.2.3 Preparation of Bottlebrush Block Copolymers 44
3.2.4 Characterization 45

3.3 Results and Discussions 46

3.3.1 Synthesis Control of Bottlebrush Block Copolymers 46
3.3.2 Morphology Evolution As Function of Side Chain and Volume Fraction Asymmetry 49
3.3.3 Crystallization Effects of PEO Blocks 52
3.3.4 Microphase Transition Temperatures 54
3.3.5 Asymmetric Template for Incorporating Dual Functional Nanoparticles 56
3.3.6 Summary 58

3.4 References 60

4 MAGENTO-OPTICAL PROPERITES OF IRON PLATIUM NANOPARTICLES AND BLOCK COPOLYMER COMPOSITE 66

4.1 Introduction 66

4.1.1 Magnetic Nanoparticles 66
4.1.2 Faraday Rotations and Verdet Constant 66
4.1.3 Current Progress of Magneto-Optical Materials 68
4.1.4 Magnetic Nanoparticles and Polymer Composite: Advantages and Challenges 68
4.1.5 Project Overview 71

4.2 Experimental 72

4.2.1 Materials 72
4.2.2 Preparation of Iron Platinum Nanoparticles 73
4.2.3 Preparation of Commercial Available Magnetic Nanofillers Ink 73
4.2.4 Preparation of Nanocomposite Films 73
4.2.5 Preparation of Imprinted Nanoparticles Films 74
4.2.6 Characterization 74

4.3 Results and Discussions 77

4.3.1 Iron Platinum Nanoparticles Size Distributions 77
4.3.2 Morphology and Magnetism of Nanocomposite 79
4.3.3 Verdet Constant versus Nanoparticles Loading 81
4.3.4 Imprinted Films Morphology 85
4.3.5 Summary 87

4.4 References 88

5 SUMMARY AND OUTLOOK 96

5.1 Incorporation of Large Functional Nanoparticles into Ordered Composite 96
5.2 High Molecular Mobility of Brush Block Copolymers 98
5.3 Anisotropic Magnetic Nanocomposite 100
5.4 References 102

BIBLIOGRAPHY 103

LIST OF TABLES

Table Page

2.1. Molecular information for BCPs used for assemblies 21

2.2. Properties of Au NPs: samples from (a) to (d) stabilized with hydroquinone and (e) capped with PHOST 25

2.3. Au NPs volume fraction in hybrid composite 26

3.1. Characteristics of PS-NB and PEO-NB macromonomer (MM) 44

3.2. Characteristics of the PS-*b*-PEO BBCP 5k-Y, 2k-Y and 0.75k-Y series 46

4.1. FePt NPs core weight percentage and volume fraction ($f_{NP,}$,%) in the nanocomposites 78

4.2. Film thickness measurement of FePt/BCP composite 82

4.3. Verdet constants (V) of glass substrate 83

4.4. Verdet constants (V) of FePt NP/BCP composite films (10^4 °/T·m), calculation and measurements by Norwood group 84

4.5. Verdet constant of homopolymer/9.3 nm FePt-GA at 10 wt % 85

LIST OF FIGURES

Figure Page

1.1. (a) an illustration of di-BCP phase diagram where χN versus *f*, (b) the phase transition of a typical di-BCP, ranging from spherical, cylindrical, gyroid, lamellar to reverse corresponding structures as function of volume fractions, (c) experimental phase diagram of a series of PS-*b*-PI di-BCPs (adapted from reference 2, 6 in Chapter 1). 1

1.2. An overview of synthesized Au nanofillers of different sizes and shapes: (A) Au NPs of spherical geometry; (B) a series of Au NPs of increasing size synthesized via seed-growth mediated method; (C) anisotropic Au nanorods of various aspect ratio (adapated from reference 29, 30 in Chapter 1). 3

1.3. Summary of projects, (a): large NPs distribution in linear BCP, (b): bottlebrush BCP morphology Transitions and (c): magneto-optical properties of magnetic nanocomposite, with courtesy to Norwood group at Univeristy of Arizona. 8

2.1. NPs distribution in BCP of weak or neutral interactions: (a) simulation results (adapated from reference 27 in Chapter 2), (b) aliphatic NPs distribution (adapated from reference 25 in Chapter 2) in BCP as function of relative size ratio over domain width. 18

2.2. Illustration of strong interaction between the NPs and BCPs domains: (a) small molecules additives (adapted from reference 34 in Chapter 2) (b) direct H-bonding (adapted from reference 35 in Chapter 2) of Au NPs and PS-*b*-P2VP BCPs. 19

2.3. Illustration of first project: Au NPs of different core diameter were modified with H-bonding donor group and directed by symmetric PS-*b*-P2VP BCPs. The distributions of Au NPs were systematically investigated as function of size and loading. 19

2.4. TEM images and core diameter histograms of synthesized hydroxylated gold NPs; hydroquinone stabilized Au NPs (a) 1.81±0.30, (b) 5.70 ±0.86, (c) 8.87±1.50, (d) 15.3±1.70 nm and (e) PHOST capped Au NPs 16.0±2.60 nm accordingly. 24

2.5. FT-IR spectra of sets (A): (a) hydroquinone, hydroquinone coated Au NPs with average size (b) 1.81 (c) 5.70, (d) 8.87, (e) 15.3 nm. FT-IR spectra of sets (B): (f) PHOST coated Au NPs with d_{core} 16.0 nm, (g) poly (4-vinylphenol) (PHOST) and (h) poly (4-acetoxystyrene). 24

2.6. TEM images of NP-1.81 blends (a)-(d), NP-5.70 blends (e)-(h), NP-8.87 blends (i)-(l), and NP-15.3 blends (m)-(p) with linear symmetric PS-*b*-P2VP block copolymer of *Mn* (total) (a) 16.5, (b) 50, (c) 84, (d) 199 kg/mol. NPs volume fraction (including organic component) ~ 9 vol %-17 vol % (20 wt % from (a) to (l), 10 wt % from (m) to (p)). 27

2.7. TEM images of NP-16.0 blends with linear symmetric PS-*b*-P2VP of *Mn* (total) (a) 16.5, (b) 50, (c) 84, (d) 199 kg/mol. NPs volume fraction ~ 4 vol % (10 wt %). The P2VP domains are lightly stained with iodine to increase domain contrast. 28

2.8. SAXS spectra of (A) NP-1.81 blends (a)-(d), (B) NP-5.70 blends (e)-(h), (C) NP-8.87 blends (i)-(l), and (D) NP-15.3 blends (m)-(p) with linear symmetric PS-*b*-P2VP of *Mn* (total) (a) 16.5, (b) 50, (c) 84, (d) 199 kg/mol. NPs volume fraction (including organic component) 9 vol %-17 vol % (20 wt % from (a) to (l), 10 wt % from (m) to (p)). 29

2.9. TEM images of NP-1.81 blends with PS(25k)-b-P2VP(25k) (d_{core}/L~0.12) with NPs volume fraction (including organic component) from 8 vol % to 45 vol %: (a) 10 wt %, (b) 20 wt %, (c) 30 wt % (d) 40 wt % (e) 50 wt %; TEM images of NP-5.70 blends with PS(25k)-b-P2VP(25k) (d_{core}/L~0.38) with volume fraction (including organic component) from 7 vol % to 42 vol % : (f) 10 wt %, (g) 20 wt %, (h) 30 wt % (i) 40 wt % (j) 50 wt %; TEM images of NP-16.0 blends with PS(40k)-b-P2VP(44k) (d_{core}/L~0.61) with NPs volume fraction (including organic component) from 4 vol % to 18 vol %: (k) 10 wt %, (l) 20 wt %, (m) 30 wt % (n) 40 wt %; samples from (k) to (n) are stained with Iodine to increase domain contrast. Ordered structured remained with NPs volume fraction up to ~ 25 vol % (with organic ligands). 30

2.10. (A): SAXS spectra of blends of PS (25k)-*b*-P2VP (25k) with NP-1.81 at different volume fraction (including organic component) from 8 vol % to 45 vol %: (a) 10 wt %, (b) 20 wt %, (c) 30 wt % (d) 40 wt % (e) 50 wt % with d_{core}/L~0.12; (B): SAXS profiles of blends based on the same BCP containing NP-5.70 (d_{core}/L~0.38) with NPs volume fraction (including organic component) from 7 vol % to 42 vol % : (f) 10 wt %, (g) 20 wt %, (h) 30 wt % (i) 40 wt % (j) 50 wt %. 31

2.11. (a) Relationship between d_{core}/L and NPs location as indicated by labels: U = uniform distribution, ED=edge diffused, C=centered distribution, B=interface/boundary of domain, D=disorder/ NPs expelled from domain. The analysis TEM images are from Figure 2.6 and Figure 2.7. NP-REF-(i) (reference 25) and NP-REF-(ii) (reference 30 in Chapter 2) are representative NPs distribution of neutral/weak NP/BCP interactions. 32

3.1. Illustration of PS-*b*-PEO BBCP with designated side chain lengths: PEO-NB (M_n ~ 0.75, 2.0 and 5.0 kg/mol accordingly) and PS-NB (M_n ~ 3.5 kg/mol). The PEO volume fraction (f_{PEO}) was controlled approximately from 20 % to 80 %. 42

3.2. Representative (a)^{1}H-NMR, (b)^{13}C-NMR spectrum of synthesized PS-*b*-PEO BBCPs and (c) ^{1}H-NMR spectra of PS homo brush polymer after 20 minutes reaction and PS MM. 47

3.3. FT-IR spectrums of representative 5k-Y series. 48

3.4. GPC traces of PS-*b*-EPO BBCPs (a) 5k-Y, (b) 2k-Y and (c) 0.75k-Y series. ... 49

3.5. SAXS spectra (at room temperature) of PS-*b*-PEO BBCPs with PEO side lengths (a) PEO M_n ~ 2.0 kg/mol, f_{PEO} from 22 % to 79 %; (b) and (c) PEO M_n ~ 5.0 kg/mol, f_{PEO} from 24 % to 81 %. The broad curve with an arrow is attributed to X-ray scattering from PEO crystalline lamellae. 50

3.6. TEM images of cryo-microtomed PS-*b*-PEO BBCPs: (a) a disordered morphology in 2k-22; (b, c, d, e) asymmetric lamellae in (b) 2k-71, (c) 5k-28, (d) 5k-32 and (e) 5k-72; highly asymmetric BBCPs (f) 5k- 81 and (g) 2k-79. Ruthenium tetroxide (RuO_4) was used as the staining agent to improve the contrast between PS (bright area) and PEO (dark area) domains, all scale bars correspond to 100 nm. The arrow in (g) points to a region where PEO crystalline lamellae can be identified in the PEO-rich BBCP. 51

3.7. Temperature controlled SAXS and WAXS 1-D profiles of BBCPs containing high volume fractions of PEO: (a) 2k-79, (b) 5k-81, (c) 2k-71, and (d) 5k-72. Higher order reflections peaks can be observed at temperature that result in a melt state of the PEO domain. 53

3.8. DSC measurement of representative PS-*b*-PEO BBCPs. 54

3.9. 1-D SAXS profiles of BBCPs: (a) 5k-28, (c) 2k-79 and (e) 2k-22 show the influence of temperature on FWHM of the primary peak. (b, d, f) FWHM as a function of temperature of BBCPs: (b) 5k-28, (d) 2k-79 and (f) 2k-22 obtained by Gaussian Fitting of the primary peak. 55

3.10. Ternary composite using PS-*b*-PEO BBCP as template, with 5 wt % 6 nm ZrO_2-GA and 5 wt % 15 nm Au-PS NPs:(a) TEM images of asymmetric lamellae, ZrO_2-GA resided in the narrower PEO domain while Au NPs had selective distribution in PS domain (b) schematic of asymmetric BBCP and ternary composite, (c) SAXS spectra of ternary composite. 58

3.11. Summary of PS-*b*-PEO BBCP phase transition: a plot of side chain length ratio (M_n (PEO-NB)/M_n (PS-NB)) *vs.* PEO volume fraction (f_{PEO}). 59

4.1. The illustration of Faraday rotation: the polarization plane of light will be altered to certain angle when exposed to an applied field (adapted from online reference 18 in Chapter 4). 67

4.2. Well-ordered lamellae morphology using modified FePt NPs and PS (13.7k)-*b*-P2VP (5.2k) BCPs via H-bonding interaction. 40 wt % loading of FePt NPs introduced order-to-order transition (Courtesy to Dr. Xinyu Wang, adapted from reference 80 in Chapter 4). 70

4.3. Project overview: (a) Surface modification of FePt NPs using gallic acid (GA) as a hydrogen bonding donor followed by selective NP dispersion in the P2VP domain within a symmetric PS-*b*-P2VP BCP template (b) setup of FR response measurement, courtesy to Norwood group. 71

4.4. Nanoimprinting of MNPs using polar suspension and polydimethylsiloxane (PDMS) stamp. The feature sizes of pattern were transferred from a master substrate (courtesy to Yiliang Zhou for procedure sketch). 72

4.5. TEM images of FePt NPs and size distribution histogram: (a) 1.9 nm, (b) 4.9 nm, (c) 5.7 nm and (d) 9.3 nm of average core diameter. Spherical estimation was used for (a)-(c) and square geometry was applied to (d) in Image J analysis. 77

4.6. Crystal structure of size controlled FePt particles: (a) XRD spectrum of $d_{core\sim}$ 5.7 nm and 9.3 nm FePt NPs powder, fcc characteristic peaks agree with previous results; (b) $d_{core\sim}$ 9.3 nm and (c) $d_{core\sim}$ 5.7 nm are electron diffraction images, the halo pattern corresponds to the XRD spectrum calibrated with a gold standard sample. 78

4.7. Room temperature SAXS profiles of neat PS (102 kg/mol)-*b*-P2VP (97 kg/mol) with (i) 1.9 nm, (ii) 4.9 nm, (iii) 5.7 nm and (iv) 9.3 nm FePt NPs at 2.5 wt % loading. TEM images of 10 wt % loading of (b) 1.9 nm NPs and (c) 9.3 nm NPs in BCP. The P2VP domain was lightly stained with iodine: particles show selective distribution through favorable H-bonding interactions (provided by Dr. Xinyu Wang). 80

4.8. Hysteresis loops of 2.5 wt %1.9 nm, 5.5 nm and 9.3nm FePt NPs in PS (102 kg/mol)-*b*-P2VP (97 kg/mol) composite. The magnetization falls back to zero in absence of the applied magnetic field for all sizes of particles (measured by Dr. Palash Gangopadhyay). 81

4.9. TEM images of (a) asymmetric X=3-4 nm, Y=5-7 nm FePt-GA NPs in DMF solution and (b) surface modified commercial MNPs (15-20 nm according to supplier) in 1,2-propendiol and ethanol, stabilized with HBA. 85

4.10. Morphology of imprinted films on Si wafer: (a) and (c) AFM and height profiles imprinted MNPs films using 500 nm PDMS stamp; (b) and (d) SEM images of FePt and Fe_3O_4 films respectively. All scale bars are 2 μm. 86

4.11. A preliminary FR response characterization of pillar structured FePt-GA NPs on glass substrate. The polarization plane of light can still be tilted after removal of the magnetic fields. 87

5.1. Illustration of a rapid and scalable process for the synthesis of hierarchical porous hybrid films of silica, carbon and gold on flexible substrate via photothermal treatment (adapted from reference 1 in Chapter 5). 97

5.2. Dynamic Master Curves of G' (open symbols) and G" (closed symbols) for PS-*b*-PEO BBCP samples at a reference temperature of T_{ref} = 120 °C. Labels indicate the following features (1) Glassy region, (2) Intermediate (backbone) relaxation, (3) Confined terminal flow. Curves shifted vertically by indicated scaling factors to provide clarity. b) Time temperature superposition shift factors a_T (closed symbols) and b_T (open symbols) for master curve. Line shows fit to WLF equation (adapted from reference 6 in Chapter 5). 99

5.3. TEM images of cobalt NRs in ethanol suspension: (a) average core diameter 19 nm, length 100 nm and (b) average core diameter 14.5 nm, length 20-40 nm (courtesy to Lacroix group at Institut National des Sciences Appliquées de Toulouse, France). 101

CHAPTER 1

INTRODUCTION

1.1 Self-Assembly of Block Copolymers

Block copolymers (BCP) are macromolecules consisting of two or more segments connected with a covalent bond. Di-BCPs are macromolecules covalently bonded of two blocks and can self-assemble into periodical structures at the nanoscale.[1–5] Three parameters contribute to the morphology transition of BCP: the Flory-Huggins parameter (χ), total degree of polymerization (N), and block volume fractions (f).[1,4] By simply tuning the block chemical nature, compositions, and molar mass, the BCPs can exhibit periodically ordered lamellar, cylindrical, and spherical structures as shown in Figure 1.1 (a) and (b). In most cases, the phase diagram may be deviated from the Figure 1.1 (a) due to the two monomers size difference and complex interaction description between two blocks (instead of χN). Asymmetric morphology transition have been observed, such as the phase diagram of poly (styrene)-*block*-poly (isoprene) (PS-*b*-PI) in Figure 1.1(c).[6]

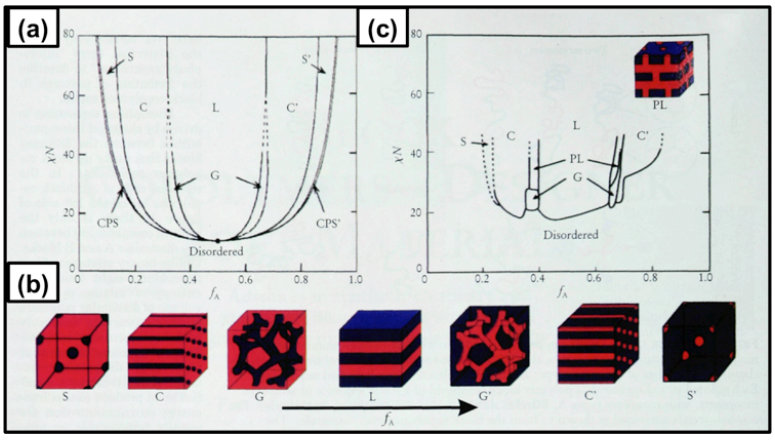

Figure 1.1(a) an illustration of di-BCP phase diagram where χN versus f, (b) the phase transition of a typical di-BCP, ranging from spherical, cylindrical, gyroid, lamellar to reverse corresponding structures as function of volume fractions, (c) experimental phase diagram of a series of PS-*b*-PI di-BCPs (adapted from reference 2, 6 in Chapter 1).

As a scaffold, BCPs have been utilized in many nanotechnology applications, including directing functional nanofillers, nanolithography, solar cells percolation layer matrix, and micelle template for drug or biomolecules delivery.[7–16] BCPs of more varied architectures, star-, brush- or ring-like structures can yield more interesting structures and enrich the potential applications.[2]

1.2 Functional Nanoparticles of Size-dependent Physical Properties

Miniaturization of bulk materials results in the development of nanoparticles nowadays of high surface per volume ratio. Materials including noble metals, metal oxides, and semiconducting elements have been studied for decades. Particularly, particles of the feature size of sub-100 nm are known as nanoparticles (NPs), which increases surface per volume ratio significantly. NPs retains the attractive physical properties of bulk state material and high ratio of surface over volume, enabling it to work as high efficient catalysts, biomedicine vehicles, bio-sensors, and additives to improve raw material mechanical, optical, or electrical performance.[17–23]

1.2.1 Gold Nanoparticles

In the long history, gold (Au) has always been valued by society. The miniaturized Au NPs, similar to their bulk state in human society, have always garnered people's attention. This type of metal NPs has been widely applied in biology for imaging, sensing and drug delivery for excellent biocompatibility, and in optical or electrical devices due to their plasmonic effects.[17,18,24–28] For example, Parak and coworkers[28] reported that the optical microscopy can image Au NPs of larger than 20 nm. Because the wavelength of absorbed light highly generally depends on the size and shape

of Au NPs, they can be utilized as labels with different color in the visible spectrum. In another review[25], plasmonic glucose or cysteine sensors have been fabricated based on the principles that a plasmon absorption spectrum changes upon the NPs aggregation, strong interaction, or surface stabilizer variation.

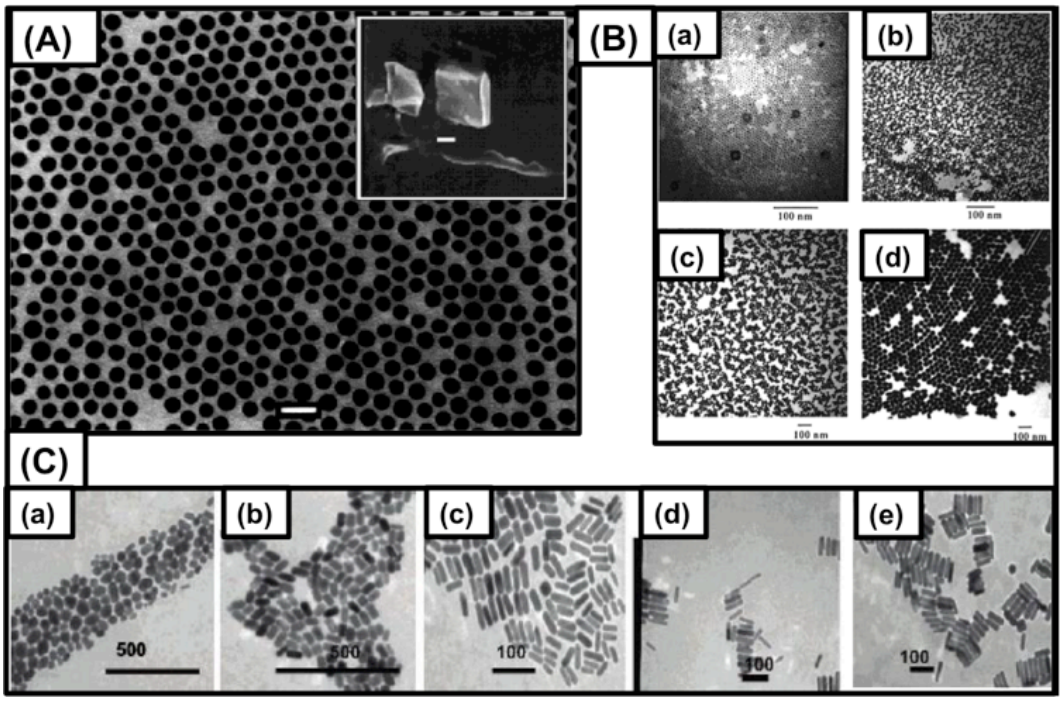

Figure 1.2 An overview of synthesized Au nanofillers of different sizes and shapes: (A) Au NPs of spherical geometry; (B) a series of Au NPs of increasing size synthesized via seed-growth mediated method; (C) anisotropic Au nanorods of various aspect ratio (adapted from reference 29, 30 in Chapter 1).

Over the last several decades, researchers have developed various techniques to control Au NPs size, surface functionalization, geometry and aspect ratio (Figure 1.2).[29–32] These valuable efforts have enabled the preparation of hybrid materials using Au NPs with control over the moieties. Precise control over building block direction, medium, size, and shape of Au species in final composite provides more possibilities for the next-generation hybrid materials.

1.2.2 Magnetic Nanoparticles

Humans have known ferromagnetic bulk material containing cobalt (Co) or iron (Fe) elements for centuries, and discovered the new continent based on the invention of a compass. For such kind of materials, the magnetization follows the direction of an external magnetic field and remains after the removal of the field. Today, the progresses in the miniaturized magnetic NPs synthesis provide the control over size and shape by using a series of method: co-precipitation, thermal decomposition or reduction, micelle or hydrothermal synthesis.[33–35] For example, the shape and size (3- 50 nm) of iron oxide (Fe_3O_4) NPs can be well controlled using decomposition of an iron precursor with oleylamine, oleic acid in phenol ether.[34] Similar to other NPs, the poorly stabilized magnetic NPs easily form aggregates due to surface energy. Subsequent oxidation may further degrade the magnetic properties in solution. In order to maintain their unique properties, grafting surface of polymer and inorganic layers have been utilized.[33]

The magnetism of the NPs is highly size-dependent. The smaller NPs of core diameter less than 20 nm, usually known as paramagnetic or superparamagnetic, exhibit minima amount of remaining magnetization after removal of external field, offering the possibility for different nanotechnology applications.[19] For instance, because the magnetic NPs have comparable sizes relative to cells, viruses and proteins, from the biomedicine view, these tiny objects have been controlled well to demonstrate separation of labeled cells apart from other biological species, targeted delivery of drug and gene, therapy curing of tumors and contrast enhancement in magnetic resonance imaging for disease diagnose.[36,37] In addition, efforts have also been dedicated to the magnetic fluids, catalysis, environmental remediation and data storages applications to take advantages of

magnetic NPs.[19,20,38] By embedding the 11 nm Co NPs within the ordered mesoporous carbon, the resulting material was suitable for the separable sorbent or catalyst support.[20]

1.2.3 Dielectric Nanoparticles

Dielectric materials exhibit polarization when exposed to an external electric field. High dielectric permittivity materials have been used as medium in electronic device such as capacitors. Recent development of electronic device requires the dielectric material having high dielectric constant, low dielectric loss especially at a high frequency, and low temperature dependency.[39]

Previous bulky dielectric materials are usually limited with their mechanical properties because most known metal oxides lack the physical flexibility. Efforts have been dedicated to preparing nanocomposites using polymer as matrix to direct the dielectric nanofillers.[40–42] The performance of the final composites requires delicate control over dielectric species surface modification and degree of homogeneity of final blends. Structured composites have shown enhanced dielectric constants for various applications.[23,43–45] For example, Jiang et al.[45] reported the synthesis of core-shell structured barium titanate ($BaTiO_3$) NPs using radical polymerization methods. The dielectric loss of resulting high loaded homogenous composites were effectively suppressed, which was well suited for energy storages applications. Gupta and coworkers[43] reported the silica (SiO_2) NPs enhanced the conjugated polymers performance in organic solar cells. The dielectric NPs have been also utilized in nonlinear and ultrafast nano-photonics, enhanced infrared absorption, and imaging in electrostatic force microscopy.[21,22,44,46,47]

1.3 Hybrid Material Containing Nanofillers Arrays Using Block Copolymers as Templates

Composites containing functional nanofillers using polymers as templates have been quite popular in recent years. For instances, the mechanical reinforcement of composites was achieved by blending carbon nanotubes into polymer matrix.[48] Polystyrene-*block*-poly (methyl methacrylate) (PS-*b*-PMMA) and Au NPs blends showed their excellent performance in the organic electronic area.[49] The integral performance of hybrid material requires delicate control over nanofillers size, shape, geometry loading, spatial distribution as well as the building blocks directions.[50–52]

Self-assembly of NPs and BCPs has been demonstrated as an elegant and powerful "bottom-up" method to fabricate naocomposites, enabling the large-scale nanostructured system available for electronic, magnetic or photonic performance enhancement.[49,53–55] Unlike in-situ reaction, "bottom-up" strategy is more attractive because it allows better control over additives, surface stabilizer, and loading in the final composite.[56–58]

Numerous efforts have been dedicated to optimize surface ligand of NPs, and it has been proved that selective surface medication assists the NPs to distribute in a target domain of BCP.[59–67] Kramer group[60,61,66] has reported that the NPs capped with PS have favorable locations in PS domain of Polystyrene-*block*-poly (2-vinyl pyridine) (PS-*b*-P2VP) BCP; on the other hand, the PS and P2VP homopolymer blend tethered NPs prefer to localize at the interface of the two blocks. The NPs distribution within BCP matrix is balanced by the enthalpy contributed from BCP/NP interaction and the entropy penalty resulting from polymer chain stretching and NPs translation.[50–52]

The typical system in which "A" polymer protected NPs reside in an "A-B" BCP, the enthalpy contribution is usually limited due to the neutral or weak interaction between NP and BCP. In order to increase loading while maintaining the ordering of a final composite, strong hydrogen bonding (H-bonding) interactions of BCP/NP has been introduced.[68–76] Xu's group[68,70] used a small molecule to connect alkyl chain stabilized NPs, and lock these additives in polystyrene-*block*-poly (4-vinyl prydine) (PS-*b*-P4VP) BCP. Hawker and coworkers[62] reported that Au NPs distribution in P2VP domain with multiple H-bonding donor oligomer ligand in PS-*b*-P2VP matrix. Our group[71,74] has demonstrated using small molecule ligand to introduce direct H-bonding interaction between NPs and target domain, and achieved 30 wt % loading of additives while maintaining the well-ordered lamellar structures. The favorable enthalpy offsets the entropy penalty and enhances the composite phase segregation. This method provides a new platform for hybrid material preparation for functional applications.

1.4 Dissertation Overview

In this thesis, three main projects were performed and are fully discussed (illustration in Figure 1.3).

In the first part, Au NPs distribution in linear BCP template as a function of size and loading concentration was systematically investigated. As mentioned above in the chapter 1.3, the entropy penalty from polymer chain rearrangement increases after sequestration of large obstacles, limiting either the relative or absolute size of incorporated NPs.[77,78] H-bonding donor ligands were used to modify the Au NPs and as a result, the relatively large NPs can be incorporated into the linear BCP.

In the second part, the morphology evolution of a new architecture BCP was studied. The severe chain entanglements of linear BCP may induce longer processing time and potentially more defects. The highly extended conformation of brush polymers provides many attractive properties for nanotechnology applications: large domain size, rapid kinetic ordering, and the ability to take high loading of functional additives.[79,80] This project focuses on two molecular characteristics: side chain and block volume fraction, which affect the interface curvature of two blocks and subsequently introduce the morphology transitions of polymers.

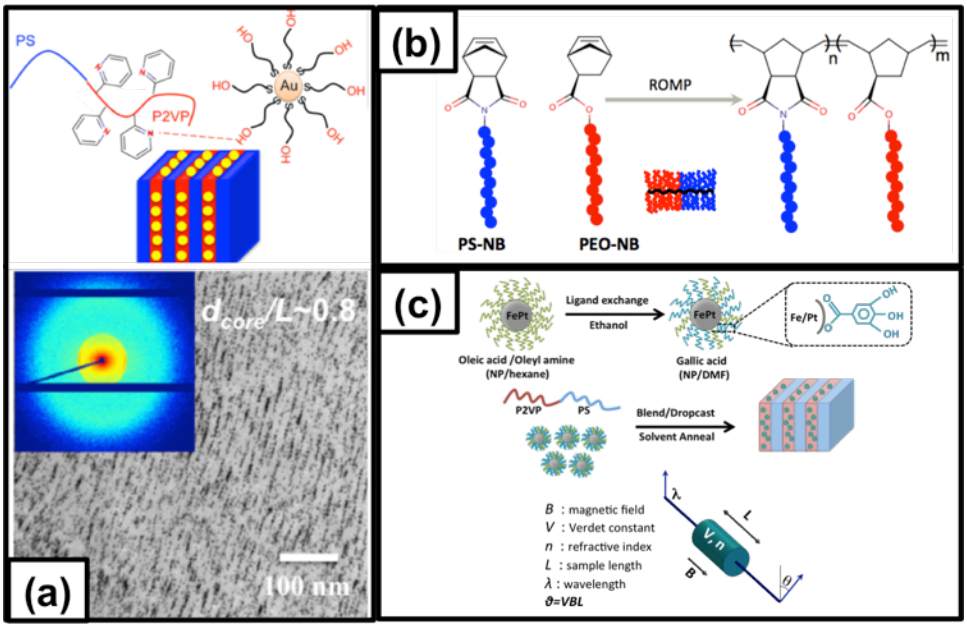

Figure 1.3 Summary of projects, (a): large NPs distribution in linear BCP, (b): bottlebrush BCP morphology Transitions and (c): magneto-optical properties of magnetic nanocomposite, with courtesy to Norwood group at Univeristy of Arizona.

In the third part, more attention was paid to the application of BCP and magnetic NPs. Thanks to the collaboration with Norwood group in the University of Arizona, the magneto-optical properties of this hybrid materials were able to be investigated. The Faraday rotation performance of composites was comparable to today's benchmark material. The low cost, simple and straightforward "bottom-up" method using BCP as

template to direct magnetic NPs is compatible with various coating techniques for flexible deposition, ideal for large-area device fabrication.

1.5 Reference

(1) Bates, F. S.; Fredrickson, G. H. Block Copolymer Thermodynamics: Theory and Experiment. *Annu. Rev. Phys. Chem.* **1990**, *41*, 525–557.

(2) Bates, F. S.; Fredrickson, G. H. Block Copolymers—Designer Soft Materials. *Phys. Today* **1999**, *52*, 32–38.

(3) Fredrickson, G. H.; Bates, F. S. Dynamics of Block Copolymers: Theory and Experiment. *Annu. Rev. Mater. Sci.* **1996**, *26*, 501–550.

(4) Leibler, L. Theory of Microphase Separation in Block Copolymers. *Macromolecules* **1980**, *13*, 1602–1617.

(5) Ruzette, A.-V.; Leibler, L. Block Copolymers in Tomorrow's Plastics. *Nat. Mater.* **2005**, *4*, 19–31.

(6) Khandpur, A. K.; Forster, S.; Bates, F. S.; Hamley, I. W.; Ryan, A. J.; Bras, W.; Almdal, K.; Mortensen, K. Polyisoprene-Polystyrene Diblock Copolymer Phase Diagram near the Order-Disorder Transition. *Macromolecules* **1995**, *28*, 8796–8806.

(7) Bang, J.; Jeong, U.; Ryu, D. Y.; Russell, T. P.; Hawker, C. J. Block Copolymer Nanolithography: Translation of Molecular Level Control to Nanoscale Patterns. *Adv. Mater.* **2009**, *21*, 4769–4792.

(8) Cheng, J. Y.; Ross, C. A.; Smith, H. I.; Thomas, E. L. Templated Self-Assembly of Block Copolymers: Top-down Helps Bottom-Up. *Adv. Mater.* **2006**, *18*, 2505–2521.

(9) Cui, H.; Chen, Z.; Zhong, S.; Wooley, K. L.; Pochan, D. J. Block Copolymer Assembly via Kinetic Control. *Science.* **2007**, *317*, 647–650.

(10) Discher, D. E.; Eisenberg, A. Polymer Vesicles. *Science.* **2002**, *297*, 967–973.

(11) Ha, J. M.; Wolf, J. H.; Hillmyer, M. A.; Ward, M. D. Polymorph Selectivity under Nanoscopic Confinement. *J. Am. Chem. Soc.* **2004**, *126*, 3382–3383.

(12) Jackson, E. A.; Hillmyer, M. A. Nanoporous Membranes Derived from Block Copolymers: From Drug Delivery to Water Filtration. *ACS Nano* **2010**, *4*, 3548–3553.

(13) Kim, D. H.; Sun, Z.; Russell, T. P.; Knoll, W.; Gutmann, J. S. Organic-Inorganic Nanohybridization by Block Copolymer Thin Films. *Adv. Funct. Mater.* **2005**, *15*, 1160–1164.

(14) Klok, H. A.; Lecommandoux, S. Supramolecular Materials via Block Copolymer Self-Assembly. *Adv. Mater.* **2001**, *13*, 1217–1229.

(15) Tang, C.; Lennon, E. M.; Fredrickson, G. H.; Kramer, E. J.; Hawker, C. J. Evolution of Block Copolymer Lithography to Highly Ordered Square Arrays. *Science.* **2008**, *322*, 429–432.

(16) Thurn-Albrecht, T.; Schotter, J.; Kästle, G. a; Emley, N.; Shibauchi, T.; Krusin-Elbaum, L.; Guarini, K.; Black, C. T.; Tuominen, M. T.; Russell, T. P. Ultrahigh-Density Nanowire Arrays Grown in Self-Assembled Diblock Copolymer Templates. *Science.* **2000**, *290*, 2126–2129.

(17) Hu, M.; Chen, J.; Li, Z.-Y.; Au, L.; Hartland, G. V; Li, X.; Marquez, M.; Xia, Y. Gold Nanostructures: Engineering Their Plasmonic Properties for Biomedical Applications. *Chem. Soc. Rev.* **2006**, *35*, 1084–1094.

(18) Jain, P. K.; Huang, X.; El-Sayed, I. H.; El-Sayed, M. A. Review of Some Interesting Surface Plasmon Resonance-Enhanced Properties of Noble Metal Nanoparticles and Their Applications to Biosystems. *Plasmonics* **2007**, *2*, 107–118.

(19) Frey, N. A.; Peng, S.; Cheng, K.; Sun, S. Magnetic Nanoparticles: Synthesis, Functionalization, and Applications in Bioimaging and Magnetic Energy Storage. *Chem. Soc. Rev.* **2009**, *38*, 2532–2542.

(20) Lu, A. H.; Schmidt, W.; Matoussevitch, N.; Bönnemann, H.; Spliethoff, B.; Tesche, B.; Bill, E.; Kiefer, W.; Schüth, F. Nanoengineering of a Magnetically Separable Hydrogenation Catalyst. *Angew. Chemie Int. Ed.* **2004**, *43*, 4303–4306.

(21) Anderson, M. S. Enhanced Infrared Absorption with Dielectric Nanoparticles. *Appl. Phys. Lett.* **2003**, *83*, 2964–2966.

(22) Akimov, Y. A.; Koh, W. S.; Sian, S. Y.; Ren, S. Nanoparticle-Enhanced Thin Film Solar Cells: Metallic or Dielectric Nanoparticles? *Appl. Phys. Lett.* **2010**, *96*, 73111.

(23) Huang, X.; Jiang, P. Core-Shell Structured High- K Polymer Nanocomposites for Energy Storage and Dielectric Applications. *Adv. Mater.* **2015**, *27*, 546–554.

(24) Elghanian, R. Selective Colorimetric Detection of Polynucleotides Based on the Distance-Dependent Optical Properties of Gold Nanoparticles. *Science.* **2007**, *277*, 1078–1081.

(25) Ghosh, S. K.; Pal, T. Interparticle Coupling Effect on the Surface Plasmon Resonance of Gold Nanoparticles: From Theory to Applications. *Chem. Rev.* **2007**, *107*, 4797–4862.

(26) Jain, P. K.; Lee, K. S.; El-Sayed, I. H.; El-Sayed, M. A. Calculated Absorption and Scattering Properties of Gold Nanoparticles of Different Size, Shape, and Composition: Applications in Biological Imaging and Biomedicine. *J. Phys. Chem. B* **2006**, *110*, 7238–7248.

(27) Saha, S.; Pal, A.; Kundu, S.; Basu, S.; Pal, T. Photochemical Green Synthesis of Calcium-Alginate-Stabilized Ag and Au Nanoparticles and Their Catalytic Application to 4-Nitrophenol Reduction. *Langmuir* **2010**, *26*, 2885–2893.

(28) Sperling, R. A.; Gil, P. R.; Zhang, F.; Zanella, M.; Parak, W. J. Biological Applications of Gold Nanoparticles. *Chem. Soc. Rev.* **2008**, *37*, 1896–1908.

(29) Daniel, M. C. M.; Astruc, D. Gold Nanoparticles: Assembly, Supramolecular Chemistry, Quantum-Size Related Properties and Applications toward Biology, Catalysis and Nanotechnology. *Chem. Rev.* **2004**, *104*, 293–346.

(30) Murphy, C. J.; Sau, T. K.; Gole, A. M.; Orendoff, C. J.; Gao, J.; Gou, L.; Hunyadi, S. E.; Li, T. Anisotropic Metal Nanoparticles: Synthesis, Assembly and Optical Applications. *J. Phys. Chem B.* **2005**, *109*, 13857–13870.

(31) Brust, M.; Walker, M.; Bethell, D.; Schiffrin, D. J.; Whyman, R. Synthesis of Thiol-Derivatised Gold Nanoparticles in a Two-Phase Liquid-Liquid System. *J.Chem. Soc.,Chem. Commun.* **1994**, 801–802.

(32) Sun, Y.; Xia, Y. Shape-Controlled Synthesis of Gold and Silver Nanoparticles. *Science.* **2002**, *298*, 2176–2179.

(33) Lu, A. H.; Salabas, E. L.; Schüth, F. Magnetic Nanoparticles: Synthesis, Protection, Functionalization, and Application. *Angew. Chemie Int. Ed.* **2007**, *46*, 1222–1244.

(34) Jana, N. R.; Chen, Y.; Peng, X. Size- and Shape-Controlled Magnetic (Cr , Mn , Fe , Co , Ni) Oxide Nanocrystals via a Simple and General Approach. *Chem. Mater.* **2004**, *16*, 3931–3935.

(35) Dumestre, F.; Chaudret, B.; Amiens, C.; Respaud, M.; Fejes, P.; Renaud, P.; Zurcher, P. Unprecedented Crystalline Super-Lattices of Monodisperse Cobalt Nanorods. *Angew. Chemie Int. Ed.* **2003**, *42*, 5213–5216.

(36) Pankhurst, Q. a.; Thanh, N. T. K.; Jones, S. K.; Dobson, J. Progress in Applications of Magnetic Nanoparticles in Biomedicine. *J. Phys. D. Appl. Phys.* **2009**, *42*, 224001.

(37) Q. A. Pankhurst; Connolly, J.; S. K. Jones; Dobson, J. Applications of Magnetic Nanoparticles in Biomedicine. *J. Phys. D Appl. Phys.* **2003**, *36*, R167–R181.

(38) Reddy, L. H.; Arias, J. L.; Nicolas, J.; Couvreur, P. Magnetic Nanoparticles: Design and Characerization,Toxicity and Biocompatibility,Pharmaceutical and Biomedical Applications. *Chem. Rev.* **2012**, *112*, 5818–5878.

(39) Cava, R. J. Dielectric Materials for Applications in Microwave Communications. *J. Mater. Chem.* **2001**, *11*, 54–62.

(40) Oskam, G. Metal Oxide Nanoparticles: Synthesis, Characterization and Application. *J. Sol-Gel Sci. Technol.* **2006**, *37*, 161–164.

(41) Paraffin, T.; Shell, C.; Balasubramanian, B.; Kraemer, K. L.; Reding, N. A.; Skomski, R.; Ducharme, S.; Sellmyer, D. J. Synthesis of Monodisperse Properties. *ACS Nano* **2010**, *4*, 1893–1900.

(42) Procedures, E.; Milli-q, M. Communications to the Editor. *Water* **1990**, 2415–2416.

(43) Gollu, S. R.; Sharma, R.; Srinivas, G.; Kundu, S.; Gupta, D. Incorporation of SiO2 Dielectric Nanoparticles for Performance Enhancement in P3HT:PCBM Inverted Organic Solar Cells. *Org. Electron.* **2015**, *24*, 43–50.

(44) Sahagún, E.; Sáenz, J. J. Dielectric Nanoparticles: Polarizability Reveals Identity. *Nat. Mater.* **2012**, *11*, 748–749.

(45) Yang, K.; Huang, X.; Huang, Y.; Xie, L.; Jiang, P. Fluoro-Polymer@BaTiO3 Hybrid Nanoparticles Prepared via RAFT Polymerization: Toward Ferroelectric Polymer Nanocomposites with High Dielectric Constant and Low Dielectric Loss for Energy Storage Application. *Chem. Mater.* **2013**, *25*, 2327–2338.

(46) Savelev, R. S.; Yulin, A. V.; Krasnok, A. E.; Kivshar, Y. S. Solitary Waves in Chains of High-Index Dielectric Nanoparticles. *ACS Photonics* **2016**, *3*, 1869–1876.

(47) Sinev, I.; Iorsh, I.; Bogdanov, A.; Permyakov, D.; Komissarenko, F.; Mukhin, I.; Samusev, A.; Valuckas, V.; Kuznetsov, A. I.; Luk'yanchuk, B. S.; *et al.* Polarization Control over Electric and Magnetic Dipole Resonances of Dielectric Nanoparticles on Metallic Films. *Laser Photon. Rev.* **2016**, *8*, 1–8.

(48) Spitalsky, Z.; Tasis, D.; Papagelis, K.; Galiotis, C. Carbon Nanotube-Polymer Composites: Chemistry, Processing, Mechanical and Electrical Properties. *Prog. Polym. Sci.* **2010**, *35*, 357–401.

(49) Rosa, C. De; Auriemma, F.; Girolamo, R. Di; Pepe, G. P.; Napolitano, T.; Scaldaferri, R. Enabling Strategies in Organic Electronics Using Ordered Block Copolymer Nanostructures. *Adv. Mater.* **2010**, *22*, 5414–5419.

(50) Balazs, A. C.; Emrick, T.; Russell, T. P. Nanoparticle Polymer Composites: Where Two Small Worlds Meet. *Science.* **2006**, *314*, 1107–1110.

(51) Bockstaller, M. R.; Mickiewicz, R. a.; Thomas, E. L. Block Copolymer Nanocomposites: Perspectives for Tailored Functional Materials. *Adv. Mater.* **2005**, *17*, 1331–1349.

(52) Kao, J.; Thorkelsson, K.; Bai, P.; Rancatore, B. J.; Xu, T. Toward Functional Nanocomposites: Taking the Best of Nanoparticles, Polymers, and Small Molecules. *Chem. Soc. Rev.* **2013**, *42*, 2654–2678.

(53) Jaramillo, T. F.; Baeck, S. H.; Cuenya, B. R.; McFarland, E. W. Catalytic Activity of Supported Au Nanoparticles Deposited from Block Copolymer Micelles. *J. Am. Chem. Soc.* **2003**, *125*, 7148–7149.

(54) Huynh, W. U.; Dittmer, J. J.; Alivisatos, A. P. Hybrid Nanorod-Polymer Solar Cells. *Science.* **2002**, *295*, 2425–2427.

(55) Tang, Z.; Kotov, N. A. One-Dimensional Assemblies of Nanoparticles: Preparation, Properties, and Promise. *Adv. Mater.* **2005**, *17*, 951–962.

(56) Joly, S.; Kane, R.; Radzilowski, L.; Wang, T.; Wu, A.; Cohen, R. E.; Thomas, E. L.; Rubner, M. F. Multilayer Nanoreactors for Metallic and Semiconducting Particles. *Langmuir* **2000**, *16*, 1354–1359.

(57) Leong, W. L.; Lee, P. S.; Lohani, A.; Lam, Y. M.; Chen, T.; Zhang, S.; Dodabalapur, A.; Mhaisalkar, S. G. Non-Volatile Organic Memory Applications Enabled by in Situ Synthesis of Gold Nanoparticles in a Self-Assembled Block Copolymer. *Adv. Mater.* **2008**, *20*, 2325–2331.

(58) Wang, T. C.; Rubner, M. F.; Cohen, R. E. Polyelectrolyte Multilayer Nanoreactors for Preparing Silver Nanoparticle Composites:Controlling Metal Concentration and Nanoparticle Size. *Langmuir* **2002**, *18*, 3370–3375.

(59) Bockstaller, M. R.; Lapetnikov, Y.; Margel, S.; Thomas, E. L. Size-Selective Organization of Enthalpic Compatibilized Nanocrystals in Ternary Block Copolymer / Particle Mixtures. *J. Am. Chem. Soc.* **2003**, *125*, 5276–5277.

(60) Chiu, J. J.; Kim, B. J.; Kramer, E. J.; Pine, D. J. Control of Nanoparticle Location in Block Copolymers. *J. Am. Chem. Soc.* **2005**, *127*, 5036–5037.

(61) Chiu, J. J.; Kim, B. J.; Yi, G. R.; Bang, J.; Kramer, E. J.; Pine, D. J. Distribution of Nanoparticles in Lamellar Domains of Block Copolymers. *Macromolecules* **2007**, *40*, 3361–3365.

(62) Jang, S. G.; Kim, B. J.; Hawker, C. J.; Kramer, E. J. Bicontinuous Block Copolymer Morphologies Produced by Interfacially Active, Thermally Stable Nanoparticles. *Macromolecules* **2011**, *44*, 9366–9373.

(63) Kim, B. J.; Bang, J.; Hawker, C. J.; Kramer, E. J. Effect of Areal Chain Density on the Location of Polymer-Modified Gold Nanoparticles in a Block Copolymer Template. *Macromolecules* **2006**, *39*, 4108–4114.

(64) Kim, S.; Yoo, M.; Kang, N.; Moon, B.; Kim, B. J.; Choi, S. H.; Kim, J. U.; Bang, J. Nanoporous Bicontinuous Structures via Addition of Thermally-Stable Amphiphilic Nanoparticles within Block Copolymer Templates. *ACS Appl. Mater. Interfaces* **2013**, *5*, 5659–5666.

(65) Yoo, M.; Kim, S.; Bang, J. Design and Fabrication of Thermally Stable Nanoparticles for Well-Defined Nanocomposites. *J. Polym. Sci. Part B Polym. Phys.* **2013**, *51*, 494–507.

(66) Kim, B. J.; Bang, J.; Hawker, C. J.; Chiu, J. J.; Pine, J.; Jang, S. G.; Yang, S.; Kramer, E. J.; Pine, D. J. Creating Surfactant Nanoparticles for Block Copolymer Composites through Surface Chemistry Creating Surfactant Nanoparticles for Block Copolymer Composites through Surface Chemistry. *Langmuir* **2007**, *23*, 12693–12703.

(67) Hamley, I. W. Nanostructure Fabrication Using Block Copolymers. *Nanotechnology* **2003**, *14*, R39–R54.

(68) Thorkelsson, K.; Mastroianni, A. J.; Ercius, P.; Xu, T. Direct Nanorod Assembly Using Block Copolymer-Based Supramolecules. *Nano Lett.* **2012**, *12*, 498–504.

(69) Ye, T.; Chen, X.; Fan, X.; Shen, Z. Ordered Gold Nanoparticle Arrays Obtained with Supramolecular Block Copolymers. *Soft Matter* **2013**, *9*, 4715–4724.

(70) Zhao, Y.; Thorkelsson, K.; Mastroianni, A. J.; Schilling, T.; Luther, J. M.; Rancatore, B. J.; Matsunaga, K.; Jinnai, H.; Wu, Y.; Poulsen, D.; *et al.* Small-Molecule-Directed Nanoparticle Assembly towards Stimuli-Responsive Nanocomposites. *Nat. Mater.* **2009**, *8*, 979–985.

(71) Lin, Y.; Daga, V. K.; Anderson, E. R.; Gido, S. P.; Watkins, J. J. Nanoparticle-Driven Assembly of Block Copolymers: A Simple Route to Ordered Hybrid Materials. *J. Am. Chem. Soc.* **2011**, *133*, 6513–6516.

(72) Noro, A.; Higuchi, K.; Sageshima, Y.; Matsushita, Y. Preparation and Morphology of Hybrids Composed of a Block Copolymer and Semiconductor Nanoparticles via Hydrogen Bonding. *Macromolecules* **2012**, *45*, 8013–8020.

(73) Song, D.-P.; Lin, Y.; Gai, Y.; Colella, N. S.; Li, C.; Liu, X.-H.; Gido, S.; Watkins, J. J. Controlled Supramolecular Self-Assembly of Large Nanoparticles in Amphiphilic Brush Block Copolymers. *J. Am. Chem. Soc.* **2015**, *137*, 3771–3774.

(74) Wei, Q.; Lin, Y.; Anderson, E. R.; Briseno, A. L.; Gido, S. P.; Watkins, J. J. Additive-Driven Assembly of Block Copolymer-Nanoparticle Hybrid Materials for Solution Processable Floating Gate Memory. *ACS Nano* **2012**, *6*, 1188–1194.

(75) Yao, L.; Lu, X.; Chen, S.; Watkins, J. J. Formation of Helical Phases in Achiral Diblock Copolymers Induced by Small Chiral Additives. *Macromolecules* **2014**, *47*, 6547–6553.

(76) Yao, L.; Lin, Y.; Watkins, J. J. Ultrahigh Loading of Nanoparticles into Ordered Block Copolymer Composites. *Macromolecules* **2014**, *47*, 1844–1849.

(77) Kim, J. U.; O'Shaughnessy, B. Morphology Selection of Nanoparticle Dispersions by Polymer Media. *Phys. Rev. Lett.* **2002**, *89*, 238301.

(78) Thompson, R. B.; Ginzburg, V. V; Matsen, M. W.; Balazs, a C. Predicting the Mesophases of Copolymer-Nanoparticle Composites. *Science.* **2001**, *292*, 2469–2472.

(79) Sheiko, S. S.; Möller, M. Visualization of Macromolecules - A First Step to Manipulation and Controlled Response. *Chem. Rev.* **2001**, *101*, 4099–4123.

(80) Zhang, M.; Müller, A. H. E. Cylindrical Polymer Brushes. *J. Polym. Sci. Part A Polym. Chem.* **2005**, *43*, 3461–3481.

CHAPTER 2

STRONG LIGAND-POLYMER INTERACTION FOR INCORPORATION OF LARGE NANOPARTICLES IN ORDERED COMPOSITE

2.1 Introduction

2.1.1 Block Copolymer Based Nanocomposite Application

Well-ordered block copolymer (BCP) nanocomposite containing inorganic nanoparticles (NP) are of great interest as next generation functional materials with enhanced electronic, optical and magnetic properties.[1–8] The performance of such hybrid materials fundamentally depends on precise control of the spatial organization of the NPs that offer attractive physical properties as determined by particle size, shape, and filling fraction.[1,5] For example, localized surface plasmon resonance (LSPR) and quantum emission of semiconductor NPs displaying size-dependent properties have been applied in bio-sensing and solar energy harvesting.[9–14] Recent development of fine control over NP sizes from a few to tens of nanometers provides new opportunities for fabricating novel functional block polymer-based composite.[15–22]

2.1.2 Size Limitation of Large Nanoparticles in Ordered Composite

A delicate thermodynamic balance between enthalpy and entropy determines the spatial distribution of NPs in a linear BCP.[1,2,5,23,24] The enthalpic contribution arises from the interaction of NP with specific block. Particularly for large NPs, the entropic contributions are often dominated by polymer chain stretching penalties while particles translation entropy is more dominant for smaller NPs.[23–28] Recent work has shown that surface modification of small NPs with core diameter (d_{core}) from 2 to 3 nm is a facile

strategy to localize the NPs selectively within a BCP target domain (domain width L) at d_{core}/L less than 0.2.[29–33] However, by either increasing the loading of such small enthalpically neutral particles or by incorporating large particles with d_{core} over 10 nm, the entropic penalties push the system towards a disorder state.

In spite of successful selective loading small NPs within linear BCPs, it remains challenging to integrate large NPs with core diameter greater than 10 nm into BCP or maintain well ordered composites structures with d_{core}/L greater than 0.3. NP organization with weak or neutral interaction has been studied both theoretically and experimentally. Thompson et al.[27] predicted that for NPs chemically compatible with the A block of an A-*block*-B BCP system, larger NPs (d_{core}/L~0.3) prefer to localize at the center of A domain, while smaller NPs (d_{core}/L~0.2) were preferentially distributed at the interface of the two domains (Figure 2.1 (a)). Bockstaller et al.[25] experimentally observed trends consistent with these simulations by introducing particles modified with aliphatic ligands into poly (styrene-*b*-ethylene propylene) (PS-*b*-PEP). Gold NPs with d_{core}/L~0.06 segregated to the intermaterial dividing surface and silica NPs with d_{core}/L=0.26 mostly localized in the center of the PEP domain (Figure 2.1 (b)). Chiu et al.[29,30] reported a more systematic study in which PS stablized gold NPs were incorporated into symmetric polystyrene-block-poly (2-vinyl pyridine) (PS-*b*-P2VP) BCP with d_{core}/L ranging from 0.035 to 0.12. Particles were localized in the center of the PS domain and their Gaussian distribution width became more narrow with increasing loading of NPs or with decreasing domain width (Figure 2.1 (c)).

Although the distribution of the enthalpically neutral modified NPs within the BCP was studied in detail, the weak interaction between NPs and BCP ultimately limited

d_{core}/L less than 0.3. It is of great interest both from fundamental and application viewpoints to investigate systematically the potential for achieving well-ordered composites with substantially higher d_{core}/L in linear BCP using hydrogen bond-mediated assembly.

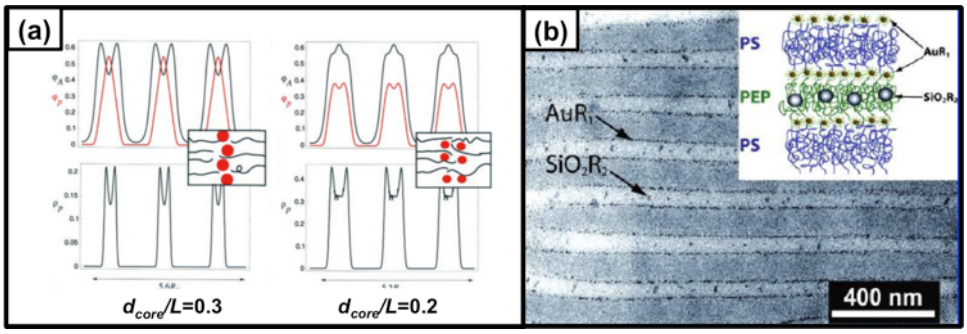

Figure 2.1 NPs distribution in BCP of weak or neutral interactions: (a) simulation results (adapted from reference 27 in Chapter 2), (b) aliphatic NPs distribution (adapted from reference 25 in Chapter 2) in BCP as function of relative size ratio over domain width.

2.1.3 Strong Interaction Meditated Self-Assembly of Block Copolymer and Nanoparticles

Efforts have been dedicated to the enhancement of the NP and BCP surface interaction. For example, Xu et al.[34] have reported the use of a small molecule 3-n-pentadecylphenol (PDP) to connect alkyl chain terminated quantum dots and poly (4-vinly pyridine) (P4VP) domain in a series of PS-*b*-P4VP BCPs (Figure 2.2 (a)). On the other hand, direct hydrogen-bonding (H-bonding) interaction between NPs and BCP domains has been demonstrated by our group[35–37] and others[38–41] (Figure 2.2 (b), (c)). By introducing functional groups on the NP surfaces that exhibit strong interactions with one block of the BCP, the favorable enthalpic interactions between NPs and corresponding block alleviate the BCP chain stretching penalty and enable the very high loading of more than 40 wt % of NPs while maintaining the strong phase segregation in the composite.[35] Recently, our group has demonstrated the directed assembly of large NPs over 15 nm

using an amphiphilic brush BCP with a large domain widths up to 150 nm as the template.[37] Surprisingly, very little work has been directed towards incorporating relative large NP into smaller linear BCP domains by employing favorable interactions between NPs and BCPs. The strong BCP/NP interactions are expected to have the possibilities to offset the entropy penalties upon sequestration of such large obstacles while maintaining the composite ordering.

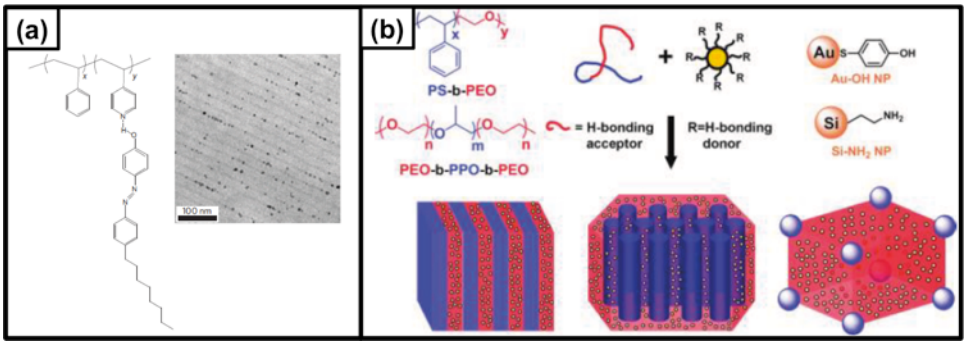

Figure 2.2 Illustration of strong interaction between the NPs and BCPs domains: (a) small molecules additives (adapted from reference 34 in Chapter 2) (b) direct H-bonding (adapted from reference 35 in Chapter 2) of Au NPs and PS-*b*-P2VP BCPs.

2.1.4 Project Overview

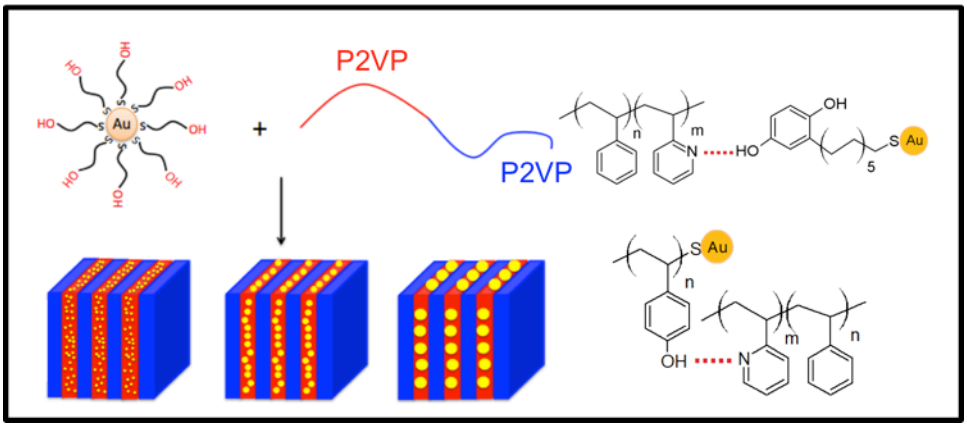

Figure 2.3 Illustration of first project: Au NPs of different core diameter were modified with H-bonding donor group and directed by symmetric PS-*b*-P2VP BCPs. The distributions of Au NPs were systematically investigated as function of size and loading.

This project explores the assembly of hydroxylated gold NPs within linear PS-*b*-P2VP BCPs and quantifies preferential NP segregation in terms of particle core diameter versus domain width (d_{core}/L). We synthesized Au NPs with diameters of 2 nm, 5 nm, 9 nm, and 15 nm and either 2-(11-mercaptoundecyl) hydroquinone or thiol-terminated poly (4-hydroxystyrene) (PHOST) served as hydrogen bonding donor ligands. Pyridine units of the P2VP in symmetric PS-*b*-P2VP functioned as a hydrogen-bonding acceptor as illustrated in Figure 2.3. Ultra large NPs (d_{core} ~ 15 nm) incorporation into linear BCPs was also investigated to under different loading and domain width conditions.

2.2 Experimental

2.2.1 Materials

Sodium borohydride, dodecanethiol (>98%), 2-(11-Mercaptoundecyl) hydroquinone (short for quinone) (95%), acetoxystyrene (96%, inhibitor removed by base aluminum oxides before usage), azobisisobutyronitrile (98%, recrystallized before use), and hexylamine (99%) were purchased from Sigma Aldrich; tetra-n-octylammonium bromide (98%), hydrogen tetrachloroaurate (100%, for traces of metal analysis), octadecanethiol(96%), 2-cyano-2-propyl benzodithioate (97%), and aluminum oxide basic Brockmann I for chromatography 50-200μm, 60A were bought from Acros Organics; sodium citrate (99%-101%) was from Fisher Bioreagents. Hydrochloric acid, ammonium hydroxide, acetic acid, toluene, methanol, ethanol, ethyl ether, hexane, tetrahydrofuran (THF), and N, N-dimethylformamide (DMF) (99.8%) were purchased with guaranteed grade. Symmetric PS-b-P2VP block copolymers were obtained from

Polymer Source, Inc. (Montreal, Canada). The properties of each block copolymer are listed in Table 2.1.

Table 2.1 Molecular information for BCPs used for assemblies

PS-*b*-P2VP	***Mn* (*kg/mol*)**	**P2VP (vol %)**	***Mw/Mn***	L_{P2VP} ***(nm)***
8.2k-*b*-8.3k	16.5	50.3	1.09	7.1
25k-*b*-25k	50	50.0	1.06	15.1
40k-*b*-44k	84	52.4	1.10	25.1
102k-*b*-97k	199	48.7	1.12	36.9

2.2.2 Preparation and Surface Modification of Gold Nanoparticles

Core diameter 2 nm Au NPs modified with quinone were synthesized following established Brust one-phase procedures[17] by replacing methanol with THF. Quinone capped Au NPs with d_{core}~5-9 nm followed the methods of heat treatment by Mikio Miyake et al.[15,18]. Au NPs with core diameter ~ 15 nm were prepared based on one-step water phase Turkevich[42] synthesis procedure. The capping agent sodium citrate was then replaced by PHOST and hydroquinone in order to disperse Au NPs in DMF. PHOST synthesis followed the routine used in previous work.[37] All Au NPs were filtered through 0.2 μm PTFE filter (from VWR) before further usage. A typical ligand exchange went as follows: The hexane was gently removed from 5 mL of 1 wt % purified NPs solution. 2.5 mL hydroquinone (200 mg) THF solution was added into the NP solid. The mixture was sonicated for 20 minutes and stirred for 2 days in order to complete the ligand exchange. The NPs were then washed with 40 mL THF: hexane (volume ratio =1:20) at least three times to remove excess ligand and ODT. Purified NPs was preserved in THF or DMF after purified with 0.2 μm filter for further usage.

2.2.3 Preparation of Symmetric Block Copolymer and Gold Nanoparticles Composite

Au NPs of core diameter from 2 nm to 15 nm with 10 wt %~ 50 wt % were dissolved in freshly prepared PS-*b*-P2VP (~1 wt %) solution with selective solvent. Typically, 2 nm Au NPs composite were prepared in THF solution. 5-9 nm Au NPs composite were prepared as mixture solvent THF: DMF (v:v=3:7). 15 nm Au NPs composite were dissolved in DMF. The NP/BCP composites solution were kept stirring for 2 hours and then dropcast onto glass slides, drying at the room temperature. The obtained films were annealed in saturated chloroform solvent vapor at room temperature for at least 2 days and slowly dried in air for 1 day.

2.2.4 Characterization

The core diameter of Au NPs were characterized by Transmission Electron Microscopy (TEM, JEOL 2000FX, 200 kV) by dropping a dilute nanoparticle solution onto a thin carbon film supported by a copper grid. Au NP size distributions and corresponding histograms were analyzed for a sample size of 300-400 particles with standard image analysis software (Image J). Fourier Transform Infrared (FT-IR) (Perkin Elmer 2000) spectra of ligands and nanoparticles were taken in the range from 4000 cm^{-1} to 650 cm^{-1} in ATR mode. The weight fraction of the gold core was determined by Thermogravemetric Analysis (TGA, TA instrument Q500) from 20 °C to 800 °C at 10 °C/min under air purge flow.

Morphology and domain spacing of neat block copolymer and NP/BCP blends were characterized using Small Angle X-ray Scattering (SAXS). Bulk films of PS-b-P2VP/Au NPs were scraped from glass slides and placed evenly in the center of a metal

washer sandwiched by Kapton tape. These samples were measured on a Ganesha SAXS-LAB instrument (UMass Amherst) with Cu Kα 0.154 nm line on SAXS or ESAXS mode. Room-temperature microtoming (Leica Ultracut microtome) was used to cut the nanocompsite bulk film into 50 nm thin films, and sections collected using a carbon film supported by copper grids. For the samples containing d_{core}~9-15 nm Au NPs, subsequent Iodine selective staining was applied to P2VP domains to improve PS/P2VP domain contrast. The prepared thin films of NP/BCP composites were then characterized by TEM (JEOL 2000FX, 200kV).

2.3 Results and Discussions

2.3.1 Size Distribution and Surface Stabilizer of Gold Nanoparticles

Au NPs mean core diameters (d_{core}) and standard deviations are presented in Figure 2.4. FT-IR spectra (Figure 2.5) of NPs resemble that of the hydroquinone or PHOST ligands bounds to the particles' surfaces. Less intense S-H band at 2550 cm^{-1} are present in the spectrum of the hydroquinone ligand and are not evident in hydroquinone capped Au NPs spectra, indicating that the thiol bond has dissociated while Au-S bond formed. The broad peak at 3300-3400 cm^{-1} suggests the existence of hydroxyl groups on the NPs surface (Figure 2.5 (A)). Complete deesterification of poly (4-acetoxystyrene) is indicated by the disappearance of C=O characteristic band at 1755 cm^{-1} as well as the presence of a broad O-H peak at 3300 cm^{-1} in the spectrum of PHOST (Figure 2.5 (B)).[37] The appearance of characteristic band of PHOST in NP spectrum indicates the successful attachment of PHOST onto the NPs surfaces.

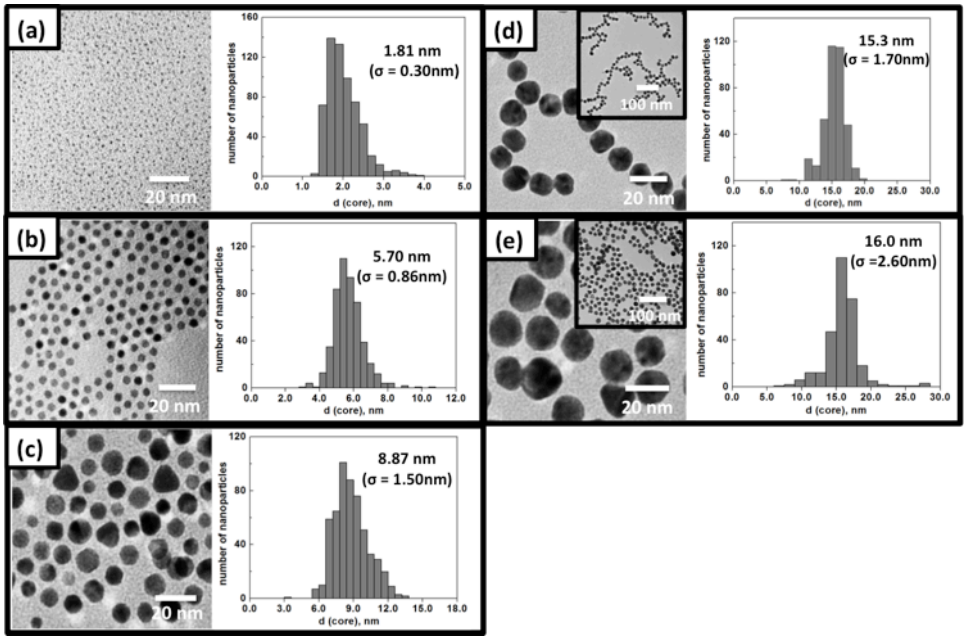

Figure 2.4 TEM images and core diameter histograms of synthesized hydroxylated gold NPs; hydroquinone stabilized Au NPs (a) 1.81±0.30, (b) 5.70 ±0.86, (c) 8.87±1.50, (d) 15.3±1.70 nm and (e) PHOST capped Au NPs 16.0±2.60 nm accordingly.

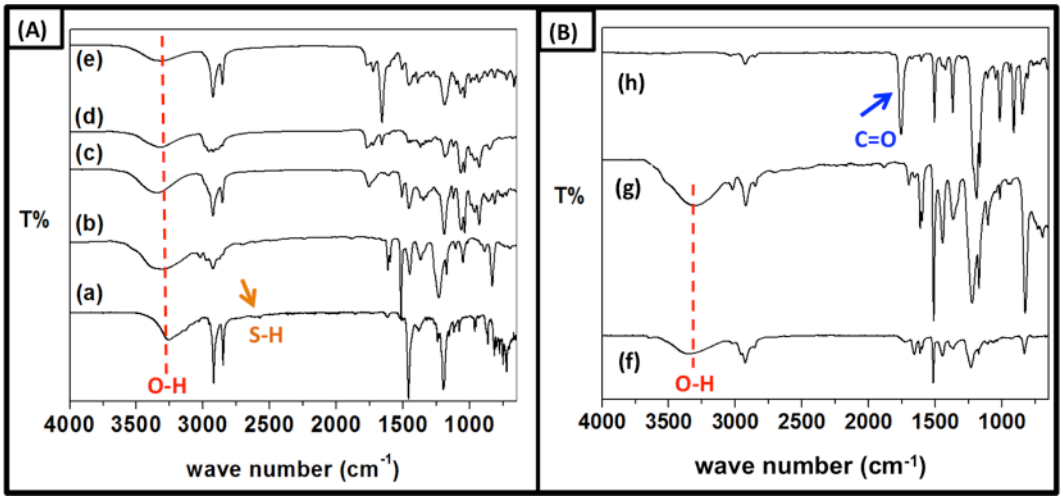

Figure 2.5 FT-IR spectra of sets (A): (a) hydroquinone, hydroquinone coated Au NPs with average size (b) 1.81 (c) 5.70, (d) 8.87, (e) 15.3 nm. FT-IR spectra of sets (B): (f) PHOST coated Au NPs with d_{core} 16.0 nm, (g) poly (4-vinylphenol) (PHOST) and (h) poly (4-acetoxystyrene).

Au NPs ligand densities are listed in Table 2.2. The calculations are based on core weight fraction measured by TGA, the number of hydroxyl groups per unit of PHOST (~25, PHOST M_n~3.2 kg/mol, PDI~1.09, synthesized by Dr. Dongpo Song) and

hydroquinone (~2), as well as the densities of the components (PS-*b*-P2VP ~ 1.05 g/cm^3, gold ~19.3 g/cm^3, PHOST~ 1.16 g/cm^3 and hydroquinone ~ 1.052 g/cm^3).[35,37] Hydroxyl group density is particularly higher for NP-15.3 due to the ineffective stabilization of large NPs with a small molecule thiol. To avoid NPs aggregation, the addition of excess hydroquinone inevitably leads to the presence of free ligands and thus an increase in the number of H-bonding donor groups (both free and bound). We also noticed that using the number of hydroxyl group to estimate the enthapic contribution has several issues. For example, the H-bonding has direction and saturation; the number of hydroxyl groups is more than the number of hydrogen bonds between particles and block copolymer due to particles self-interaction and the existence of free ligand. In spite of these issues, earlier work[35,36,38,39] has reported that the favorable H-bonding interactions between NPs and corresponding block enhanced the microphase segregation to alleviate the BCP chain-stretching penalty in different systems. The hydroxyl group density of ligands stabilized Au NPs in this system are high enough to yield adequate interaction with P2VP domain.

Table 2.2 Properties of Au NPs: samples from (a) to (d) stabilized with hydroquinone and (e) capped with PHOST

NP	Aver d_{core} (nm)	Core weight (%)	Ligand density (per nm^2)	Hydroxyl group density (per nm^2)
NP-1.81	1.80	19.5	48.8	97.6
NP-5.70	5.70	29.2	90.3	181
NP-8.87	8.87	40.8	83.5	167
NP-15.3	15.3	10.6	843	1690
NP-16.0	16.0	67.2	4.70	118

The volume fraction of NPs in the composite varies among particles batches, and Table 2.3 provides the detailed information. The organic ligands of NPs were included during the calculation.

Table 2.3 Au NPs volume fraction in hybrid composite

NP-1.81 loading	ϕ_{NP}	$\phi_{NP+p2vp}$	**NP-5.70 loading**	ϕ_{NP}	$\phi_{NP+p2vp}$	**NP-8.87 loading**	ϕ_{NP}	$\phi_{NP+p2vp}$
0.10	0.08	0.54	0.10	0.07	0.54	0.10	0.06	0.53
0.20	0.17	0.58	0.20	0.15	0.58	0.20	0.13	0.57
0.30	0.26	0.63	0.30	0.24	0.62	0.30	0.21	0.60
0.40	0.35	0.68	0.40	0.33	0.66	0.40	0.29	0.65
0.50	0.45	0.72	0.50	0.42	0.71	0.50	0.38	0.69
NP-15.0 loading	ϕ_{NP}	$\phi_{NP+p2vp}$	**NP- 16.0 loading**	ϕ_{NP}	$\phi_{NP+p2vp}$			
0.10	0.09	0.55	0.10	0.04	0.52			
0.20	0.18	0.59	0.20	0.08	0.54			
0.30	0.28	0.64	0.30	0.13	0.56			
0.40	0.37	0.69	0.40	0.18	0.59			
0.50	0.47	0.74	0.50	0.25	0.63			

2.3.2 Gold Nanoparticles Distribution in Terms of Size Variation

To demonstrate NPs distributions, TEM images of composite samples are presented for a range of particle core diameters (d_{core}) and P2VP domain widths L (Figure 2.6). Consider the assembly of NP-1.81/BCP as one example (Figure 2.6 (a) to (d)), the d_{core}/L ratios for these samples were less than 0.3 (from 0.049 to 0.25). NP-1.81 and NP-5.70 composites were unstained and contrast in the images only came from the electron density difference between metal core and polymer matrix. With core diameter increasing to 5.70 nm, NPs became centralized in the domain with d_{core}/L greater than 0.3 but remained uniformly distributed in larger domains at which d_{core}/L is 0.23 and 0.15 (Figure 2.6 (e) to (h)). The incorporation of NP-5.70 into 7.1 nm domains, resulting in a significantly increasing d_{core}/L to 0.8 in BCP/NP assembly with an inter-particle distance less than 10 nm is noteworthy. Larger NPs (samples were then stained with Iodine to increase domain contrast) were more apparently pushed toward the center of the P2VP domains for most d_{core}/L ratios greater than 0.3 (Figure 2.6 (i) to (p)).

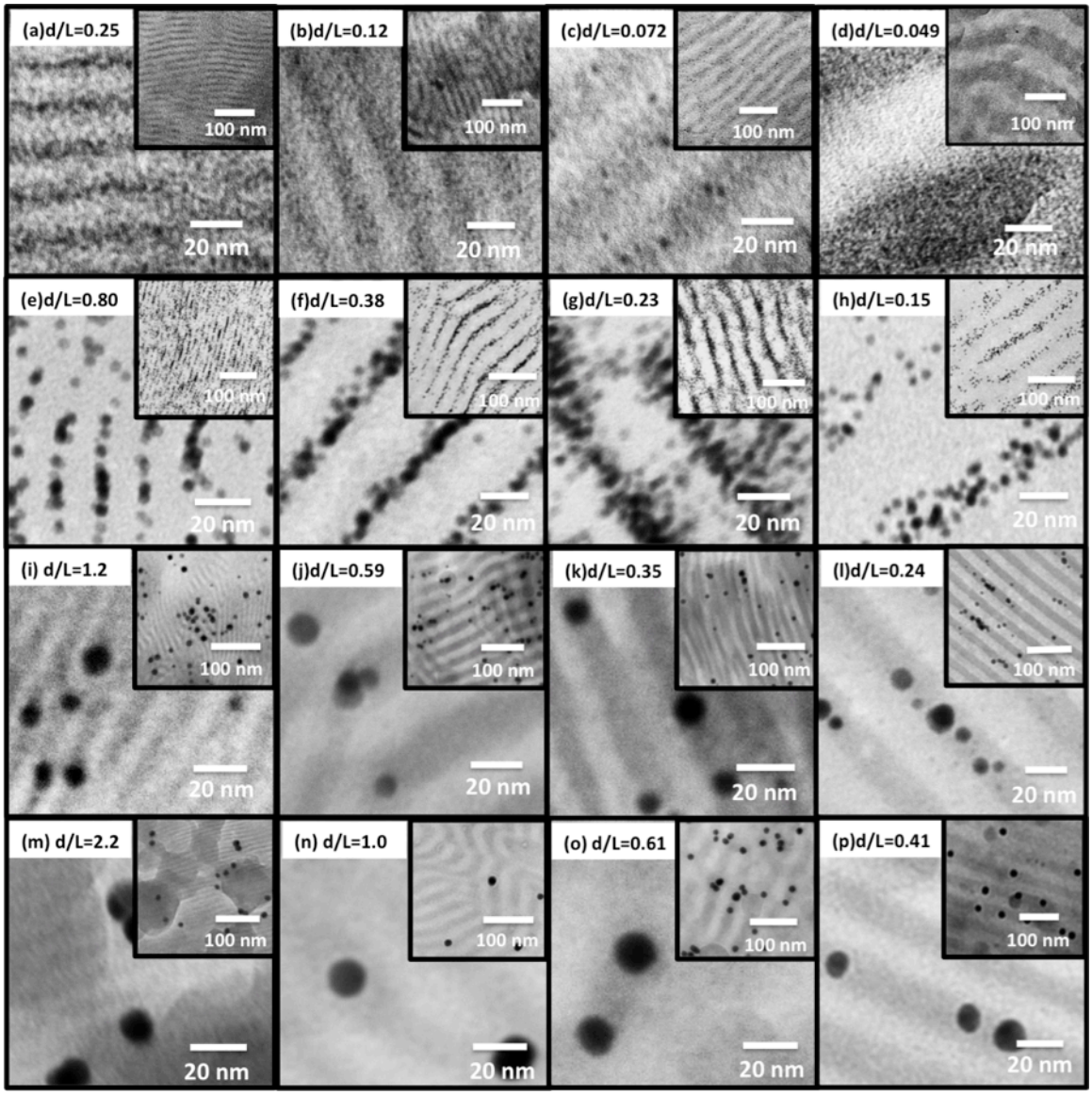

Figure 2.6 TEM images of NP-1.81 blends (a)-(d), NP-5.70 blends (e)-(h), NP-8.87 blends (i)-(l), and NP-15.3 blends (m)-(p) with linear symmetric PS-*b*-P2VP block copolymer of *Mn* (total) (a) 16.5, (b) 50, (c) 84, (d) 199 kg/mol. NPs volume fraction (including organic component) ~ 9 vol %-17 vol % (20 wt % from (a) to (l), 10 wt % from (m) to (p)).

Figure 2.6 (a), (e), (i) and (m) confirms the particles distribution transition, in which the particles were pushed toward to center of domain with increasing d_{core}/L. For NP-8.87, which had a core diameter slightly larger than the P2VP domain size (7.1 nm), Y-shape defects occured in the nanocompostie (Figure 2.6 (i)). In Figure 2.6 (m), NPs

were expelled out of the polymer domain with d_{core}/L over than 2, while the BCP maintains its lamellar structure.

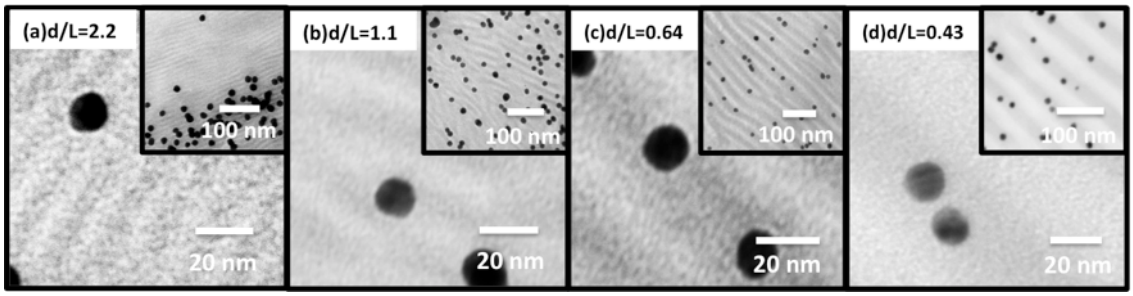

Figure 2.7 TEM images of NP-16.0 blends with linear symmetric PS-*b*-P2VP of *Mn* (total) (a) 16.5, (b) 50, (c) 84, (d) 199 kg/mol. NPs volume fraction ~ 4 vol % (10 wt %). The P2VP domains are lightly stained with iodine to increase domain contrast.

Figure 2.7 shows that linear block copolymer templates direct the distribution of d_{core}~16.0 nm PHOST coated Au NPs. The NPs were by definition larger than the block domain at d_{core}/L~2, but clearly reside at the center of the domain with d_{core}/L~0.64. A lamellar morphology is observed with a d_{core}/L of 0.4 and particles were not restricted to center of the P2VP domain. Figure 2.6 and Figure 2.7 suggest that large NPs (d_{core} ~15 nm) distributions in linear BCP are mainly dependent of relative size between NPs and block domain rather than their surface stabilizer.

The corresponding SAXS spectra are shown in Figure 2.8, and domain spacing was calculated from the primary order peak using equation $d=2\pi/q^*$. Unfortunately, SAXS (Figure 2.8 (D)) does not provide structure information for NP-15.3 and BCP composite. The high scattering cross-section of the 15 nm Au NPs produced strong background scattering and made the resolution of signal generated from the NP/BCP blends quite difficult.

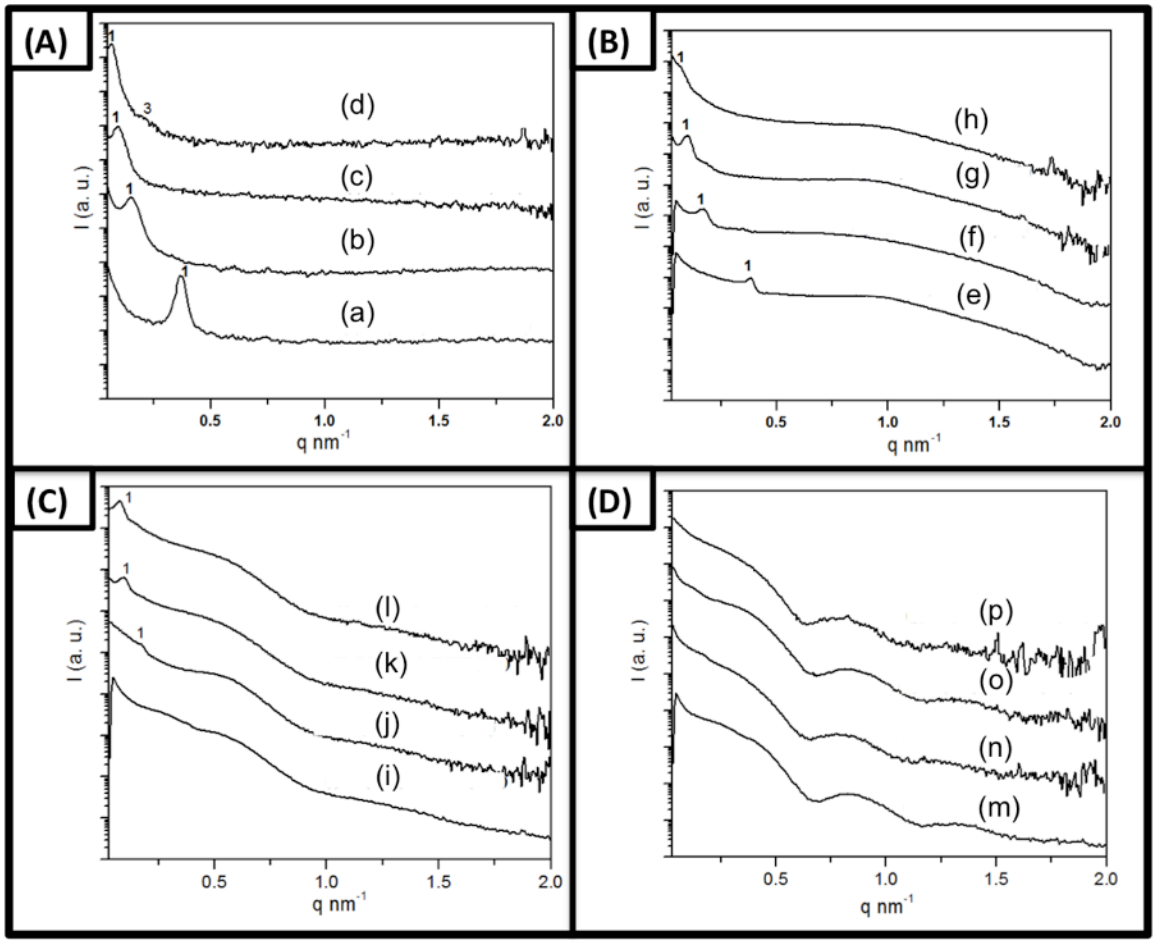

Figure 2.8 SAXS spectra of (A) NP-1.81 blends (a)-(d), (B) NP-5.70 blends (e)-(h), (C) NP-8.87 blends (i)-(l), and (D) NP-15.3 blends (m)-(p) with linear symmetric PS-*b*-P2VP of *Mn* (total) (a) 16.5, (b) 50, (c) 84, (d) 199 kg/mol. NPs volume fraction (including organic component) 9 vol %-17 vol % (20 wt % from (a) to (l), 10 wt % from (m) to (p)).

2.3.3 Gold Nanoparticles Distribution in Terms of Loading

Figure 2.9 shows NP distribution with increasing loading of Au NPs. PS (25k)-*b*-P2VP (25k) BCP formed an ordered lamella structure with up to 26 vol % (30 wt %) d_{core}~1.81 nm Au NPs, but underwent a morphology transition at a NP loading concentration of 35 vol % (40 wt %). The system was disordered upon incorporation of 45 vol % (50 wt %) Au NPs. As no staining is used in these samples, the high contrast

from gold core indicates that the NPs were uniformly distributed in block domain in regardless of loading.

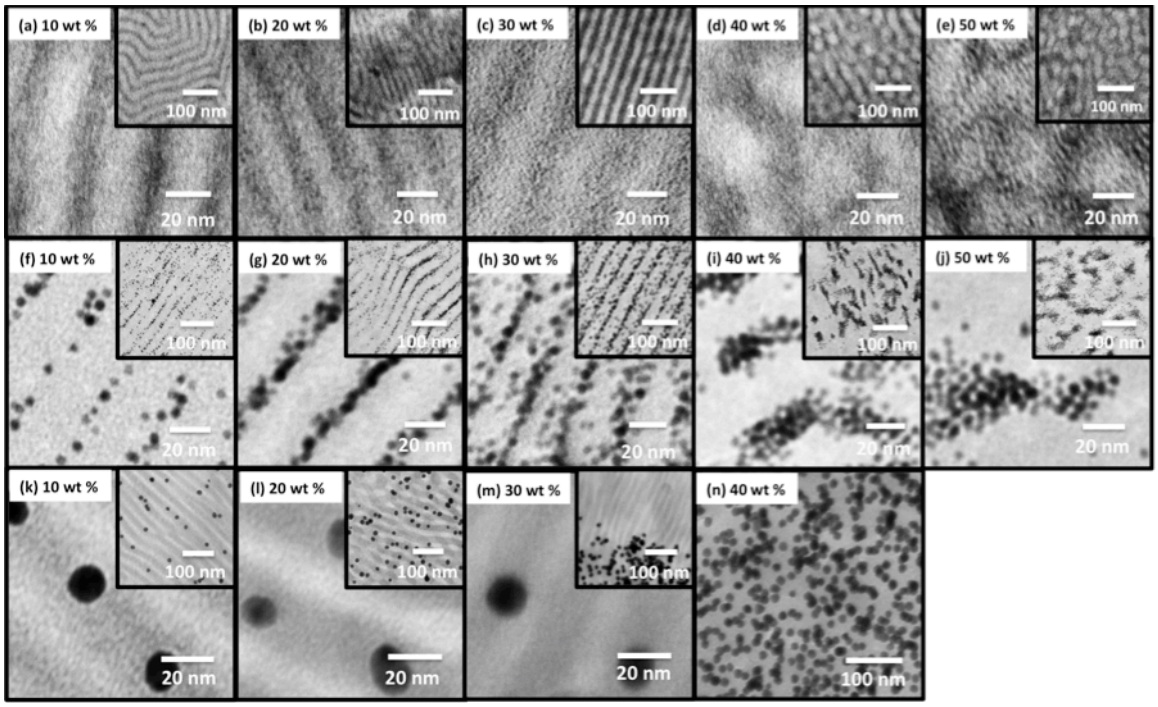

Figure 2.9 TEM images of NP-1.81 blends with PS(25k)-b-P2VP(25k) *(d_{core}/L*~0.12) with NPs volume fraction (including organic component) from 8 vol % to 45 vol %: (a) 10 wt %, (b) 20 wt %, (c) 30 wt % (d) 40 wt % (e) 50 wt %; TEM images of NP-5.70 blends with PS(25k)-b-P2VP(25k) (d_{core}/L~0.38) with volume fraction (including organic component) from 7 vol % to 42 vol % : (f) 10 wt %, (g) 20 wt %, (h) 30 wt % (i) 40 wt % (j) 50 wt %; TEM images of NP-16.0 blends with PS(40k)-b-P2VP(44k) (d_{core}/L~0.61) with NPs volume fraction (including organic component) from 4 vol % to 18 vol %: (k) 10 wt %, (l) 20 wt %, (m) 30 wt % (n) 40 wt %; samples from (k) to (n) are stained with Iodine to increase domain contrast. Ordered structured remained with NPs volume fraction up to ~ 25 vol % (with organic ligands).

Figures 2.9 ((f) to (j)) show the structures of NP-5.70 and PS (25k)-*b*-P2VP (25k) BCP composites. Well-ordered lamellar structures were observed again by incorporating up to 24 vol % (30 wt %). Self-aggregation of NPs appeared at loadings over 28 vol % (40 wt %). We also noted that the NPs were centralized within the target domain at low loading, and gradually spread to the domain edges as more particles were loaded in the BCP. The structure of NP-16.0 and PS (40k)-*b*-P2VP (44k) nanocomposites were shown

in Figure 2.9 (k) to (n). It is noteworthy to point out the lamellae structure at NPs loading less than 8 vol % (20 wt %), confirming that the linear block copolymer is useful as a template to guide large NPs assemblies.

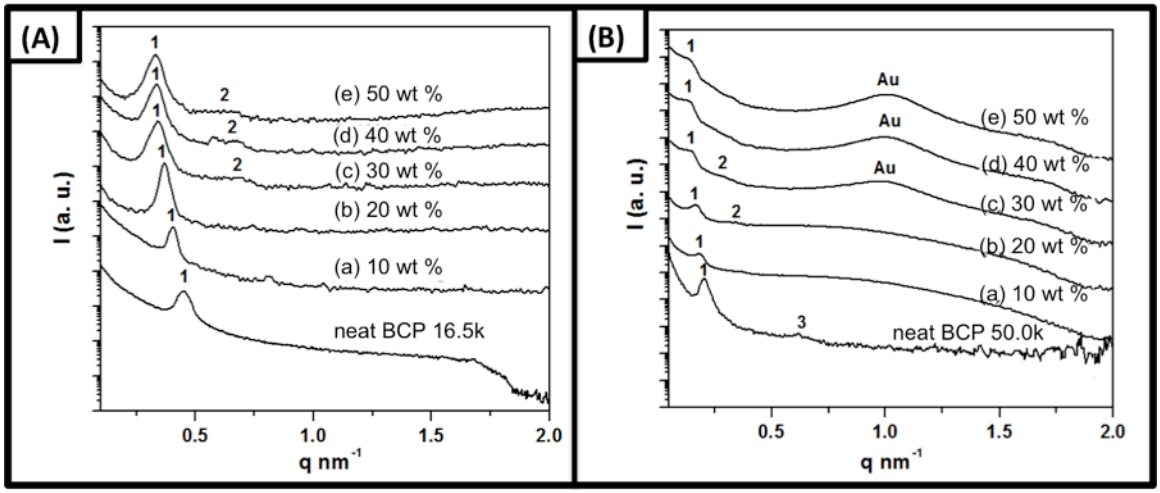

Figure 2.10 (A): SAXS spectra of blends of PS (25k)-*b*-P2VP (25k) with NP-1.81 at different volume fraction (including organic component) from 8 vol % to 45 vol %: (a) 10 wt %, (b) 20 wt %, (c) 30 wt % (d) 40 wt % (e) 50 wt % with d_{core}/L~0.12; (B): SAXS profiles of blends based on the same BCP containing NP-5.70 (d_{core}/L~0.38) with NPs volume fraction (including organic component) from 7 vol % to 42 vol % : (f) 10 wt %, (g) 20 wt %, (h) 30 wt % (i) 40 wt % (j) 50 wt %.

Figure 2.10 shows a shift of the primary peaks to lower q values with the increasing loading of NPs, indicating a swelling of the target domains due to a selective incorporation of NPs within P2VP domains. As shown in Figure 2.10 (A), the domain spacing was increased from 30 to 40 nm as calculated according to the q values for the primary peak ($d = 2\pi/q^*$). A symmetric lamellar morphology formed in the neat BCP sample as indicated by the higher order reflections at 3q. In contrast, an asymmetric lamellar morphology was observed in the composite samples containing NPs 8 vol % ~ 26 vol % (10 wt % ~ 30 wt %). Moreover, a morphology transition from lamellae to cylinder was achieved at a high NP loading of up to 35 vol % (40 wt %) (Fig. 2.10 (A)). A further increasing of NP loading to 45 vol % (50 wt %) resulted in a disordered state.

Upon addition of larger NPs (Fig. 2.10(B)), self-aggregation occurs and phase segregation and order within the composites are compromised, as verified by more intense NPs scattering intensity and a less intense 1st order peak at 42 vol % (50 wt %) loading of NPs.

2.3.4 Summary

A number of studies have explored the thermodynamic balance of NP/BCP assemblies.[1,2,5,43] Generally, the enthapic contribution is governed by the interactions between the NPs and BCPs, while polymer chain stretching as well as NP translation upon mixing influence the entropic contribution. H-bonding meditated assembly provides favorable enthalpic interactions that can promote strong phase segregation in the NP and BCP composite. Figure 2.11 summarizes the nature and distribution of NPs in the composites at specific d_{core}/L values based on TEM image analysis.

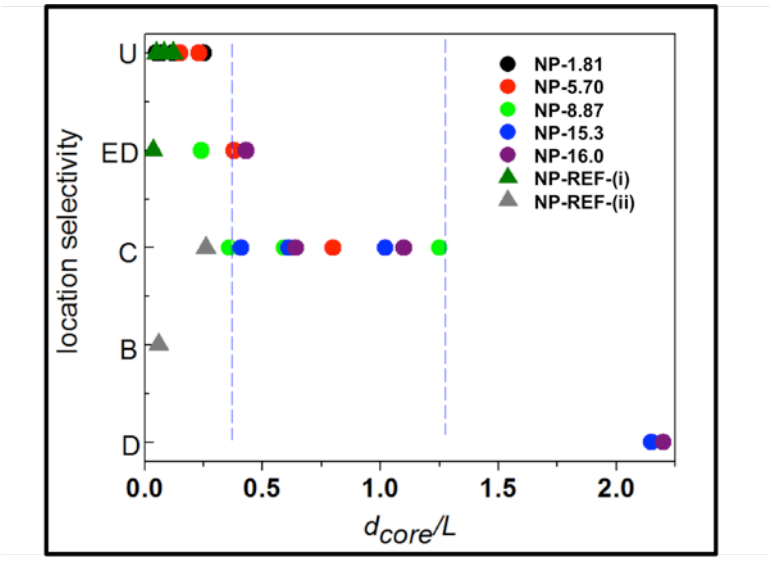

Figure 2.11 (a) Relationship between d_{core}/L and NPs location as indicated by labels: U = uniform distribution, ED=edge diffused, C=centered distribution, B=interface/boundary of domain, D=disorder/ NPs expelled from domain. The analysis TEM images are from Figure 2.6 and Figure 2.7. NP-REF-(i) (reference 25) and NP-REF-(ii) (reference 30 in Chapter 2) are representative NPs distribution of neutral/weak NP/BCP interactions.

The behavior can be summarized as follows.

For $0<d_{core}/L<0.3$, the favorable enthalpic interactions effectively offset the entropy penalty and the relatively small NPs are easily accommodated up to relatively high NP loadings. The NPs are uniformly distributed in the target domain. And the uniform distribution in selective domain differs from systems with relatively weak interactions in which NPs distribution is biased towards the center of the target (d_{core}/L up to 0.12).[29–31] The surface modification of neutral or mixture ligand may also introduce particles locate at the interface of two domains at low d_{core}/L (less than 0.2), also significantly different from a H-bonding interaction system with selective incorporation of nanoparticles.[35,37]

At $0.3< d_{core}/L< 0.5$, as the relative NP size increases, entropy begins to play a prominent role in the spatial organization of the NPs. Initially, with low loading of NPs, the NPs distribute towards the center of the target domain in order to reduce entropic penalty by minimizing chain stretching through localization near chain ends.[27,30] The favorable enthalpic contribution of the strong interactions enable the incorporation of additional NPs into the domain but the NPs have to increasingly be accommodated in less preferred regions near the domain edges. Once NPs saturate the domain further addition of NPs results in aggregation and macrophase separation.

At $0.5 < d_{core}/L < 1$. Entropic penalties become significant and begin to dominate as the NPs size becomes comparable to the domain width. While the favorable interactions enable the accommodation of NPs within the target domains, the loadings concentrations are not as high as those of composite containing smaller NPs. Our

experimental results indicate that well-ordered lamellar morphologies can be observed in NP/BCP blends at d_{core}/L ~0.8 with less than 15 vol % (20 wt %) NP (Figure 2.6 (f)).

$1 < d_{core}/L$. NPs with core diameter size similar or larger than domain width increase the NP/BCP mixture entropy significantly. Under these conditions, the distortion of domain and chain stretching required to incorporate the NPs causes X, Y or T shape defects, consistent with simulation results.[44] In many cases, NPs are expelled out of the domain as free energy does not favor the assembly and NPs only attach interface of the two blocks by hydrogen-bonding interaction.

In summary, hydroxylated Au nanoparticles with narrow size distributions have been synthesized over a wide range of particle diameters and selectively incorporated within the target domains of linear block copolymers to reveal NP spatial distribution in composites with hydrogen-bonding interactions between the NPs and BCP chain segments. At small values of d_{core}/L~0.1, the particles are nearly homogeneously distributed within the target domains. As particle size increases relative to the target domain width (d_{core}/L over 0.3), the NP locations are initially biased towards the domain center at low concentrations and then are accommodated in less energetically preferred locations nearer the domain boundaries as NP loading increases. Favorable enthalpic introduction by H-bonding offset entropic penalties mainly arising from chain stretching upon incorporation of large NPs. We successfully employ symmetric linear block copolymer as template to incorporate 15 nm Au NPs and increase d_{core}/L to 0.8 while maintaining well-ordered lamellar structure in NP/BCP composites. This systematic study provides a guide for a precise control on NP-size-tunable NP/BCP hybrid materials in the presence of strong enthalpic interactions.

The contents of Chapter 2 have been published in *Macromolecules*, **2016**, *49*, 3352-3360.

2.4 References

(1) Balazs, A. C.; Emrick, T.; Russell, T. P. Nanoparticle Polymer Composites: Where Two Small Worlds Meet. *Science.* **2006**, *314*, 1107–1110.

(2) Bockstaller, M. R.; Mickiewicz, R. a.; Thomas, E. L. Block Copolymer Nanocomposites: Perspectives for Tailored Functional Materials. *Adv. Mater.* **2005**, *17*, 1331–1349.

(3) Huynh, W. U.; Dittmer, J. J.; Alivisatos, A. P. Hybrid Nanorod-Polymer Solar Cells. *Science.* **2002**, *295*, 2425–2427.

(4) Jaramillo, T. F.; Baeck, S. H.; Cuenya, B. R.; McFarland, E. W. Catalytic Activity of Supported Au Nanoparticles Deposited from Block Copolymer Micelles. *J. Am. Chem. Soc.* **2003**, *125*, 7148–7149.

(5) Kao, J.; Thorkelsson, K.; Bai, P.; Rancatore, B. J.; Xu, T. Toward Functional Nanocomposites: Taking the Best of Nanoparticles, Polymers, and Small Molecules. *Chem. Soc. Rev.* **2013**, *42*, 2654–2678.

(6) Lopes, W. A.; Jaeger, H. M. Hierarchical Self-Assembly of Metal Nanostructures on Diblock Copolymer Scaffolds. *Nature* **2001**, *414*, 735–738.

(7) Rosa, C. De; Auriemma, F.; Girolamo, R. Di; Pepe, G. P.; Napolitano, T.; Scaldaferri, R. Enabling Strategies in Organic Electronics Using Ordered Block Copolymer Nanostructures. *Adv. Mater.* **2010**, *22*, 5414–5419.

(8) Xiang, J.; Lu, W.; Hu, Y.; Wu, Y.; Yan, H.; Lieber, C. M. Ge/Si Nanowire Heterostructures as High-Performance Field-Effect Transistors. *Nature* **2006**, *441*, 489–493.

(9) Choi, C. L.; Alivisatos, a P. From Artificial Atoms to Nanocrystal Molecules: Preparation and Properties of More Complex Nanostructures. *Annu. Rev. Phys. Chem.* **2010**, *61*, 369–389.

(10) K. Huang, H. Ma, J. L. et. a. Size-Dependent Localization and Pene- Tration of Ultrasmall Gold Nano- Particles in Cancer Cells, Multicellular Spheroids, and Tumors in Vivo. *ACS Nano* **2012**, *6*, 4483–4493.

(11) Ku, K. H.; Shin, J. M.; Kim, M. P.; Lee, C. H.; Seo, M. K.; Yi, G. R.; Jang, S. G.; Kim, B. J. Size-Controlled Nanoparticle-Guided Assembly of Block Copolymers for Convex Lens-Shaped Particles. *J. Am. Chem. Soc.* **2014**, *136*, 9982–9989.

(12) Link, S.; El-Sayed, M. a. Size and Temperature Dependence of the Plasmon Absorption of Colloidal Gold Nanoparticles. *J. Phys. Chem. B* **1999**, *103*, 4212–4217.

(13) Sarangi, S. N.; Hussain, a. M. P.; Sahu, S. N. Strong UV Absorption and Emission from L-Cysteine Capped Monodispersed Gold Nanoparticles. *Appl. Phys. Lett.* **2009**, *95*, 73109.

(14) Talapin, D. V.; Lee, J.-S.; Kovalenko, M. V.; Shevchenko, E. V. Prospects of Colloidal Nanocsrystals for Electronic and Optoelectronic Applications. *Chem. Rev.* **2010**, *110*, 389–458.

(15) Shimizu, T.; Teranishi, T.; Hasegawa, S.; Miyake, M. Size Evolution of Alkanethiol-Protected Gold Nanoparticles by Heat Treatment in the Solid State. *J. Phys. Chem. B* **2003**, *107*, 2719–2724.

(16) Sabir, T. S.; Rowland, L. K.; Milligan, J. R.; Yan, D.; Aruni, A. W.; Chen, Q.; Boskovic, D. S.; Kurti, R. S.; Perry, C. C. Mechanistic Investigation of Seeded Growth in Triblock Copolymer Stabilized Gold Nanoparticles. *Langmuir* **2013**, *29*, 3903–3911.

(17) Brust, M.; Fink, J.; Bethell, D.; Schiffrin, D. J.; Kiely, C. Synthesis and Reactions of Functionalised Gold Nanoparticles. *J. Chem. Soc. Chem. Commun.* **1995**, 1655–1656.

(18) Brust, M.; Walker, M.; Bethell, D.; Schiffrin, D. J.; Whyman, R. Synthesis of Thiol-Derivatised Gold Nanoparticles in a Two-Phase Liquid-Liquid System. *J.Chem. Soc.,Chem. Commun.* **1994**, 801–802.

(19) Jana, N. R.; Gearheart, L.; Murphy, C. J. Seeding Growth for Size Control of 5-40 Nm Diameter Gold Nanoparticles. *Langmuir* **2001**, *17*, 6782–6786.

(20) Johnson, S. R.; Evans, S. D.; Brydson, R. Influence of a Terminal Functionality on the Physical Properties of Surfactant-Stabilized Gold Nanoparticles. *Langmuir* **1998**, *14*, 6639–6647.

(21) Kanaras, A. G.; Kamounah, F. S.; Schaumburg, K.; Kiely, C. J.; Brust, M. Thioalkylated Tetraethylene Glycol: A New Ligand for Water Soluble Monolayer Protected Gold Clusters. *Chem. Commun.* **2002**, 2294–2295.

(22) Liu, X.; Xu, H.; Xia, H.; Wang, D. Rapid Seeded Growth of Monodisperse, Quasi-Spherical, Citrate- Stabilized Gold Nanoparticles via H 2 O 2 Reduction. *Langmuir* **2012**, 13720–13726.

(23) Huh, J.; Ginzburg, V. V.; Balazs, A. C. Thermodynamic Behavior of Particle/diblock Copolymer Mixtures: Simulation and Theory. *Macromolecules* **2000**, *33*, 8085–8096.

(24) Lee, J.-Y.; Thompson, R. B.; Jasnow, D.; Balazs, A. C. Entropically Driven Formation of Hierarchically Ordered Nanocomposites. *Phys. Rev. Lett.* **2002**, *89*, 155503.

(25) Bockstaller, M. R.; Lapetnikov, Y.; Margel, S.; Thomas, E. L. Size-Selective Organization of Enthalpic Compatibilized Nanocrystals in Ternary Block Copolymer / Particle Mixtures. *J. Am. Chem. Soc.* **2003**, *125*, 5276–5277.

(26) Kim, J. U.; O'Shaughnessy, B. Morphology Selection of Nanoparticle Dispersions by Polymer Media. *Phys. Rev. Lett.* **2002**, *89*, 238301.

(27) Thompson, R. B.; Ginzburg, V. V; Matsen, M. W.; Balazs, a C. Predicting the Mesophases of Copolymer-Nanoparticle Composites. *Science.* **2001**, *292*, 2469–2472.

(28) Yoo, M.; Kim, S.; Bang, J. Design and Fabrication of Thermally Stable Nanoparticles for Well-Defined Nanocomposites. *J. Polym. Sci. Part B Polym. Phys.* **2013**, *51*, 494–507.

(29) Chiu, J. J.; Kim, B. J.; Kramer, E. J.; Pine, D. J. Control of Nanoparticle Location in Block Copolymers. *J. Am. Chem. Soc.* **2005**, *127*, 5036–5037.

(30) Chiu, J. J.; Kim, B. J.; Yi, G. R.; Bang, J.; Kramer, E. J.; Pine, D. J. Distribution of Nanoparticles in Lamellar Domains of Block Copolymers. *Macromolecules* **2007**, *40*, 3361–3365.

(31) Jang, S. G.; Kim, B. J.; Hawker, C. J.; Kramer, E. J. Bicontinuous Block Copolymer Morphologies Produced by Interfacially Active, Thermally Stable Nanoparticles. *Macromolecules* **2011**, *44*, 9366–9373.

(32) Kim, B. J.; Bang, J.; Hawker, C. J.; Chiu, J. J.; Pine, J.; Jang, S. G.; Yang, S.; Kramer, E. J.; Pine, D. J. Creating Surfactant Nanoparticles for Block Copolymer Composites through Surface Chemistry Creating Surfactant Nanoparticles for Block Copolymer Composites through Surface Chemistry. *Langmuir* **2007**, *23*, 12693–12703.

(33) Kim, S.; Yoo, M.; Kang, N.; Moon, B.; Kim, B. J.; Choi, S. H.; Kim, J. U.; Bang, J. Nanoporous Bicontinuous Structures via Addition of Thermally-Stable Amphiphilic Nanoparticles within Block Copolymer Templates. *ACS Appl. Mater. Interfaces* **2013**, *5*, 5659–5666.

(34) Zhao, Y.; Thorkelsson, K.; Mastroianni, A. J.; Schilling, T.; Luther, J. M.; Rancatore, B. J.; Matsunaga, K.; Jinnai, H.; Wu, Y.; Poulsen, D.; *et al.* Small-Molecule-Directed Nanoparticle Assembly towards Stimuli-Responsive Nanocomposites. *Nat. Mater.* **2009**, *8*, 979–985.

(35) Lin, Y.; Daga, V. K.; Anderson, E. R.; Gido, S. P.; Watkins, J. J. Nanoparticle-Driven Assembly of Block Copolymers: A Simple Route to Ordered Hybrid Materials. *J. Am. Chem. Soc.* **2011**, *133*, 6513–6516.

(36) Yao, L.; Lin, Y.; Watkins, J. J. Ultrahigh Loading of Nanoparticles into Ordered Block Copolymer Composites. *Macromolecules* **2014**, *47*, 1844–1849.

(37) Song, D.-P.; Lin, Y.; Gai, Y.; Colella, N. S.; Li, C.; Liu, X.-H.; Gido, S.; Watkins, J. J. Controlled Supramolecular Self-Assembly of Large Nanoparticles in Amphiphilic Brush Block Copolymers. *J. Am. Chem. Soc.* **2015**, *137*, 3771–3774.

(38) Jang, S. G.; Khan, A.; Hawker, C. J.; Kramer, E. J. Morphology Evolution of PS-B-P2VP Diblock Copolymers via Supramolecular Assembly of Hydroxylated Gold Nanoparticles. *Macromolecules* **2012**, *45*, 1553–1561.

(39) Jang, S. G.; Kramer, E. J.; Hawker, C. J. Controlled Supramolecular Assembly of Micelle-like Gold Nanoparticles in PS-b-P2VP Diblock Copolymers via Hydrogen Bonding. *J. Am. Chem. Soc.* **2011**, *133*, 16986–16996.

(40) Ye, T.; Chen, X.; Fan, X.; Shen, Z. Ordered Gold Nanoparticle Arrays Obtained with Supramolecular Block Copolymers. *Soft Matter* **2013**, *9*, 4715–4724.

(41) Yeh, S.; Wei, K.; Sun, Y.; Jeng, U.; Liang, K. S. Morphological Transformation of PS-B-PEO Diblock Copolymer by Selectively Dispersed Collidal CdS Quantum Dots. *Macromolecules* **2003**, *36*, 7903–7907.

(42) Enustun, B. V.; Turkevich, J. Coagulation of Colloidal Gold. *J. Am. Chem. Soc.* **1963**, *85*, 3317–3328.

(43) Tyagi, S.; Lee, J. Y.; Buxton, G. A; Balazs, A. C. Using Nanocomposite Coatings To Heal Surface Defects. *Macromolecules* **2004**, *37*, 9160–9168.

(44) Kim, Y.; Chen, H.; Alexander-Katz, A. Free Energy Landscape and Localization of Nanoparticles at Block Copolymer Model Defects. *Soft Matter* **2014**, *10*, 3284–3291.

CHAPTER 3

MORPHOLOGY EVOLUTIONS OF BOTTLEBRUSH BLOCK COPOLYMERS: INFLUENCE OF SIDE CHAIN AND VOLUME FRACTIONS

3.1 Introduction

3.1.1 Chain Entanglement of Linear Block Copolymer

Block Copolymers (BCPs) have attracted tremendous attention due to their roles as scaffolds in directing self-assembly from a few to tens of nanometers through microphase separation.[1–15] For a traditional linear A-B BCP, the morphology is governed by control over the Flory-Huggins parameter (χ), the number of repeat units (N) and the block volume fraction (f).[1–3] The degrees of chain entanglement or the viscosities of linear BCPs become quite serious when the molecular weight increases. The resulting increase in defects, longer processing time and lack of long-range ordering limit the further application of BCPs in next-generation hybrid materials.

3.1.2 Architecture and Application of Bottlebrush Block Copolymers

Bottlebrush block copolymers (BBCP) are novel architected macromolecules with densely grafted branches attached to a linear backbone.[16,17] Significant repulsive forces between the short densely grafted side chains induce the stretching in the backbone of BBCP, and the BBCPs exhibit a reduced degree of chain entanglement compared to linear BCPs.[18,19] Such intrinsic properties enable BBCP to exhibit fast ordering dynamics with large domain spacings (d-spacings) over 100 nm, offering opportunities for rapid and scalable manufacturing for various applications.[20–30]

3.1.3 Current Morphology Study Progress of Bottlebrush Block Copolymers

Knowledge of BBCP phase behavior is essential for the control of their morphology and subsequent applications. Multiple parameters including the chemical incompatibility of two blocks, the block volume ratio, the side chain asymmetry, and the length of backbone should be considered when investigating their morphology transitions. Theodorakis[31] and coworkers reported a simulation result for the self-assembly of BBCPs in which the transition from lamellae to hexagonally packed cylinders did not quite depend on asymmetry of volume fraction, but rather from the asymmetry of the side chain. This result significantly deviated from the current understanding of linear BCP phase behavior.

Recent experimental studies has offered a glimpse into the phase behavior of BBCPs, but not yet provided a satisfactory description of the parameters that precisely control the morphology upon microphase segregation.[32–35] To date there has been incomplete control over molecular characteristics of synthesized BBCP and studies have been limited to purely symmetric system. The most developed "graft from" or "graft onto" methods for BBCP synthesis introduced subsequent growth of side chains from a linear backbone, requiring orthogonal mechanisms or the purification of unreacted side chain in grafting process.[36–42] For example, Rzayev group[20,32,35] reported the self-assembly of asymmetric polystyrene-*b*-polylactide (PS-*b*-PLA) or polystyrene-*b*-poly (methyl methacrylate) (PS-*b*-PMMA) BBCPs using "RAFT-ATRP" method, in which they observed the formation of cylindrical structures with 55 nm in average pore size. However, the limited initiation efficiency of macroinitiators could not guarantee complete grafting in most "graft-from" or "graft to" methods, making it difficult to

determine side chain characteristics and precisely explain the control over the BBCP phase transition.[19]

On the other hand, combinations of norbornene (NB) modified macromonomers (MM) and ring opening metathesis polymerization (ROMP) developed by Xia et al.[19,43] and other groups[44,45] presented a more attractive route to synthesize BBCP, ensuring complete grafting of every backbone repeat unit. Nevertheless, only lamellar structures of BBCP in symmetric system have been investigated in detail so far.[18,19,46] For instance, Gu et al.[18] and Dalsin et al.[46] separately studied phase segregation of symmetric PS-*b*-PLA or polystyrene-*b*- (atactic) polypropylene (PS-*b*-aPP) BBCPs with well-ordered lamellae over a wide range of domain sizes. While those works explored the relationship between backbone length and the resulting domain spacing, there were no complete studies of the role of block volume fraction or side chain length on the phase behavior of asymmetric BBCPs, especially the BBCPs synthesized via MM methods.

3.1.4 Project Overview

Here the morphology transitions of polystyrene-*b*-poly (ethylene oxide) (PS-*b*-PEO) BBCP as a function of PEO side chain length and block volume fraction was studied (Figure 3.1). We specifically studied the asymmetric architectures, crystallization effects on microphase segregation, and microphase transition temperature (T_{MST}). Understanding of the role that side chain length and block volume fraction play in controlling the phase behavior of BBCP offers new opportunities for creating functional materials using BBCP as the scaffolds.

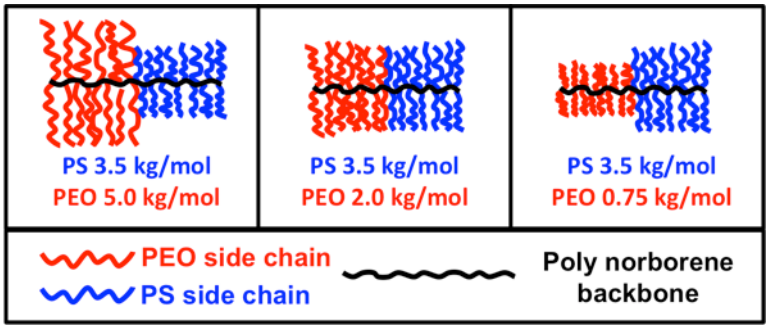

Figure 3.1 Illustration of PS-*b*-PEO BBCP with designated side chain lengths: PEO-NB (M_n ~ 0.75, 2.0 and 5.0 kg/mol accordingly) and PS-NB (M_n ~ 3.5 kg/mol). The PEO volume fraction (f_{PEO}) was controlled approximately from 20 % to 80 %.

3.2 Experimental

3.2.1 Materials

Cis-5-norbornene-exo-2,3-dicarboxylic anhydride (95%), ethanolamine (99.0%, ACS grade), triethylamine (> 99.5 %), N,N'-dicyclohexyl-carbodiimide (DCC, > 99.0 %), , 4-dimethylaminopyridine (DMAP, > 99%), sodium azide (NaN_3> 99.5%) styrene (contained 4-tert-butylcatechol as stabilizer, ≥ 99%), CuBr (98%), ethyl-2-bromoisobutyrate (98%),N,N,N′,N″,N″-Pentamethyldiethylenetriamine (PMDETA, 99%), poly (ethylene glycol) methyl ether (M_n ~ 0.75, 2.0 and 5.0 kg/mol), exo-5-norbornenecarboxylic acid (97 %), gallic acid (GA) were purchased from Sigma-Aldrich. Pentynoicacid (98 %), anhydrous dichloromethane (DCM), anhydrous toluene (99.8 %), anhydrous N,N-dimethylformamide (DMF, 99.8%), anhydrous tetrahydrofuran (THF, 99.9 %) were purchased from Acros Organics. Third-generation Grubbs catalyst was prepared based on the reported method.[19,43] Styrene was passed through basic aluminum oxide before the polymerization. Under nitrogen flow, PEO methyl ether was heated at 120 °C for about 4 hours to remove moisture before usage. Ruthenium tetroxide (0.5%

stabilized aqueous solution) was purchased from VWR. Thiol-terminated polystyrene (M_n ~ 2.5 kg/mol, PDI~1.05) was purchased from Polymer Source, Inc.

3.2.2 Preparation of Macromonomers and Third-Generation Grubbs Catalyst

The synthesis and characterization of PS-NB (M_n ~ 3.5 kg/mol) and PEO-NB (*Mn* ~ 0.75, 2.0 and 5.0 kg/mol) followed the established procedures.[19,43,47–50] PS-NB was prepared using atom transfer radical polymerization (ATRP) and click chemistry. A high yield strategy was proposed to synthesize PEO-NB MM by modifying the end group of commercial available PEO. Under nitrogen flow, PEO methyl ether (CH_3-PEO-OH) was heated at 120 ^oC for about 4 hours to remove moisture. After cooling, 2 mmol PEO-OH (*Mn* ~ 0.75 kg/mol (1.5 g), *Mn* ~2.0 kg/mol (4.0 g) or 5.0 kg/mol (10.0 g)), exo-5-norbornenecarboxylic acid (0.55 g, 4 mmol), DCC (0.99 g, 4.8 mmol) and DMAP (24 mg, 0.2 mmol) were added into a 200 mL of Schlenk flask followed by 30 mL anhydrous DCM. The reaction mixture was stirred at room temperature for about 48 hours, filtered to remove precipitates, and the filtrate was precipitated in cool diethyl ether three times to yield white solid as PEO-NB. Table 3.1 summarized the characteristics of as prepared MMs.

The third generation Grubbs catalyst was prepared based on the established routine. [19,43] Typically, 100 mg second generation Grubbs catalyst was mixed with 0.5 mL 3-bromopyridine. The mixture color immediately changes from dark brown to bright green, indicating the new ligand coordination. The product was precipitated and washed with 10 mL pentane for three times. The green solid was then dried under vacuum and transferred to nitrogen glove box.

Table 3.1 Characteristics of PS-NB and PEO-NB macromonomer (MM)

MM[a]	M_n (kg/mol)[b]	PDI[b]	DP^c_{NMR}	DP^d_{GPC}	$DP^e_{supplier}$
PS-3500-NB	4.0	1.06	33	35	-
PEO-750-NB	1.3	1.04	25	27	17
PEO-2000-NB	3.2	1.03	53	70	45
PEO-5000-NB	8.1	1.03	128	181	114

[a] The MMs are named as "X-M_n-NB", where X refers to MM chemical composition. [b] Measured by GPC. [c] Calculated using the integrations of PS phenyl group, PEO backbone and protons on the C=C bonds of NB end groups from ^{1}H-NMR spectra. [d] Calculated from GPC traces, higher DP was obtained due to PS standards used for calibration. Contribution of end group to MW was subtracted from the results (354 g/mol for PS-NB and 120 g/mol for PEO-NB respectively). [e] Calculated from molecular weight provided by Sigma-Aldrich.

3.2.3 Preparation of Bottlebrush Block Copolymers

In a typical experiment, 40-200 mg of PS-NB and PEO-NB MM were added to separate Schlenk flasks followed by the desired amount of anhydrous DCM. The concentration of the PS-NB MM was controlled from 0.05 to 0.1 M. The resulting solutions were degassed with three cycles of freeze-pump-thaw before the sequential polymerization. At room temperature, the polymerization of PS-NB was initiated by adding the desired amount of third generation Grubbs catalyst solution in DCM. After the first MM PS-NB reacted for 20 minutes, solution of the second MM, PEO-NB, was injected into the reaction mixture. This solution was stirred for an additional 2-3 hours. The reaction was quenched with ethyl vinyl ether. By tuning the mass ratio of reacting PS-NB and PEO-NB MM, the volume fraction of PS and PEO block was controlled. The mass ratio of PS and PEO block was calculated according to the corresponding molar ratio as determined using ^{1}H-NMR spectra.

3.2.4 Characterization

Proton or carbon nuclear magnetic resonance (^{1}H-NMR/^{13}C-NMR) spectroscopy was recorded in $CDCl_3$ using a Brucker 300 or 500 NMR Spectrometer. Gel permeation chromatography (GPC) of the BBCPs was carried out in THF on two PLgel 10 µm mixed-B LS columns (Polymer Laboratories) connected in series with a DAWN EOS multi angle laser light scattering (MALLS) detector and an RI detector. A calibration standard of PS with *Mn* ~ 30 kg/mol were used for the BBCP, and *dn/dc* values were obtained for each injection by assuming 100% mass elution from the columns. GPC analysis of PS-NB and PEO-NB MM were carried out using a Polymer Labotatories PL-GPC50 instrument with two 5 µm mixed-D columns, a 5 µm guard column, and a RI detector (HP1047A). THF was used as the eluent at a flow rate of 1.0 mL /min. Polystyrene standards were used for the calibration. Fourier Transform Infrared (FT-IR) (Perkin Elmer 2000) spectra of BBCP were taken in the range from 4000 to 650 cm^{-1} on ATR mode. Differential scanning calorimetry (DSC) analysis was performed on TA instrument Q200-1390-RCS. The melting enthalpy of PEO domain was measured on the second heating scan from - 60 to 110 °C at a rate of 5 °C/min. The heat of fusion for 100 % crystalline PEO was ΔHm^{0} ~197 J/g as referred in the TA instrument thermal application note. Morphology and domain spacing of BBCP were characterized using small/wide angle X-ray scattering (SAXS/WAXS). Bulk films were placed in the center of a metal washer and sealed with Kapton tape. These samples were measured on Ganesha SAXS-LAB with Cu Kα 0.154 nm line on SAXS/WAXS or ESAXS mode with a temperature control stage. Cryo-microtoming (Leica Ultracut microtome) was used to cut the nanocomposite bulk film into 50 nm thin films. Sections were collected using a

carbon film supported by copper grids. Subsequent RuO_4 staining was applied to improve contrast between PS and PEO domains. The prepared thin films were then characterized by transmission electron microscopy (TEM) on JEOL 2000FX 200kV.

3.3 Results and Discussions

3.3.1 Synthesis Control of Bottlebrush Block Copolymers

Table 3.2 Characteristics of the PS-*b*-PEO BBCP 5k-Y, 2k-Y and 0.75k-Y series

BBCP[a]	[Cat]:[PS_{MM}]:[PEO_{MM}]	f_{PEO} (%)[b]	M_w (kg/mol)[c]	PDI[c]	DP PS[d]	DP PEO[d]	d-spacing (nm)[e]
5k-24	1:100:18	24	714.7	1.28	121	27	43.6
5k-28	1:51:12	28	320.2	1.10	60	16	41.9
5k-32	1:47:14	32	345.9	1.12	60	20	51.1
5k-37	1:101:30	37	727.9	1.26	105	41	46.9
5k-49	1:36:25	49	473.6	1.09	63	42	59.5
5k-57	1:72:50	57	808.0	1.23	81	75	76.2
5k-72	1:20:33	72	416.5	1.13	29	53	35.0
5k-81	1:15:43	81	401.9	1.16	19	56	34.0
2k-22	1:47:21	22	346.0	1.09	70	34	43.3
2k-41	1:25:31	41	214.6	1.16	30	43	55.6
2k-45	1:38:46	45	393.3	1.38	49	60	82.7
2k-71	1:14:58	71	299.3	1.16	21	92	41.9
2k-79	1:9:61	79	282.9	1.25	14	89	34.4
0.75k-20	1:111:130	20	693.2	T	133	155	52.4
0.75k-28	1:79:159	28	710.1	D	121	220	61.0
0.75k-41	1:44:206	41	394.1	D	54	176	50.3

[a] BBCPs are labeled as "X-Y", where X and Y represent PEO side chain length and PEO domain volume fraction respectively. [b] Volume fraction of PEO (f_{PEO}) was calculated from characteristic protons in ^{1}H-NMR spectrum. [c] *Mw* and PDI were determined by GPC MALLS traces, D referred to two and T represented three components in one sample. [d] An approximate estimation of degree of polymerization using absolute molecular weights were measured by GPC-MALLS. [e] Domain spacing (d-spacing) of BBCP was calculated using the equation $d=2\pi/q^*$, where q^* corresponded to the primary peak in SAXS.

We synthesized a family of PS-*b*-PEO BBCPs with volume fraction of PEO block (f_{PEO}) varying from 22 % to 81 %, and with different PEO side chain lengths (M_n ~ 2.0 and 5.0 kg/mol) following reported procedures.[19,43,47] Table 3.2 summarizes the molecular characteristics of the synthesized 2k-Y and 5k-Y series of PS-*b*-PEO BBCP.

The chemical compositions of the obtained BBCPs were determined using ^{1}H-/^{13}C-NMR data (Figure 3.2) and FT-IR spectra (Figure 3.3). Figure 3.2 shows a representative ^{1}H-NMR spectrum of PS-*b*-PEO BBCP, where the signals of 6.5-7.2 ppm are ascribed to PS phenyl groups and 3.6-3.8 ppm for protons of PEO side chains. The mass ratio of PS and PEO blocks was calculated according to the corresponding molar ratio as determined using ^{1}H-NMR spectra. Subsequently, the volume ratio of PS and PEO (V_{PS}/V_{PEO}) was obtained using their approximate bulk densities (1.05 and 1.08 g/cm^3 for PS and PEO, respectively). The PEO domain volume fraction was calculated as $f_{PEO}=V_{PEO}/(V_{PEO}+V_{PS})$.

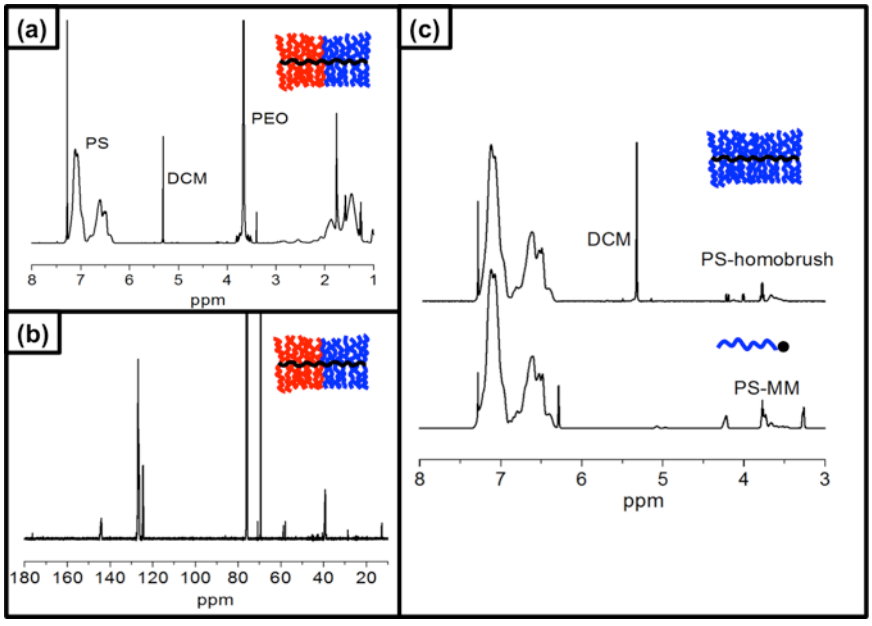

Figure 3.2 Representative (a)^{1}H-NMR, (b)^{13}C-NMR spectrum of synthesized PS-*b*-PEO BBCPs and (c) ^{1}H-NMR spectra of PS homo brush polymer after 20 minutes reaction and PS MM.

The nearly quantitative conversion of both PS-NB and PEO-NB MM can be confirmed from ^{1}H-NMR spectra Figure 3.2 (a), where the signals (6.15-6.28 ppm) of protons on the C=C bonds of NB end groups were absent for all the BBCP. At the same time, signals at 5.04-5.38 ppm from protons of opened C=C bonds indicated successful polymerization of norbornene backbone. In addition, nearly all PS-NB MMs were converted into brush polymer after 20 minutes of reaction. This was accomplished by acquiring the ^{1}H-NMR spectrum of first block Figure 3.2 (c) polymerized via ROMP using PS-NB of similar molecular weight (2.9 kg/mol). The second MM, PEO-NB was added after 20 minutes reaction of the first MM (PS-NB), and initiated the polymerization of the second MM, affording PS-*b*-PEO BBCP for the study.

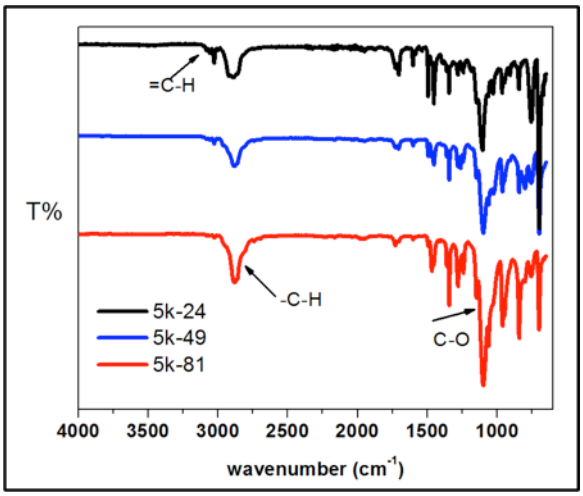

Figure 3.3 FT-IR spectrums of representative 5k-Y series.

The molecular weights of BBCPs were obtained using GPC MALLS. The light scattering (LS) traces of the BBCPs are provided in Figure 3.4. While all 2k-Y and 5k-Y samples exhibited a monomodal peak, weak shoulders and tailing were observed in GPC traces of a few samples, such as 5k-28, 5k-32 in Figure 3.4 (a), 2k-22 in Figure 3.4 (b). These features were observed previously for other brush polymers with high molecular

weights.[35,37,39,51] The shoulders observed in GPC traces of 5k-28 and 5k-32 at the shorter elution times could be due to higher molecular weight species. The tailing observed for 5k-81, 5k-49 and 5k-32 were mainly due to low molecular weight species.[19,35,43] The low population of these "impurities" is not expected exert a significant influence on the phase behavior of the BBCP.[35,51–53]

A series of PS-*b*-PEO BBCPs with extremely short PEO chains (0.75 kg/mol) were prepared. However, the synthesis of the BBCPs containing PEO of 0.75 kg/mol was poorly controlled, possibly due to the rapid polymerization kinetics of small PEO-NB MMs with short side chain lengths. The GPC traces (Figure 3.4 (c)) of the resulting samples show multiple peaks, indicating that multiple species in fact exist in those samples. Therefore, the discussion of the morphology of these BBCPs was not included. Despite the exclusion of 0.75k-Y system, the preparation of 5k-Y and 2k-Y PS-*b*-PEO BBCPs was generally under control, and the samples were suitable for subsequent morphology studies.

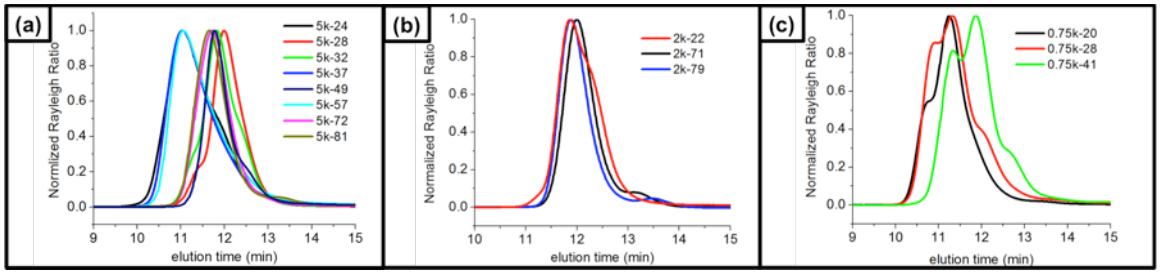

Figure 3.4 GPC traces of PS-*b*-EPO BBCPs (a) 5k-Y, (b) 2k-Y and (c) 0.75k-Y series.

3.3.2 Morphology Evolution As Function of Side Chain and Volume Fraction Asymmetry

The morphologies of PS-*b*-PEO BBCPs in the bulk state were measured with SAXS (Figure 3.5) as well as complementary TEM analysis (Figure 3.6) of cryo-microtomed samples. The domain spacing (d-spacing) was calculated using $d=2\pi/q^*$ for

each primary scattering peak and listed in Table 3.1. All samples showed sharp primary scattering signals suggesting strong phase segregation between the PS and PEO domains.

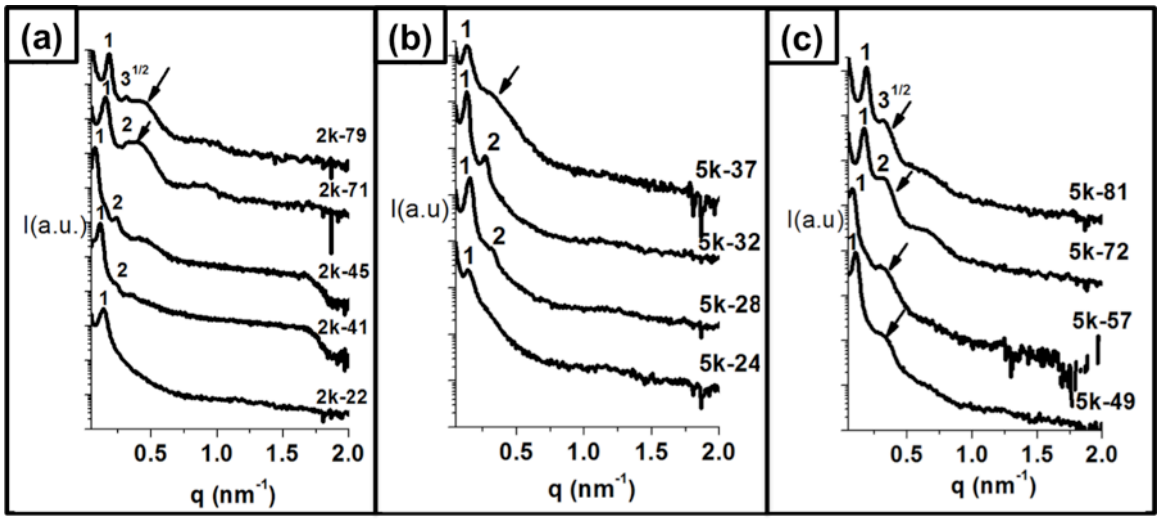

Figure 3.5 SAXS spectra (at room temperature) of PS-*b*-PEO BBCPs with PEO side lengths (a) PEO M_n ~ 2.0 kg/mol, f_{PEO} from 22 % to 79 %; (b) and (c) PEO M_n ~ 5.0 kg/mol, f_{PEO} from 24 % to 81 %. The broad curve with an arrow is attributed to X-ray scattering from PEO crystalline lamellae.

A disordered morphology (f_{PEO} < 22 %) was observed (Figure 3.6 (a)), in which short and irregular shaped PEO domains were dispersed within the PS matrix. In this sample, the BBCP exhibited strong phase segregation but did not form a well-defined periodical structure such as lamellae or hexagonal packed cylinders. The SAXS spectra (Figure 3.5 (a)) only show strong primary peak without high order reflections. Annealing for longer times or at higher temperature did not improve the regularity of packing. The formation of such strongly segregated but disordered morphology may result from a highly asymmetric volume fraction coupled with irregular interface curvature.

As f_{PEO} increased, we noticed that the morphology transition more depended on the variation of f_{PEO} rather than PEO side chain length (Figure 3.5). PS-*b*-PEO BBCP appeared to arrange into well-ordered lamellae at approximate equal volume fraction

(f_{PEO}~0.5) similar to other symmetric PS-*b*-PLA brush polymer systems.[18] Asymmetric lamellar structures were observed with f_{PEO} as low as 28 % or as high as 71 % in 5k-Y series. SAXS spectra of samples 2k-71, 5k-28, 5k-32 and 5k-72 reveal the ratios of $q^*:q_2$ = 1:2 and are consistent with TEM analysis (Figure 3.6 (b) to Figure 3.6 (e)).

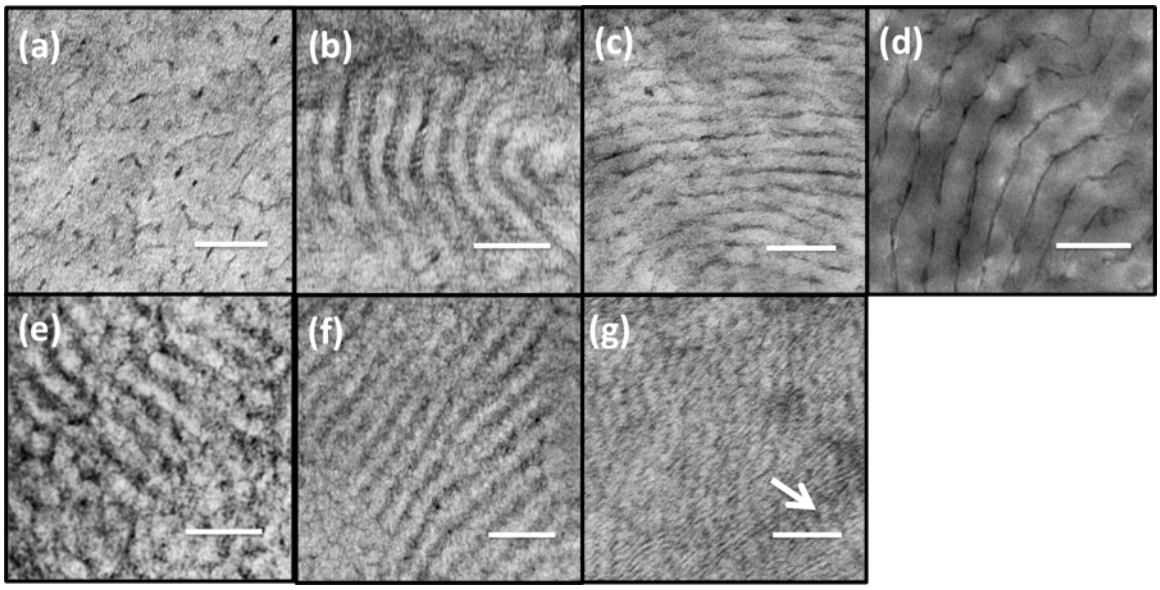

Figure 3.6 TEM images of cryo-microtomed PS-*b*-PEO BBCPs: (a) a disordered morphology in 2k-22; (b, c, d, e) asymmetric lamellae in (b) 2k-71, (c) 5k-28, (d) 5k-32 and (e) 5k-72; highly asymmetric BBCPs (f) 5k- 81 and (g) 2k-79. Ruthenium tetroxide (RuO_4) was used as the staining agent to improve the contrast between PS (bright area) and PEO (dark area) domains, all scale bars correspond to 100 nm. The arrow in (g) points to a region where PEO crystalline lamellae can be identified in the PEO-rich BBCP.

TEM images of highly asymmetric PS-*b*-PEO BBCPs, for example, 5k-81 (Figure 3.6 (f) shows some evidence of parallel cylindrical or lamellar morphology patterns, while 2k-79 (Figure 3.6 (g)) does not reveal clear morphology information due to the high crystallinity of PEO block and the low staining contrast between PS and PEO domains. Although TEM images have limitations for determining sample morphology, SAXS profiles with a characteristic high order reflection ratio of $q^*:q_2 = 1:\sqrt{3}$ (Figure 3.5 (a), (c)) indicate that in fact 5k-81 and 2k-79 exhibit cylindrical morphology at bulk state.

Temperature controlled SAXS profiles (Figure 3.7(a), (b)) provide a more convincing result, which will be discussed later.

TEM images of PS-*b*-PEO BBCPs have relatively low contrast, especially with high f_{PEO} samples, mainly due to weak selectivity of RuO_4 staining of PS-*b*-PEO BBCP and PEO crystallization. The right bottom of Figure 4g shows the PEO crystalline lamellae with a feature size approximately 14-20 nm (labeled by a small arrow), which is consistent with appearance of broad peak at high q in SAXS spectra (Figure 3.5 (a)).

3.3.3 Crystallization Effects of PEO Blocks

The crystallization of PEO became more apparent as f_{PEO} increased and therefore its effect on microphase segregation must be taken into consideration. A broad peak with feature size around 14-20 nm appeared in 2k-71, 2k-79 and 5k-49, 5k-57, 5k-72 and 5k-81 SAXS spectra, corresponding to the thickness of PEO crystalline lamellae. To obtain a better understanding of the effect that crystallization has on the morphology transition, we compared both SAXS and WAXS spectra of four samples with high f_{PEO} (70 %-80 %) acquired at room temperature and above the PEO melting point (Figure 3.7).

In Figure a, at 25 °C the sample showed both sharp crystalline peaks in WAXS regime and broad peak beside the secondary high order reflection (q*:q= 1:√3) in the SAXS regime. A series of higher order reflections (1: √3: √4: √7) consistent with a cylindrical morphology appeared as temperature increased to 65 °C, accompanied by the disappearance of PEO crystalline scattering signals in WAXS regime. The crystalline lamellae of PEO completely melt at this temperature and a well-ordered cylindrical structure was observed. Figure 3.7 (b), (c) and (d) show similar behaviors, confirming the

cylindrical (5k-81) and lamellar (2k-71 and 5k-72) morphologies of the BBCPs above the PEO melting point.

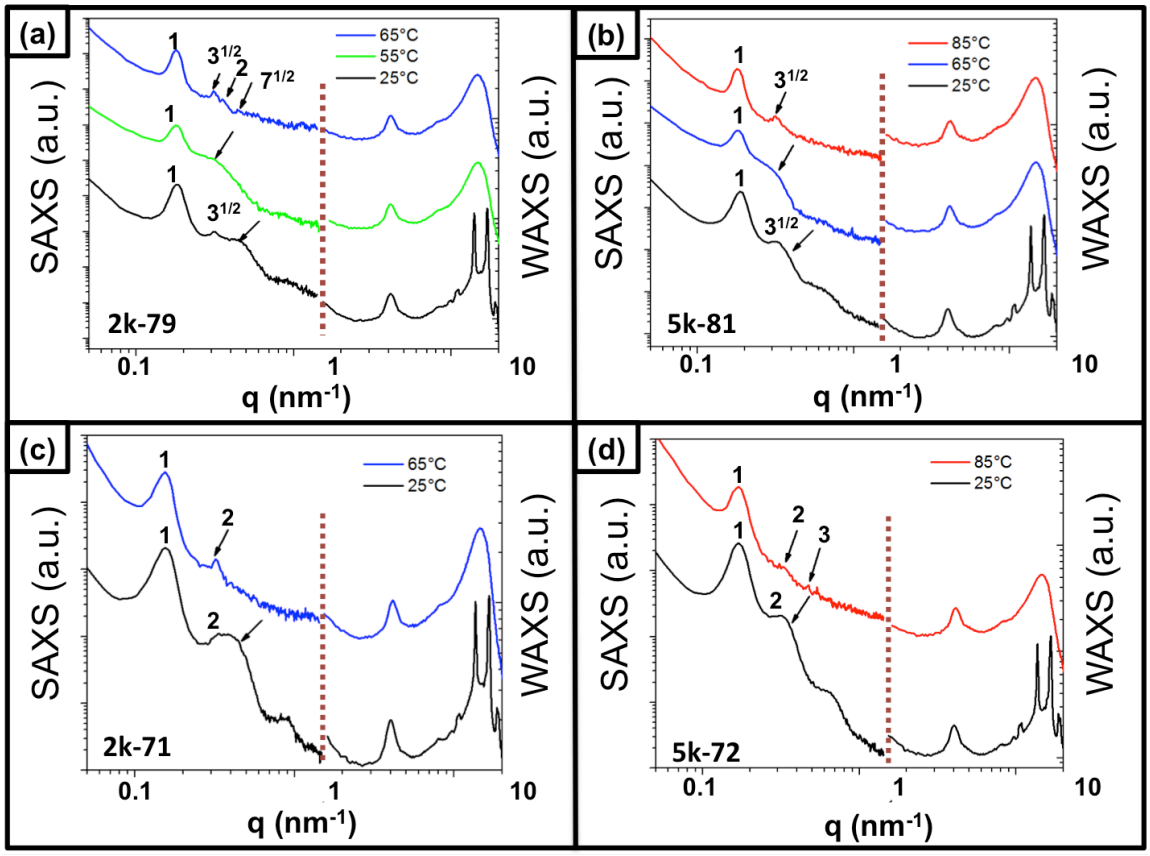

Figure 3.7 Temperature controlled SAXS and WAXS 1-D profiles of BBCPs containing high volume fractions of PEO: (a) 2k-79, (b) 5k-81, (c) 2k-71, and (d) 5k-72. Higher order reflections peaks can be observed at temperature that result in a melt state of the PEO domain.

Before and after heating, the SAXS/WAXS profiles of BBCPs remained same at 25 °C. SAXS and WAXS spectra of PS-*b*-PEO BBCPs with low f_{PEO} do not show significant PEO crystallization effects on the morphology transitions. The microphase segregation of 2k-22, 5k-28 remained approximately the same when heated within the same temperature range. DSC (Figure 3.8) analysis reveals decrease in degree of crystallization of lower f_{PEO} samples. For 2k-22, the PS-*b*-PEO BBCPs had degrees of crystallization of around 50 %, compared to 60 % - 66 % crystalline degree for 2k-79 and

5k-81. The slightly lower degree of crystallinity may be attributed to combination of degree of PEO side chain polymerization and reduced mobility of PEO in the high T_g PS matrix, which limited PEO side branch arrangement into crystallite lamellae.

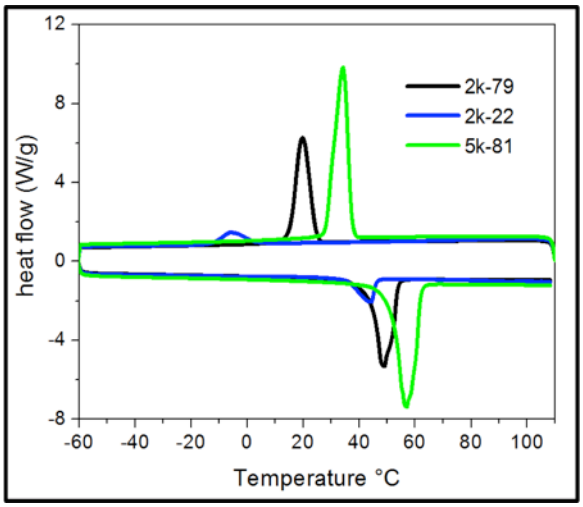

Figure 3.8 DSC measurement of representative PS-*b*-PEO BBCPs.

3.3.4 Microphase Transition Temperatures

A microphase transition temperature was observed when PS-*b*-PEO BBCPs were heated from 25 °C to 250 °C in a 30 °C step heating schedule with 3 minutes thermal equilibration at each temperature. The primary peaks in SAXS profiles of three typical PS-*b*-PEO samples (5k-28, 2k-79, 2k-22) were fitted to Gaussian curve and a series of full-width-at-half-maximum (FWHM) values were calculated. An abrupt change in slope determined the transition temperature in a plot of FWHM *versus* temperature (Figure 3.9).

When temperature was elevated, decreased intensities of the primary peaks and the disappearance of high order reflections was observed, indicating the decrease in degree of phase segregation.[4,5,54] Because the BBCP did not display long-range ordering,

we followed the reference and define this temperature as microphase transition temperature T_{MST}[55] rather than order-to-disorder transition temperature (T_{ODT}).

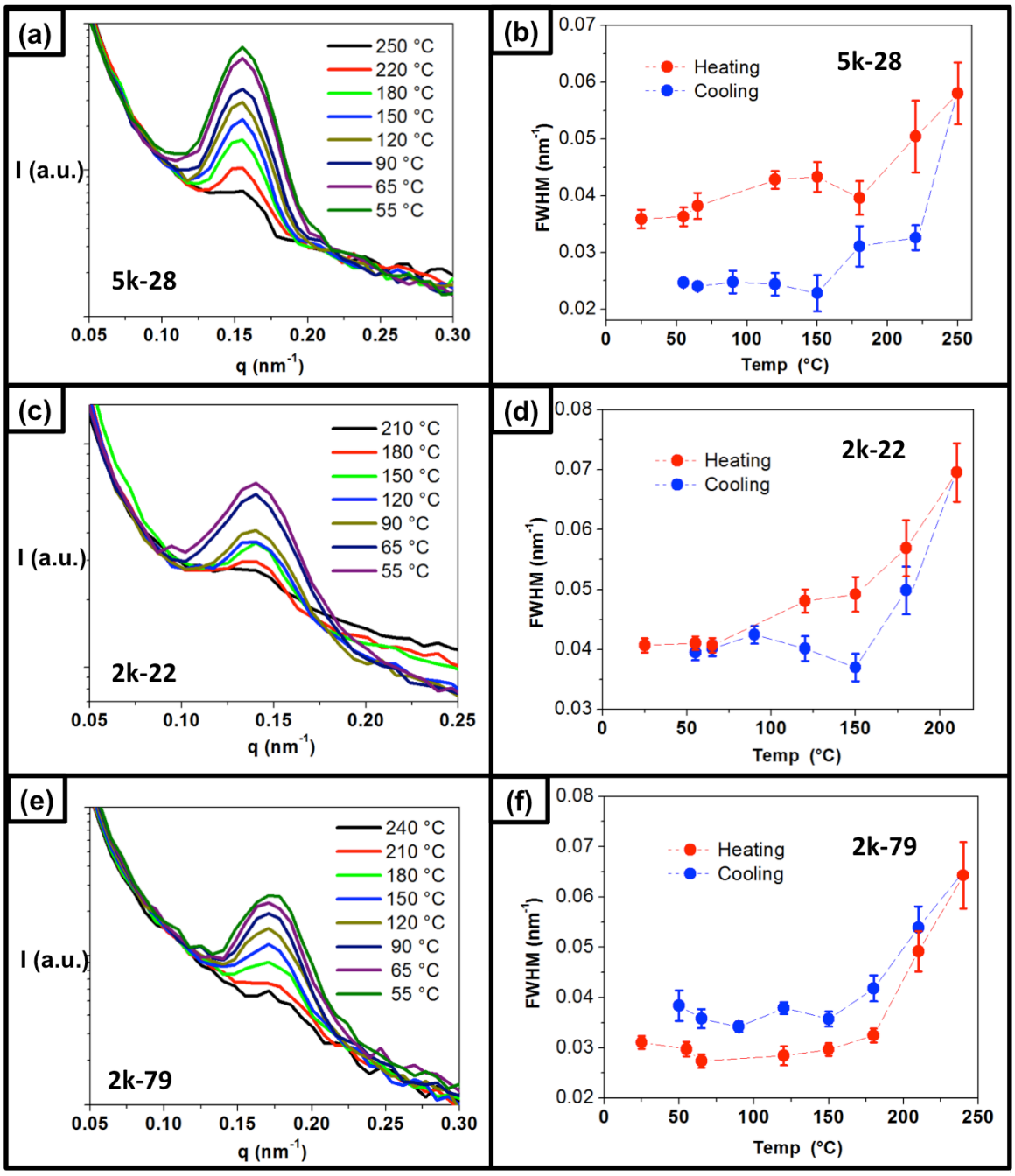

Figure 3.9 1-D SAXS profiles of BBCPs: (a) 5k-28, (c) 2k-79 and (e) 2k-22 show the influence of temperature on FWHM of the primary peak. (b, d, f) FWHM as a function of temperature of BBCPs: (b) 5k-28, (d) 2k-79 and (f) 2k-22 obtained by Gaussian Fitting of the primary peak.

The T_{MST} were found to be within the range of 150-180 °C for 5k-28, 2k-79, 2k-22 which had M_w from 280 kg/mol to 350 kg/mol. In light of these observations, the T_{MST} seemed to be relatively insensitive to volume fraction and side chain length within the molecular weight range investigated.

A few studies also investigated the effects of molecular characteristics of brush polymer on T_{ODT}. Although given the extensive variable space available in the design of brush polymers, these data sets are limited at this time. For example, Xia and coworkers[19] found that changes in T_{ODT} of polylactide-*b*-poly (n-butyl acrylate) (PLA-*b*-PnBA) bottlebrush random polymers (75-85 °C) was dominated by the degree polymerization N of side chain. Dalsin et al.[46] reported that only polystyrene-b-(atactic) polypropylene (PS-*b*-aPP) brush block copolymer (BBCP) of low molecular weight (M_n~28.3 kg/mol) had measurable T_{ODT} of approximately 215-220 °C, while most high molecular samples did not exhibit accessible T_{ODT} below the decomposition temperature of 300 °C. In this case, the overall molecular weight affected the final T_{ODT} of BBCPs. For a typical linear BCP, the product of the Flory-Huggins parameter χ and the degree of polymerization N determines the phase transition temperature. To fully understand the role of the complex molecular characteristics of BBCPs on T_{ODT} for any one system, a comprehensive family of BBCPs with measureable T_{ODT} as function of variable side chain lengths, backbone lengths and block volume fractions need to be synthesized and studied.

3.3.5 Asymmetric Template for Incorporating Dual Functional Nanoparticles

In order to achieve polymer based magneto-dielectric or metal-dielectric metamaterial, it is required to incorporate two types of functional NPs into two separate polymer domains.[56] However, few efforts have been dedicated to fabrication of a ternary

composite and control over its characteristics.[57–59] Bockstaller et al.[59] showed the preparation of ternary blends using polystyrene-*block*-polypropylene (PS-*b*-PEP) BCP and alkyl stabilized gold and silica NPs. Smaller gold NPs (d/L~0.06) were distributed at the interface between two domains while larger silica NPs (d/L~0.26) resided at the center of PEP domain, in which d was core diameter of particles and L was respective domain size. Despite the achievement of an ordered structure and controlled distribution of particles, the NPs loading was limited to less than 2% due to weak or neutral interaction between particles and polymer. Strong hydrogen bonding (H-bonding) NP/BCP interaction has been proven to increase particle size and loading.[47,60,61] Surprisingly, few efforts have been dedicated to the direct employment of H-bonding in ternary dual-NP/BCP composite.

Figure 3.10 reveals the integration of 5 wt % 6 nm Zirconium dioxide (ZrO_2)-GA NPs and 5 wt % 15 nm Au NPs (synthesize process followed the procedure[48,62] described in Chapter 2.2.1) into asymmetric PS-*b*-PEO BBCPs. ZrO_2-GA NPs were filled into the PEO domain through strong H-bonding interaction while Au NPs capped with PS had favorable affiliation to PS block. The ratio of core diameter (d_{core}) over domain width (L) d/L of ZrO_2-GA/PEO block and Au-PS/PS block were estimated to be 0.37 and 0.43 respectively, which was determined by PEO volume fraction of f_{PEO} ~ 32 % over a d-spacing of 51 nm. Although the SAXS spectra (Figure 1.10 (c)) did not show primary peak of this composite due to strong scattering from large gold metal cores, the well-ordered structure was confirmed with TEM images over large scale. It is worth noting that this metal-dielectric composite was formed without further annealing after solvent evaporation.

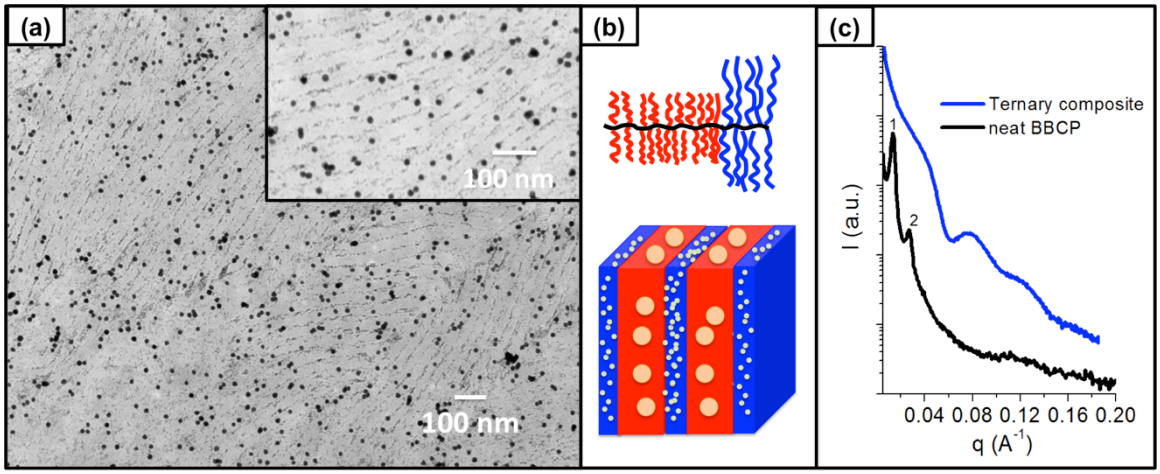

Figure 3.10 Ternary composite using PS-*b*-PEO BBCP as template, with 5 wt % 6 nm ZrO_2-GA and 5 wt % 15 nm Au-PS NPs:(a) TEM images of asymmetric lamellae, ZrO_2-GA resided in the narrower PEO domain while Au NPs had selective distribution in PS domain (b) schematic of asymmetric BBCP and ternary composite, (c) SAXS spectra of ternary composite.

3.3.6 Summary

A map of PS-*b*-PEO BBCP morphology trends was constructed using side chain asymmetry *versus* volume fraction (*f*) to provide a basic understanding of the morphology for these polymers. A linear BCP phase diagram is typically plotted as the phase segregation parameter χN *versus* volume fraction *f*. Considering the complex parameters in tuning the BBCP morphology, the side chain length ratio or asymmetry was applied for the Y-axis of a phase behavior plot (Figure 3.11) rather than χN. It is necessary to point out that there might be several physical parameters that could also be used to illustrate the phase behavior of a BBCP. For instance, Runge et al.[33] used mole fraction of one monomer in backbone as the Y-axis for their preliminary phase diagram.

Figure 3.11 shows the observed morphology transitions of PS-*b*-PEO BBCPs based on our experimental results. For the reported BBCPs, a lamellar structure formed over a much wider range of volume fraction when compared to linear BCP systems. The

prevalence of lamellae was weakly dependent on the side chain length. This phenomenon was expected due to the existence of a highly extended backbone and the fact that the volume fraction change did not significantly affect the cross-sectional area of BBCP.[20,31]

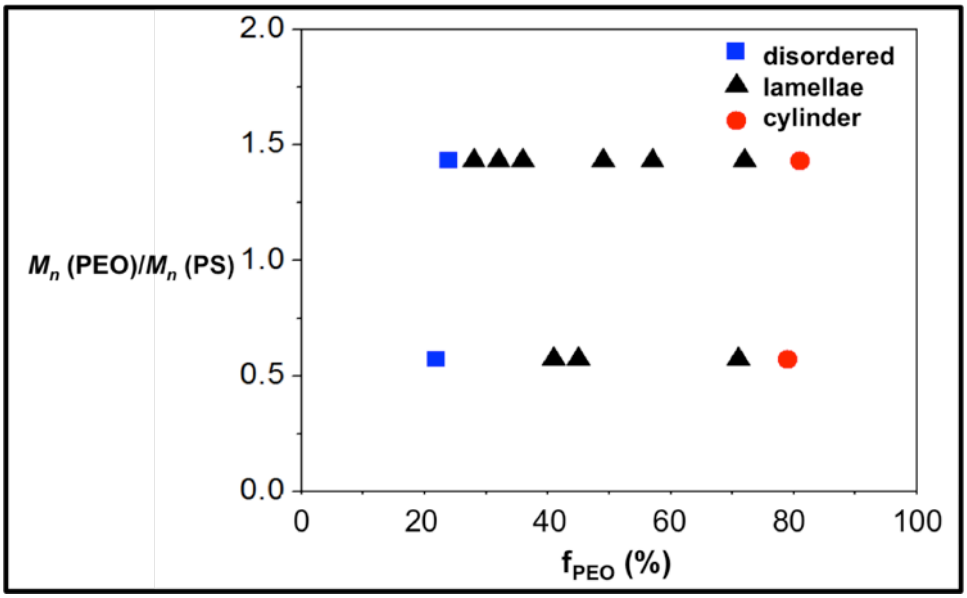

Figure 3.11 Summary of PS-*b*-PEO BBCP phase transition: a plot of side chain length ratio (M_n (PEO-NB)/M_n (PS-NB)) *vs* PEO volume fraction (f_{PEO}).

The samples with high f_{PEO} yielded cylindrical morphologies with PEO acting as the matrix domain. On the other end, we noticed that in samples with low f_{PEO} the PEO domain did not exhibit cylindrical morphology, instead, they formed a "disordered" structure. This unsymmetrical morphology evolution was different from a linear PS-*b*-PEO, in which hexagonally packed PEO cylinders have been observed with $f_{PEO} \sim 33$ %.[63] Although the hexagonal packing of PEO cylinders in PS matrix were not observed in the low f_{PEO} samples, such a morphology could still be expected by tuning the molecular weight of PEO-NB MM to much smaller than that of PS-NB MM.[64] For instance, previous studies[20] showed that PLA cylinders were observed in a PS-*b*-PLA BBCP, in

which the PLA side chains were much shorter than the PS. This asymmetry introduced a favorable curved interface, leading to the formation of well-defined PLA cylinders.

The chemical nature of side chain may also account for the interface curvature change and effect the subsequent morphology transition. Recently, the Osuji group[65] explored phase behavior of liquid crystalline brush like polymers, in which spheres, cylinders, lamellae, inverse cylinders and spheres were observed by merely increasing weight fraction of liquid crystal. The simple occurrence of curved interface for spherical or cylindrical morphology had strong dependence on volume fraction but regardless of side chain asymmetry was apparently apart from the current understanding of BBCP system.[31,64] Such interesting phenomenon may be due to the existence of liquid crystal group. More detailed investigations of side chain effects on BBCP morphology should be performed in the future.

The contents of Chapter 3 have been published in *Macromolecules,* **2017**, *50*, 1503-1511.

3.4 References

(1) Bates, F. S.; Fredrickson, G. H. Block Copolymers—Designer Soft Materials. *Phys. Today* **1999**, *52*, 32–38.

(2) Bates, F. S.; Fredrickson, G. H. Block Copolymer Thermodynamics: Theory and Experiment. *Annu. Rev. Phys. Chem.* **1990**, *41*, 525–557.

(3) Fredrickson, G. H.; Bates, F. S. Dynamics of Block Copolymers: Theory and Experiment. *Annu. Rev. Mater. Sci.* **1996**, *26*, 501–550.

(4) Khandpur, A. K.; Forster, S.; Bates, F. S.; Hamley, I. W.; Ryan, A. J.; Bras, W.; Almdal, K.; Mortensen, K. Polyisoprene-Polystyrene Diblock Copolymer Phase Diagram near the Order-Disorder Transition. *Macromolecules* **1995**, *28*, 8796–8806.

(5) Leibler, L. Theory of Microphase Separation in Block Copolymers. *Macromolecules* **1980**, *13*, 1602–1617.

(6) Bang, J.; Jeong, U.; Ryu, D. Y.; Russell, T. P.; Hawker, C. J. Block Copolymer Nanolithography: Translation of Molecular Level Control to Nanoscale Patterns. *Adv. Mater.* **2009**, *21*, 4769–4792.

(7) Cheng, J. Y.; Ross, C. A.; Smith, H. I.; Thomas, E. L. Templated Self-Assembly of Block Copolymers: Top-down Helps Bottom-Up. *Adv. Mater.* **2006**, *18*, 2505–2521.

(8) Cui, H.; Chen, Z.; Zhong, S.; Wooley, K. L.; Pochan, D. J. Block Copolymer Assembly via Kinetic Control. *Science.* **2007**, *317*, 647–650.

(9) Discher, D. E.; Eisenberg, A. Polymer Vesicles. *Science.* **2002**, *297*, 967–973.

(10) Ha, J. M.; Wolf, J. H.; Hillmyer, M. A.; Ward, M. D. Polymorph Selectivity under Nanoscopic Confinement. *J. Am. Chem. Soc.* **2004**, *126*, 3382–3383.

(11) Jackson, E. A.; Hillmyer, M. A. Nanoporous Membranes Derived from Block Copolymers: From Drug Delivery to Water Filtration. *ACS Nano* **2010**, *4*, 3548–3553.

(12) Klok, H. A.; Lecommandoux, S. Supramolecular Materials via Block Copolymer Self-Assembly. *Adv. Mater.* **2001**, *13*, 1217–1229.

(13) Ruzette, A.-V.; Leibler, L. Block Copolymers in Tomorrow's Plastics. *Nat. Mater.* **2005**, *4*, 19–31.

(14) Tang, C.; Lennon, E. M.; Fredrickson, G. H.; Kramer, E. J.; Hawker, C. J. Evolution of Block Copolymer Lithography to Highly Ordered Square Arrays. *Science.* **2008**, *322*, 429–432.

(15) Thurn-Albrecht, T.; Schotter, J.; Kästle, G. a; Emley, N.; Shibauchi, T.; Krusin-Elbaum, L.; Guarini, K.; Black, C. T.; Tuominen, M. T.; Russell, T. P. Ultrahigh-Density Nanowire Arrays Grown in Self-Assembled Diblock Copolymer Templates. *Science.* **2000**, *290*, 2126–2129.

(16) Sheiko, S. S.; Möller, M. Visualization of Macromolecules - A First Step to Manipulation and Controlled Response. *Chem. Rev.* **2001**, *101*, 4099–4123.

(17) Zhang, M.; Müller, A. H. E. Cylindrical Polymer Brushes. *J. Polym. Sci. Part A Polym. Chem.* **2005**, *43*, 3461–3481.

(18) Gu, W.; Huh, J.; Hong, S. W.; Sveinbjornsson, B. R.; Park, C.; Grubbs, R. H.; Russell, T. P. Self-Assembly of Symmetric Brush Diblock Copolymers. *ACS Nano* **2013**, *7*, 2551–2558.

(19) Xia, Y.; Olsen, B. D.; Kornfield, J. A.; Grubbs, R. H. Efficient Synthesis of Narrowly Dispersed Brush Copolymers and Study of Their Assemblies: The Importance of Side Chain Arrangement. *J. Am. Chem. Soc.* **2009**, *131*, 18525–18532.

(20) Bolton, J.; Bailey, T. S.; Rzayev, J. Large Pore Size Nanoporous Materials from the Self-Assembly of Asymmetric Bottlebrush Block Copolymers. *Nano Lett.* **2011**, 998–1001.

(21) Byun, M.; Bowden, N. B.; Lin, Z. Hierarchically Organized Structures Engineered from Controlled Evaporative Self-Assembly. *Nano Lett.* **2010**, *10*, 3111–3117.

(22) Cheng, C.; Qi, K.; Khoshdel, E.; Wooley, K. L. Tandem Synthesis of Core-Shell Brush Copolymers and Their Transformation to Peripherally Cross-Linked and Hollowed Nanostructures. *J. Am. Chem. Soc.* **2006**, *128*, 6808–6809.

(23) Huang, K.; Rzayev, J. Well-Defined Organic Nanotubes from Multicomponent Bottlebrush Copolymers. *J. Am. Chem. Soc.* **2009**, *131*, 6880–6885.

(24) Kang, Y.; Walish, J. J.; Gorishnyy, T.; Thomas, E. L. Broad-Wavelength-Range Chemically Tunable Block-Copolymer Photonic Gels. *Nat. Mater.* **2007**, *6*, 957–960.

(25) Miyake, G. M.; Weitekamp, R. A.; Piunova, V. A.; Grubbs, R. H. Synthesis of Isocyanate-Based Brush Block Copolymers and Their Rapid Self-Assembly of Brush Block Copolymers to Photonic Crystals. *J. Am. Chem. Soc.* **2012**, *134*, 14249–14254.

(26) Sveinbjornsson, B. R.; Weitekamp, R. A.; Miyake, G. M.; Xia, Y.; Atwater, H. A.; Grubbs, R. H. Rapid Self-Assembly of Brush Block Copolymers to Photonic Crystals. *Proc. Natl. Acad. Sci.* **2012**, *109*, 14332–14336.

(27) Djalali, R.; Li, S. Y.; Schmidt, M. Amphipolar Core-Shell Cylindrical Brushes as Templates for the Formation of Gold Clusters and Nanowires. *Macromolecules* **2002**, *35*, 4282–4288.

(28) Tang, C.; Dufour, B.; Kowalewski, T.; Matyjaszewski, K. Synthesis and Morphology of Molecular Brushes with Polyacrylonitrile Block Copolymer Side Chains and Their Conversion into Nanostructured Carbons. *Macromolecules* **2007**, *40*, 6199–6205.

(29) Zhang, M.; Estournès, C.; Bietsch, W.; Müller, A. H. E. Superparamagnetic Hybrid Nanocylinders. *Adv. Funct. Mater.* **2004**, *14*, 871–882.

(30) Zhang, M.; Drechsler, M.; Müller, A. H. E. Template-Controlled Synthesis of Wire-Like Cadmium Sulfide Nanoparticle Assemblies within Core-Shell Cylindrical Polymer Brushes. *Chem. Mater.* **2004**, *16*, 537–543.

(31) Chremos, A.; Theodorakis, P. E. Morphologies of Bottle-Brush Block Copolymers. *ACS Macro Lett.* **2014**, *3*, 1096–1100.

(32) Bolton, J.; Rzayev, J. Tandem RAFT-ATRP Synthesis of Polystyrene - Poly(methyl Methacrylate) Bottlebrush Block Copolymers and Their Self-Assembly into Cylindrical Nanostructures. *ACS Macro Lett.* **2012**, *1*, 15–18.

(33) Runge, M. B.; Bowden, N. B. Synthesis of High Molecular Weight Comb Block Copolymers and Their Assembly into Ordered Morphologies in the Solid State. *J. Am. Chem. Soc.* **2007**, *129*, 10551–10560.

(34) Runge, M. B.; Lipscomb, C. E.; Ditzler, L. R.; Mahanthappa, M. K.; Tivanski, A. V.; Bowden, N. B. Investigation of the Assembly of Comb Block Copolymers in the Solid State. *Macromolecules* **2008**, *41*, 7687–7694.

(35) Rzayev, J. Synthesis of Polystyrene-Polylactide Bottlebrush Block Copolymers and Their Melt Self-Assembly into Large Domain Nanostructures. *Macromolecules* **2009**, *42*, 2135–2141.

(36) Gao, H.; Matyjaszewski, K. Synthesis of Molecular Brushes By "grafting Onto" method: Combination of ATRP and Click Reactions. *J. Am. Chem. Soc.* **2007**, *129*, 6633–6639.

(37) Lanson, D.; Ariura, F.; Schappacher, M.; Borsali, R.; Deffieux, A. Comb Copolymers with Polystyrene and Polyisoprene Branches: Effect of Block Topology on Film Morphology. *Macromolecules* **2009**, *42*, 3942–3950.

(38) Lanson, D.; Schappacher, M.; Borsali, R.; Deffieux, A. Synthesis of (Poly (Chloroethyl Vinyl Ether)-G-Polystyrene) Comb-B-(Poly (Chloropyran Ethoxy Vinyl Ether)- G-Polyisoprene) Comb Copolymers and Study of Hyper-Branched Micelle Formation in Dilute Solutions. *Macromolecules* **2007**, *40*, 5559–5565.

(39) Lee, H. Il; Matyjaszewski, K.; Sherryl, Y. S.; Sheiko, S. S. Hetero-Grafted Block Brushes with PCL and PBA Side Chains. *Macromolecules* **2008**, *41*, 6073–6080.

(40) Runge, M. B.; Dutta, S.; Bowden, N. B. Synthesis of Comb Block Copolymers by ROMP, ATRP, and ROP and Their Assembly in the Solid State. *Macromolecules* **2006**, *39*, 498–508.

(41) Schappacher, M.; Deffieux, A. From Combs to Comb-G-Comp Centipedes. *Macromolecules* **2005**, *38*, 7209–7213.

(42) Sumerlin, B. S.; Neugebauer, D.; Matyjaszewski, K. Initiation Efficiency in the Synthesis of Molecular Brushes by Grafting from via Atom Transfer Radical Polymerization. *Macromolecules* **2005**, *38*, 702–708.

(43) Xia, Y.; Kornfield, J. A.; Grubbs, R. H. Efficient Syntheses of Brush Polymers via Living Ring Opening Metathesis Polymerization of Macromonomers. *Macromolecules* **2009**, *42*, 3761–3766.

(44) Cheng, C.; Khoshdel, E.; Wooley, K. L. ATRP from a Norbornenyl-Functionalized Initiator: Balancing of Complementary Reactivity for the Preparation of α-Norbornenyl Macromonomers/ω-Haloalkyl Macroinitiators. *Macromolecules* **2005**, *38*, 9455–9465.

(45) Patton, D. L.; Advincula, R. C. A Versatile Synthetic Route to Macromonomers via RAFT Polymerization. *Macromolecules* **2006**, *39*, 8674–8683.

(46) Dalsin, S. J.; Rions-Maehren, T. G.; Beam, M. D.; Bates, F. S.; Hillmyer, M. A.; Matsen, M. W. Bottlebrush Block Polmers: Quantitative Theory and Experiments. *ACS Nano* **2015**, *9*, 12233–12245.

(47) Song, D.-P.; Lin, Y.; Gai, Y.; Colella, N. S.; Li, C.; Liu, X.-H.; Gido, S.; Watkins, J. J. Controlled Supramolecular Self-Assembly of Large Nanoparticles in Amphiphilic Brush Block Copolymers. *J. Am. Chem. Soc.* **2015**, *137*, 3771–3774.

(48) Song, D.-P.; Li, C.; Li, W.; Watkins, J. J. Block Copolymer Nanocomposites with High Refractive Index Contrast for One-Step Photonics. *ACS Nano* **2016**, *10*, 1216–1223.

(49) Song, D. P.; Li, C.; Colella, N. S.; Xie, W.; Li, S.; Lu, X.; Gido, S.; Lee, J. H.; Watkins, J. J. Large-Volume Self-Organization of Polymer/Nanoparticle Hybrids with Millimeter-Scale Grain Sizes Using Brush Block Copolymers. *J. Am. Chem. Soc.* **2015**, *137*, 12510–12513.

(50) Song, D. P.; Li, C.; Colella, N. S.; Lu, X.; Lee, J.-H.; Watkins, J. J. Thermally Tunable Metallodielectric Photonic Crystals from the Self-Assembly of Brush Block Copolymers and Gold Nanoparticles. *Adv. Opt. Mater.* **2015**, *3*, 1169–1175.

(51) Kawamoto, K.; Zhong, M.; Gadelrab, K. R.; Cheng, L.-C.; Ross, C. A.; Alexander-Katz, A.; Johnson, J. A. Graft-through Synthesis and Assembly of Janus Bottlebrush Polymers from A- Branch -B Diblock Macromonomers. *J. Am. Chem. Soc.* **2016**, *138*, 11501–11504.

(52) Lynd, N. A.; Hillmyer, M. A. Influence of Polydispersity on the Self-Assembly of Diblock Copolymers. *Macromolecules* **2005**, *38*, 8803–8810.

(53) Lynd, N. A.; Hillmyer, M. A.; Matsen, M. W. Theory of Polydisperse Block Copolymer Melts: Beyond the Schulz-Zimm Distribution. *Macromolecules* **2008**, *41*, 4531–4533.

(54) Sakamoto, N.; Hashimoto, T. Order-Disorder Transition of Low Molecular Weight Polystyrene-Block-Polyisoprene. 1. SAXS Analysis of Two Characteristic Temperatures. *Macromolecules* **1995**, *28*, 6825–6834.

(55) Mannion, A. M.; Bates, F. S.; MacOsko, C. W. Synthesis and Rheology of Branched Multiblock Polymers Based on Polylactide. *Macromolecules* **2016**, *49*, 4587–4598.

(56) Mosallaei, H.; Sarabandi, K. Magneto-Dielectrics in Electromagnetics: Concept and Applications. *IEEE Trans. Antennas Propag.* **2004**, *52*, 1558–1567.

(57) Bockstaller, M. R.; Ryu, H. J.; Ojha, S.; Choi, J. 1D Periodic Bimetallic Superstructures by Co-Assembly of Ternary Block Copolymer/nanoparticle Blends. *J. Mater. Chem.* **2010**, *20*, 9339.

(58) Sohn, B. H.; Choi, J. M.; Yoo, S. Il; Yun, S. H.; Zin, W. C.; Jung, J. C.; Kanehara, M.; Hirata, T.; Teranishi, T. Directed Self-Assembly of Two Kinds of Nanoparticles Utilizing Monolayer Films of Diblock Copolymer Micelles. *J. Am. Chem. Soc.* **2003**, *125*, 6368–6369.

(59) Bockstaller, M. R.; Lapetnikov, Y.; Margel, S.; Thomas, E. L. Size-Selective Organization of Enthalpic Compatibilized Nanocrystals in Ternary Block Copolymer / Particle Mixtures. *J. Am. Chem. Soc.* **2003**, *125*, 5276–5277.

(60) Yao, L.; Lin, Y.; Watkins, J. J. Ultrahigh Loading of Nanoparticles into Ordered Block Copolymer Composites. *Macromolecules* **2014**, *47*, 1844–1849.

(61) Lin, Y.; Daga, V. K.; Anderson, E. R.; Gido, S. P.; Watkins, J. J. Nanoparticle-Driven Assembly of Block Copolymers: A Simple Route to Ordered Hybrid Materials. *J. Am. Chem. Soc.* **2011**, *133*, 6513–6516.

(62) Enustun, B. V.; Turkevich, J. Coagulation of Colloidal Gold. *J. Am. Chem. Soc.* **1963**, *85*, 3317–3328.

(63) Kim, D. H.; Sun, Z.; Russell, T. P.; Knoll, W.; Gutmann, J. S. Organic-Inorganic Nanohybridization by Block Copolymer Thin Films. *Adv. Funct. Mater.* **2005**, *15*, 1160–1164.

(64) Fenyves, R.; Schmutz, M.; Horner, I. J.; Bright, F. V; Rzayev, J. Aqueous Self-Assembly of Giant Bottlebrush Block Copolymer Surfactants as Shape-Tunable Building Blocks. *J. Am. Chem. Soc.* **2014**, *136*, 7762–7770.

(65) Choo, Y.; Mahajan, L. H.; Gopinadhan, M.; Ndaya, D.; Deshmukh, P.; Kasi, R. M.; Osuji, C. O. Phase Behavior of Polylactide-Based Liquid Crystalline Brushlike Block Copolymers. *Macromolecules* **2015**, *48*, 8315–8322.

CHAPTER 4

MAGENTO-OPTICAL PROPERITES OF IRON PLATIUM NANOPARTICLES AND BLOCK COPOLYMER COMPOSITE

4.1 Introduction

4.1.1 Magnetic Nanoparticles

As discussed in the introduction, magnetic materials comprised of cobalt or iron elements have been known for thousand of years. The recent development of magnetic material miniaturization provides possibilities for functional materials aimed in nanotechnologies.[1] For instance, magnetic nanoparticles (MNP) such as iron oxide (FeO_x), iron platinum (FePt), cobalt oxide (Co_3O_4), cobalt platinum (Co/Pt) nano-additives have been widely used in therapy drug delivery, biosensor or imaging, magnetic fluids, nano-engineering catalyst, environmental remediation and data storage.[1–3]

All these inspiring applications are realized by the unique physical properties of MNPs. Accompanying with decrease in the size of MNPs, the magnetization of MNPs returns to zero without the exposure to the applied field, which is known as paramagnetism. Large NPs of core diameter above 20 nm, in contrast, usually display ferromagnetism, in which the magnetizations persist without the field.[4] These interesting physical behaviors of MNPs are highly size dependent, and provide the opportunities for other optical or electronic utilization.[5,6]

4.1.2 Faraday Rotations and Verdet Constant

The optical property of a magneto-optical (MO) material can be simply tuned by the external magnetic field (MF).[7,8] The active MO response of materials enables

numerous high-end applications including optical isolators and switches, high performance MF sensors and electromagnetic signal amplifier.[9–17] Specially, Faraday rotation (FR) is one of the most important MO phenomena, in which the applied MF changes the polarization (Figure 4.1, copyright by DrBob~commonswiki on Wikipedia website) plane of propagating linearly polarized light by inducing a circular birefringence.[7,8] Assuming the materials exhibit negligible light absorption, the FR performance highly depends on the Verdet constant (V) of a unit °/T·m. The polarization rotation angle (θ) is proportional to V multiplied by the propagation length (L) under magnetic field (B) ($\theta=VBL$).

The Verdet constant (V) depends strongly on wavelength, temperature during the measurement of MO materials, and intrinsic material properties. The macroscopic response is determined by the interaction of the magnetic field with the net volumetric magnetic moment within the optical path, whereas the magnetic moment itself is determined by the inherent electronic structure and composition of the material.[7]

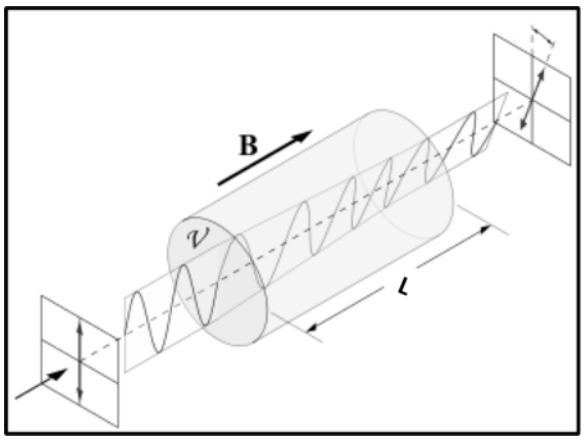

Figure 4.1 The illustration of Faraday rotation: the polarization plane of light will be altered to certain angle when exposed to an applied field (adapted from online reference 18 in Chapter 4).

4.1.3 Current Progress of Magneto-Optical Materials

Transparent materials with FR response at room temperature have been of great interest over the last few decades.[19–29] Acceptable MO performance in a composite generally requires the dispersion of a high volume fraction of magnetic species, which often leads to light losses through scattering of aggregated additives, thereby decreasing the transparency and effective FR response.[22] Today's benchmark MO materials include ferromagnetic terbium gallium garnet (TGG, $Tb_3Ga_5O_{12}$)[30–32] and bismuth (Bi) doped yttrium iron garnet (Bi:YIG, $Y_2Fe_5O_{12}$)[33–38], targeting the visible and near infrared (NIR) regimes, respectively. However, this family of materials containing rare-earth elements is usually produced as single crystals in order to achieve millimeter-scale path lengths for sufficient MO performance.[26] The high processing costs associated with high-quality crystal growth and limited achievable film thickness have restricted their broader utilization.

4.1.4 Magnetic Nanoparticles and Polymer Composite: Advantages and Challenges

Recently, composites using MNPs dispersed in organic matrices have offered an alternative low-cost method for generating MO materials.[21,22] To balance the trade-off between high NP loading and decreased transparency, the scattering loss generated by MNPs need be taken into consideration and alleviated. If the MNPs of core diameters (d) are much smaller than the wavelength of light but larger than 20 nm, Rayleigh scattering predominates the scattering loss. Significant scattering loss can arise when there are substantial (> 0.1) differences between the refractive indices of the polymer matrix and inorganic NP. In this case, it is a necessary to use small NPs (< 20 nm) that are evenly distributed in a pore-free polymer matrix.[39,40] The transmittance of the film follows

Beer's law, which is exponentially dependent on both NP medium concentration and propagation length of light. Taken together, delicate control over the dispersion and spatial distribution of MNPs in polymer matrix, homogeneity, and thickness of films are essential to guarantee adequate film FR performance.

Various systems including MNPs and silica sol-gel porous matrix blends[41–46], plasmonic enhanced shell MNPs[47–51], and homopolymer stabilized core-shell MNP composites[52–57] have been studied to understand both their scattering mechanisms and MO performance. Despite the high Verdet constants achieved in some of these composites, the resulting scattering from the aggregation of large NPs at higher concentrations still limits the FR application at realistic length scales. Thus, it is essential to find other strategies that give uniform MO composite materials with precise control over the particle distribution and balance light losses and concentration of MO species.

Self-assembly of functional NPs and block copolymer (BCP) offers a straightforward "bottom-up" avenue for producing MO composite materials.[58–62] BCPs can microphase segregate into periodic structures at the nanoscale, with facile control over the volume fraction and chemical nature of the two blocks. Strong NP/BCP interactions have been shown to selectively integrate functional NPs into specific domains with desired size, filling fractions, and building block directions.[63–70] Resulting hybrid materials, with improved electric and optical properties, have been utilized in organic field effect transistors and polymeric Bragg mirrors.[71–73]

As a critical MO component in hybrid materials, iron platinum (FePt) NPs are of great interest due to their excellent chemical stability and demonstrated applications in high-density magnetic storage, bio-sensing, and therapeutics.[5,6,74–76] Simultaneous

synthesis[4,77,78] and surface modification[79] of size controlled FePt particles with diameters less than 10 nm allowed the construction of paramagnetic materials displaying unique size dependent properties. A series of BCPs including polystyrene-*block*-poly (2-vinyl pyridine) (PS-*b*-P2VP), polystyrene-*block*-poly (ethylene oxide) (PS-*b*-PEO), and polystyrene-*block*-poly (acrylic acid) (PS-*b*-PAA) have used to assemble with MNPs by strong hydrogen-bonding (H-bonding) interaction, leading to the enhanced phase segregation and long-rang ordering (Figure 4.2).[80] Copolymer templates are expected to selectively template the NPs, resulting in the reduced light scattering and improvement of FR response by permitting the control of the NP filling fraction and distribution. To date few efforts have been directed toward the MO material fabrication using selective arrangement of MNPs into a BCP template.

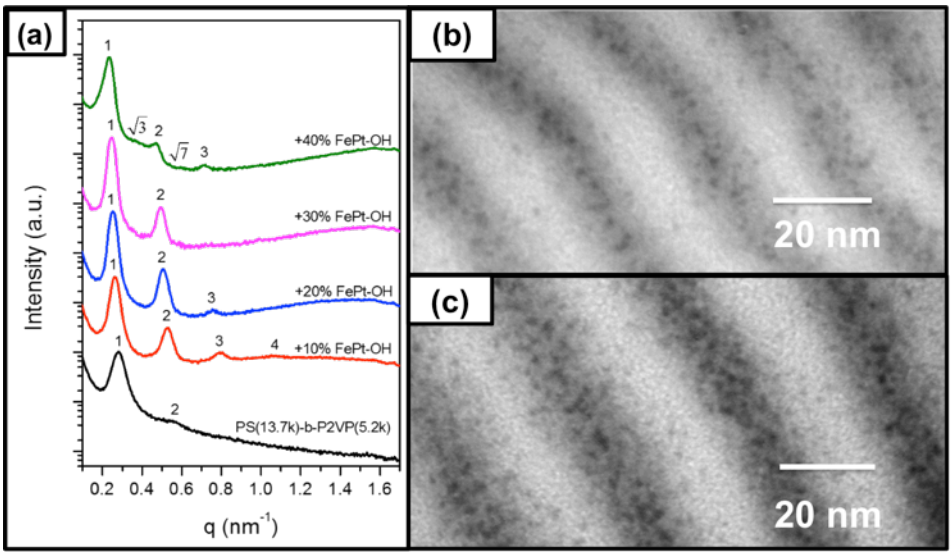

Figure 4.2 Well-ordered lamellae morphology using modified FePt NPs and PS (13.7k)-*b*-P2VP (5.2k) BCPs via H-bonding interaction. 40 wt % loading of FePt NPs introduced order-to-order transition (Courtesy to Dr. Xinyu Wang, adapted from reference 80 in Chapter 4).

4.1.5 Project Overview

In this work, a solution-processable method has been demonstrated to prepare MO materials of high Verdet constants at room temperature by integrating FePt NPs into a (PS-*b*-P2VP) template (Figure 4.3). NPs with core diameters (d_{core}) from 1.9 to 9.3 nm were synthesized and modified with gallic acid (GA) to enable H-bonding interactions with the P2VP domains. The selective distribution of particles in the P2VP domain at the nanoscale reduced light scattering and achieved large Verdet constants in conjunction with improved transparency compared to conventional composites. The roles of particle size, loading, and optical wavelength played in the FR response of BCP based polymeric composites have been systematically investigated. This work was conducted in collaboration with Norwood group at University of Arizona. Alexander Miles and Dr. Palash Gangopadhyay measured the FR responses of composites. The author acknowledges Professor Norwood and Dr. Palash Gangopadhyay for detailed discussion and interpretation of FR measurement results.

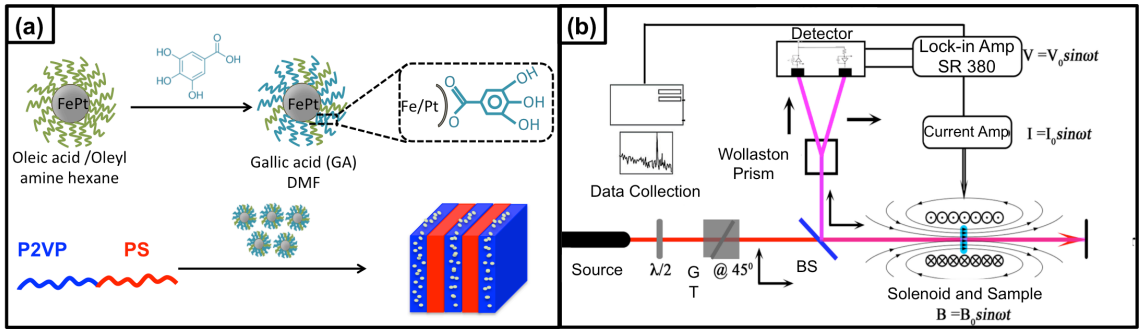

Figure 4.3 Project overview: (a) Surface modification of FePt NPs using gallic acid (GA) as a hydrogen bonding donor followed by selective NP dispersion in the P2VP domain within a symmetric PS-*b*-P2VP BCP template (b) setup of FR response measurement, courtesy to Norwood group.

On the other hand, introducing the MNPs on the substrate of periodical structures can also be achieved by using the imprinting method, which has been demonstrated by

our group[81] (Figure 1.4) with general applicability to a wide range of metal oxides NPs. In this project, another type of commercial available MNP was surface modified. Together with FePt-GA NPs solutions, two different MNPs inks were used to prepare MNPs grafting film on substrate. A preliminary test was performed by Norwood group and the FR behavior difference from the BCP composites were briefly discussed.

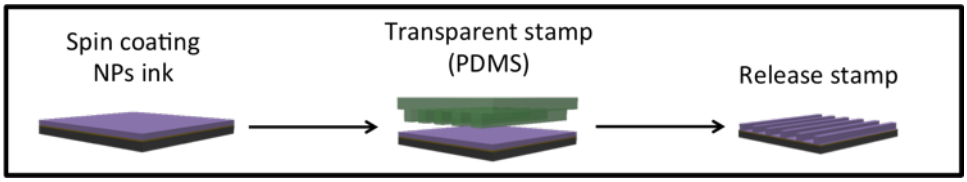

Figure 4.4 Nanoimprinting of MNPs using polar suspension and polydimethylsiloxane (PDMS) stamp. The feature sizes of pattern were transferred from a master substrate (courtesy to Yiliang Zhou for procedure sketch).

4.2 Experimental

4.2.1 Materials

4-Hydroxybenzoic acid (HBA) (99%) and gallic acid (GA) (98%), oleylamine (80%-90%) and oleic acid (97%) were purchased from Acros Organics. Dioctyl ether (99%), iron (0) pentacarbonyl (> 99.99% traces metals basis), platinum acetylacetonate (97%), homo polymer P2VP (M_n ~152 kg/mol, PDI ~1.04) were purchased from Sigma Aldrich. 1,2-hexadecanediol (>98%) was purchased from TCI America. Fe_3O_4, high purity, 99.5+%, 15-20 nm powders were purchased from US research nanomaterials, Inc. PS (102 kg/mol)-*b*-P2VP (97 kg/mol) f_{P2VP} ~ 48.7 %, PDI~1.12 was purchased from Polymer Source, Inc. Common solvents were purchased from Fisher Scientific. All reagents were used as received without further purification.

4.2.2 Preparation of Iron Platinum Nanoparticles

FePt NPs with core diameters from 1.9 to 9.3 nm were synthesized and surface-modified following established procedures.[4,78,79] Typically hexane was removed from each 50 mg of as-prepared FePt NPs solution (10 mg/mL) under a gentle nitrogen flow and 25 mg/mL GA (20 mL ethanol) solution was added immediately to the dried solids. The mixture was kept under sonication for two hours, and then left stirring overnight. The FePt-GA NPs were precipitated in a 200 mL 1:10 (v/v) ethanol/hexane mixture solvent with a neodymium magnet (2 inch × 2 inch × ½ inch, McMaster-Carr). Purified NPs were passed through a 0.2 μm PTFE filter and were stored in dimethylformamide (DMF).[79]

4.2.3 Preparation of Commercial Available Magnetic Nanofillers Ink

In a typical experiment, 100 mg commercial Fe_3O_4 MNP powders were mixed with 20 mL (25 mg/mL) HBA ethanol solution. The mixture was sonicated for at least 2 hours and kept stirring over night. The suspension was precipitated in a 100-150 mL 1:5 (ethanol/hexane) mixture solvent with a neodymium magnet. Purified NPs were passed through a 0.45 μm PTFE filter and then preserved in ethanol, DMF or 1,2-propendiol.

4.2.4 Preparation of Nanocomposite Films

FePt-GA NPs with different d_{core} with varied concentrations (from 0.1 %, 0.5 %, 1 %, 2.5 %, 5 %. 7.5 % to 10 wt %) were mixed with PS (102k)-*b*-P2VP (97k) freshly prepared solution. The concentration of the blend solution was diluted to 2 wt % (10 mg solid content) with a mixture solvent of tetrahydrofuran (THF)/DMF (v_T:v_D=7:3). The solution was then drop cast onto pre-cleaned glass slides (area ~ 1" × 3" inch square) and

dried at room temperature. The films were then annealed in saturated chloroform vapor at room temperature for at least 2 days, and then slowly dried in air for 1 day.

4.2.5 Preparation of Imprinted Nanoparticles Films

The feature sizes of PDMS stamps were transferred from the master substrate by crosslinking commercial Sylgard 184 silicone. Two feature sizes were utilized: pitch 1000 nm, width 500 nm, height 500 nm and pitch 480 nm, width 240 nm, height 100 nm, respectively. The MNP solutions were either in DMF or 4:1 volume ratio of ethanol and 1,2-propendiol at high concentration 80-100 mg/mL. The PDMS stamp were immediately pressed on the spincoated film (2000-3000 rpm, 30-45 seconds, dependent of ink concentration) and dried on a hot plate for 2 hours. The stamp was gently pealed off from the film when solvent was completely removed. A well-formed grating film usually displays shining color.[81]

4.2.6 Characterization

Transmittance electron microscopy (TEM) was carried out with a JEOL 2000FX (accelerating voltage of 200kV) to investigate NP size and composite morphology. The samples were prepared by dropping dilute NP solution onto a thin carbon film supported by a copper grid. The size distribution of NPs was analyzed for a sample size of 300-400 particles with a standard image analysis software (*Image J*). Electron diffraction images of NPs were calibrated with gold deposited carbon film. *Thermogravimetric analysis* (TGA) was performed on TA Instruments Q500, and the weight fraction of the FePt metal core was measured from 20 ° C to 800 °C at 10 °C/min under an air purge flow. *X-ray diffraction* (XRD) was performed using a Panalytical X-pert X-ray powder

diffractometer and X-ray reflectometer. The crystal structures of FePt NPs of varioius sizes were characterized with 5-10 mg FePt NPs powders with a 2θ scan from 30° to 110°. *Vibrating sample magnetometer* (VSM) measurements were performed on a Microsense EZ9 with FePt NPs copolymer composite films at a room temperature. A solution was dropcast on a 5mm × 5 mm Si wafer for at least three times to yield the samples. *Ultraviolet–visible spectroscopy* (UV-vis) was performed on a Cary 5000 UV-Vis-NIR spectrometer to characterize the film absorption coefficient as a function of wavelength in the same regions of the thin films sampled in the thickness and Faraday rotation measurements. *Small angle X-ray scattering* (SAXS) was carried out on a Ganesha SAXS-LAB and performed with the Cu Kα 0.154 nm line. Bulk film was carefully scraped and secured in the center of a washer with Kapton tape. *Microtoming* was performed on a Leica Ultracut UCT microtome at a room temperature. Composite samples were prepared as 50 nm thin sections collected with carbon film on copper grids for microscopy, followed by subsequent iodine staining to increase P2VP domain contrast. *Profilometry* was performed on a Veeco Dektak 150 and the film thickness of the dropcast film was determined by contact mode with a minimum of three scans per film. *Atomic Force Microscopy* (AFM) was performed on SPM Dimension 3100 scanning probe microscope. *Scanning Electron Microscopy* (SEM) was carried on the FESEM Magellan 400. Because the grafting MNPs film might be ferromagnetic, only top-view mode was performed due to potential damage to the EM lens.

Faraday rotation measurements (**courtesy of the Norwood group**). The Verdet constants were measured in a two-pass sinusoidal magnetic field driven homodyne apparatus using a NewFocus Nirvana 2017 auto-differential detector with efficient

common-mode noise cancellation (Figure 4.3(b), courtesy to Norwood group). This detector employed in conjunction with a lock-in amplifier, allowed for accurate measurement of small Faraday rotations. Due to the nonreciprocal nature of FR, such a two-pass setup generates twice the rotation for a given magnetic field and cancels any rotation effect present that is reciprocal in nature. Inherent anisotropy in FePt NPs copolymer composites may generate such reciprocal rotations of the polarization as a result of circular birefringence and scattering. The sinusoidal output from the internal oscillator of the lock-in amplifier, a Stanford Research Systems SR830, was fed into a home-built low-noise amplifier/solenoid driver to create 20 to 400 gauss of sinusoidal magnetic flux density at the composite film. The magnetic fields were calibrated periodically using a Hall probe AC gauss meter. A polarization controller consisting of a half-wave plate and a high extinction-ratio linear polarizer produced the light in a known polarization state. After a non-polarizing beam splitter (NPBS), the light was passed through the sample twice, yielding a rotation of the linear polarization state of 2θ, where θ is directly proportional to the sample thickness, applied magnetic field, and Verdet constant. The transmitted light is then spatially separated into vertically and horizontally polarized components (denoted *s* and *p*) by a Wollaston prism, focused by a singlet lens, and detected with an auto-differential detector. The detector used here is an InGaAs (1000-1600 nm) based Nirvana autobalanced front-end receiver, Model 2017 from New Focus. The wavelengths used in these experiments are 850 nm, 980 nm, 1310 nm, and 1550 nm (all distributed feedback semiconductor diode lasers). Auto-balanced phase-sensitive detection was used to reduce common-mode laser noise reference correction. The measured rotation was generally recovered as a phase change, a ratiometric quantity,

unlike the more common traditional polarimetric method, i.e., through a polarizer/rotating analyzer.

4.3 Results and Discussions

4.3.1 Iron Platinum Nanoparticles Size Distributions

Four batches of FePt NPs were synthesized by reduction of platinum and iron precursors and the average d_{core} were measured as 1.9, 4.9, 5.7 and 9.3 nm with narrow size distributions. The TEM images and corresponding size distribution histograms are shown in Figure 4.5. After surface modification, the particles exhibited fair stability in polar solvents (e.g. DMF) without obvious aggregation, ensuring the selective dispersion in the P2VP domain. The particle geometry was observed to undergo a spherical to cubic transition as the particle core diameter increased, consistent with previous work.[78]

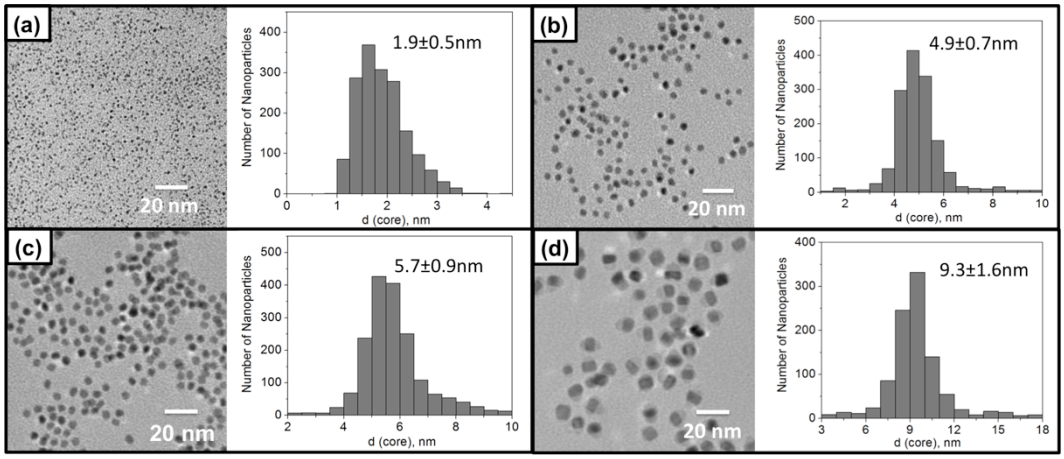

Figure 4.5 TEM images of FePt NPs and size distribution histogram: (a) 1.9 nm, (b) 4.9 nm, (c) 5.7 nm and (d) 9.3 nm of average core diameter. Spherical estimation was used for (a)-(c) and square geometry was applied to (d) in Image J analysis.

The core metal weight fraction of particles and the corresponding volume/filling fractions (f_{NP}) in the BCP were calculated and are provided in Table 4.1. Among the composites, f_{NP} ranged from 0.02 % to 4.8 % depending on particle size and loading. f_{NP}

was calculated with using the equation $f_{NP}=V_{NP}/(V_{NP}+V_{BCP})$, in which V_{NP} and V_{BCP} referred to NP and BCP volumes accordingly, with the following known or estimated densities: PS-*b*-P2VP ~ 1.05 g/cm^3, Fe ~7.8 g/cm^3, Pt ~ 21.3 g/cm^3 and GA~ 1.7 g/cm^3.[79] Fe and Pt atoms pack at a 1:1 mole ratio based on the synthesis protocol. NPs with d_{core} ~1.9 nm had comparatively high volume fraction due to insufficient GA stabilization for small FePt NPs; the excess free ligand was attributed to the low volume fraction compared to other samples. Because no apparent aggregation was observed in polar solvents, the NPs are believed to have strong H-bonding interactions with the P2VP domain.

Table 4.1 FePt NPs core weight percentage and volume fraction (f_{NP},%) in the nanocomposites

d_{core} [a] (nm)	Core[b] wt %	f_{NP}[c] 0.1wt %	f_{NP} 0.5wt %	f_{NP} 1.0 wt %	f_{NP} 2.5 wt %	f_{NP} 5 wt %	f_{NP} 7.5 wt %	f_{NP} 10 wt %
1.9	30	0.04	0.23	0.46	1.2	2.3	3.6	4.8
4.9	81	0.02	0.12	0.25	0.63	1.3	2.0	2.7
5.7	77	0.03	0.14	0.29	0.73	1.5	2.3	3.1
9.3	85	0.02	0.07	0.16	0.39	0.80	1.2	1.7

[a] Average core diameter as analyzed by Image J. [b] Inorganic weight fraction as measured by TGA. [c] Volume fraction of NPs as calculated according to ligand and polymer density.

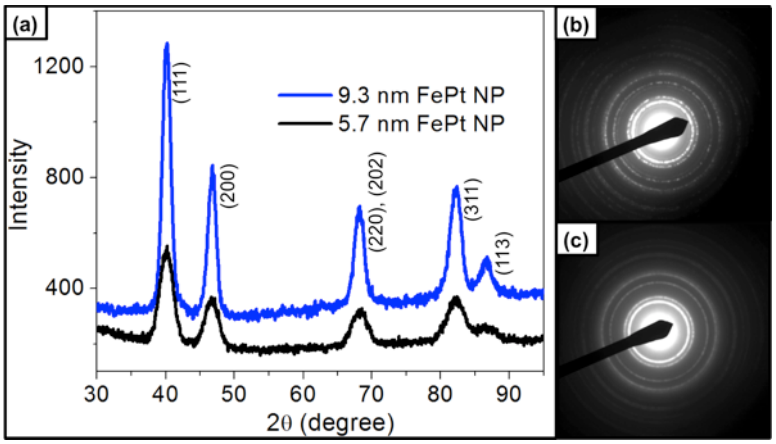

Figure 4.6 Crystal structure of size controlled FePt particles: (a) XRD spectrum of d_{core} ~ 5.7 nm and 9.3 nm FePt NPs powder, fcc characteristic peaks agree with previous results; (b) d_{core} ~ 9.3 nm and (c) d_{core} ~ 5.7 nm are electron diffraction images, the halo pattern corresponds to the XRD spectrum calibrated with a gold standard sample.

To further confirm the FePt MNPs structure, both electron and X-ray diffraction were conducted and indicated (Figure 4.6) face centered cubic (fcc) FePt lattice structures with characteristic peaks (111)/(200), (220)/(202) and (311)/(113). The strong and clear ring pattern in the electron diffraction spectra indicated high crystallinity of the FePt NPs. The identical 2θ angle, and the decrease of the full width at height maxima (FWHM) as the particles size increased agreed well with reported work.[4,77,78]

4.3.2 Morphology and Magnetism of Nanocomposite

SAXS was used to determine the NP/BCP blend morphology and domain spacing (d-spacing). Because paramagnetic materials are temperature sensitive, solvent annealing was adopted to avoid changes in the magnetic properties. As shown in Figure 4.7 (a), the SAXS 1D profiles of the polymer showed an obvious primary peak at $q^* = 0.087$ nm^{-1} suggesting phase separation of the composite with a d-spacing of 72 nm ($d = 2\pi/q^*$). This primary scattering signal remained apparent upon the addition of NPs indicating a persistent strong phase segregation of NP/BCP blends. The value of q* shifted to a slightly lower value, indicating that sequestration of NPs began to swell the block.

Figures 4.7 (b) and (c) (courtesy to Dr. Xinyu Wang) show that GA capped FePt NPs had selective dispersion in the P2VP domain (dark area stained with iodine). The paramagnetic NPs arrays could be self-assembled into the linear BCP template with NPs sizes less than 10 nm. Although high order reflection was not observed in the 1D spectrum, the TEM images confirmed that lamellae morphology was obtained through solvent annealing. The absence of higher order peaks may result from chain entanglements of high molecular weight BCPs that leads to slow ordering dynamics or from background scattering signals generated from the NPs. As stated in the introduction,

the hydrophilic FePt NPs have been shown to enhance BCP phase segregation. The detailed morphology trantion of FePt/BCP nanocomposite have been fully elaborated by Dr. Xinyu Wang.[80]

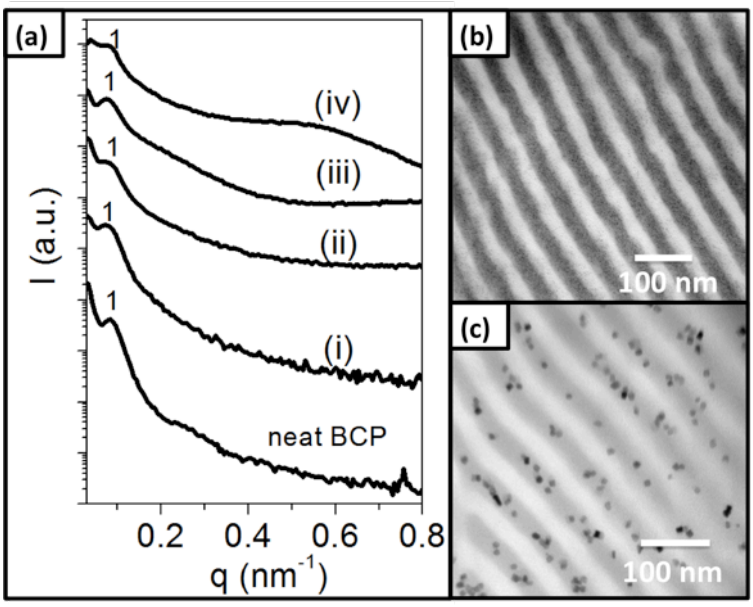

Figure 4.7 Room temperature SAXS profiles of neat PS (102 kg/mol)-*b*-P2VP (97 kg/mol) with (i) 1.9 nm, (ii) 4.9 nm, (iii) 5.7 nm and (iv) 9.3 nm FePt NPs at 2.5 wt % loading. TEM images of 10 wt % loading of (b) 1.9 nm NPs and (c) 9.3 nm NPs in BCP. The P2VP domain was lightly stained with iodine: particles show selective distribution through favorable H-bonding interactions (provided by Dr. Xinyu Wang).

The magnetization of prepared FePt NPs/BCP composites were correlated with increasing the core diameter of FePt NPs (Figure 4.8, measured by Dr. Palash Gangopadhyay). FePt NPs were paramagnetic at the room temperature (298 K), consistent with previous studies. There were no differences in magnetization between in-plane and out-of-plane measurement geometries indicating isotropic bulk magnetization in these films. Usually, paramagnetic materials produce induced fields along the direction of the applied field, and lose their magnetization upon removal of the applied field or at elevated temperatures higher than its Curie temperature. Paramagnetic NP/BCP composites, due to a lack of coercivity, are ideally suited for MO magnetic field sensor

applications, and the current study enabled us to choose candidate materials with maximum magnetization.[4,77] Phenomenologically, the wavelength dependent FR was directly proportional to the available volume magnetization of the transducing material. Because 4.9 nm and 5.7 nm FePt NPs have similar core diameters, a representative particle of close diameter (5.5 nm) was measured.

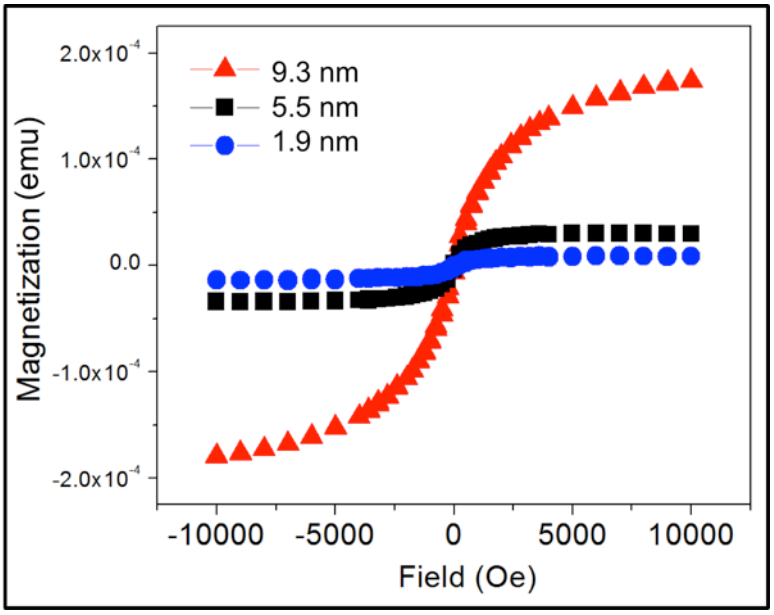

Figure 4.8 Hysteresis loops of 2.5 wt %1.9 nm, 5.5 nm and 9.3nm FePt NPs in PS (102 kg/mol)-*b*-P2VP (97 kg/mol) composite. The magnetization falls back to zero in absence of the applied magnetic field for all sizes of particles (the measurement was performed by Dr. Palash Gangopadhyay).

4.3.3 Verdet Constant versus Nanoparticles Loading

To determine the Verdet constant, the film thicknesses (L) of the composites were determined by surface profilometry (measured by Alexander Miles). The FePt NP BCP composite films were prepared by drop-casting onto a 3" × 1" inch glass slide, resulting in wide thickness variations. The spot size in the FR measurement setup is < 1mm^2, and measurements were carried out on multiple spots on each film.

Table 4.2 Film thickness measurement of resulting FePt/BCP composite

Wt% FePt	Avg. Thick (µm)	Avg Ra (nm)	Max Error (nm)	Uncertainty (%)
		Neat BCP		
0	3.17	57.3	69.80	2.20
		1.9 nm FePt-Composite		
0.1	7.62	71.6	298.95	3.92
0.5	8.44	66.7	456.40	5.41
1	8.34	70.6	1304.85	15.65
2.5	8.98	38.1	49.62	0.55
5	7.06	17.3	2299.67	32.57
7.5	8.86	523	636.24	7.18
10	7.96	53.2	120.12	1.51
		4.9 nm FePt Composite		
0.1	6.11	28.7	28.72	0.47
0.5	7.83	65.9	65.90	0.84
1	9.40	152	151.60	1.61
2.5	8.49	39.9	39.88	0.47
5	6.66	37.5	40.03	0.60
7.5	5.59	41.1	41.07	0.73
10	4.97	206	205.57	4.13
10*	10.74	81.8	836.00	7.79
15*	12.30	155	171.00	1.39
20*	11.43	93.5	691.00	6.04
25*	10.60	31.3	43.00	0.41
		5.7 nm FePt Composite		
0.1	11.21	439	581.87	5.19
0.5	6.29	46.1	979.53	15.56
1	7.39	168	1012.86	13.71
2.5	6.83	82.1	488.56	7.15
5	6.61	50.8	194.69	2.95
7.5	6.46	44.5	152.73	2.37
10	6.66	39.7	88.65	1.33
		9.3 nm FePt Composite		
0.1	10.08	312	483.43	4.80
0.5	10.69	651	686.18	6.42
1	9.68	602	754.62	7.80
2.5	7.12	101	378.31	5.31
5	5.98	94.0	109.13	1.83
7.5	7.70	75.0	179.06	2.33
10	7.10	79.2	143.58	2.02

Given that any error in the thickness measurement directly affects the calculated Verdet constant, thickness was measured only on the 1mm^2 segment of film actually used for each of the FR measurements. Thicknesses and corresponding uncertainties were taken into account during Verdet constant calculations and constitute the error bars in data plots (Table 4.2, measured by Alexander Miles).

The Verdet constant ($V = \theta/BL$) was determined through the FR measurements, in which the total rotation angle of the polarized light, film thickness, and applied magnetic field were measured. The FR performance contributed by the 1 mm thick glass substrate was accounted for at each wavelength in the NIR regime and the experimental values for the glass substrate were found to agree well with the existing literature (Table 4.3).

Table 4.3 Verdet constants (V) of the glass substrate

Wavelength (λ) (nm)	***V*** **(°/T·m)**
845	146.8
980	104.0
1310	74.0
1550	39.1

The measured Verdet constants for FePt NP/BCP composites are listed in Table 4.4. The Verdet constant of NP/BCP composites at 845 nm with 10 wt % loading and d_{core} ~ 4.8 nm FePt particles was as high as -6.3×10^4 °/T·m. The FR response of composite surpassed TGG, which has V was around ~ 8.3×10^3 °/T·m at 632 nm.[22] The Verdet constant of neat polymer film was measured as +12 °/T·m at 980nm, thus the strong MO response of the NP/BCP composite was introduced by the addition of FePt NPs. Unlike single crystal materials, this high Verdet constant NP/BCP composite was

prepared through a solution process, making versatile coating techniques and large area films on flexible substrates possible.

Table 4.4 Verdet constants (V) of FePt NP/BCP composite films (10^4 °/T·m), calculation and measurements by Norwood group

	λ=845 nm				**λ=980 nm**			
wt %/ d_{core}	1.9 nm	4.8 nm	5.7 nm	9.3 nm	1.9 nm	4.8 nm	5.7 nm	9.3 nm
0.10	-3.82	-5.25	-2.81	-3.18	-2.96	-3.52	-2.16	-2.18
0.50	-3.43	-4.09	-5.25	-2.99	-2.71	-2.95	-3.71	-2.05
1.00	-3.62	-3.27	-4.52	-3.18	-2.87	-2.05	-2.99	-2.27
2.50	-3.20	-3.71	-4.83	-4.42	-2.57	-2.70	-2.81	-3.27
5.00	-4.39	-4.79	-4.79	-5.34	-3.30	-3.46	-3.30	-3.84
7.50	-2.99	-5.51	-4.88	-4.00	-2.58	-4.13	-3.20	-2.35
10.00	-3.61	-6.27	-4.70	-4.40	-2.91	-4.70	-3.29	-3.18
	λ=1310 nm				**λ=1550 nm**			
wt%/ d_{core}	1.9 nm	4.8 nm	5.7 nm	9.3 nm	1.9 nm	4.8 nm	5.7 nm	9.3 nm
0.10	-1.09	-2.27	-1.22	-1.35	-1.16	-1.37	-0.37	-0.55
0.50	-0.98	-1.80	-2.21	-1.20	-1.01	-0.96	-0.67	-0.64
1.00%	-0.98	-1.45	-1.93	-1.43	-0.89	-0.91	-0.57	-0.58
2.50%	-0.90	-1.66	-2.07	-1.94	-0.90	-1.01	-0.62	-0.80
5.00%	-1.14	-2.10	-2.06	-2.25	-1.15	-1.26	-0.65	-0.79
7.50%	-0.91	-2.33	-2.10	-1.77	-0.90	-1.48	-0.68	-0.67
10.00%	-1.02	-2.79	-2.08	-1.90	-0.99	-1.74	-0.77	-0.70

[a]The given weight percentages include the capping layer of GA, results of 1.9 nm samples under longer wavelength are currently not available.

The Verdet constant of homopolymer/FePt composites under different wavelength was measured as a control group (Table 4.5). First, the absolute value of homopolymer composite was at least 2 magnitudes smaller than the BCP composite. This result confirmed that the nanostructures of BCP assist to direct the MNPs and reduce the light scattering loss. However, one phenomenon is unusual: the Verdet constant was positive rather than negative as expected. The inconsistence of homopolymer composite behavior is not completely explained so far. Serious chain entanglement or the inhomogeneity of MNPs dispersion in homopolymer matrix may be attributed to the unexpected results.

Table 4.5 Verdet constant of homopolymer/9.3 nm FePt-GA at 10 wt %

Wavelength (λ) (nm)	*V* (°/T·m)
980	848
1310	638
1550	442

4.3.4 Imprinted Films Morphology

The surface modified commercial MNPs had relatively stable dispersion in the polar solvent (Figure 4.9). The shapes of MNPs were not spherical but more like very irregular. Large MNPs aggregation could still be observed over 100 nm but less than 500 nm. The dispersion of commercial MNPs was not as good as FePt-GA NPs but stable enough for imprinting film on the glass or the Si substrate.

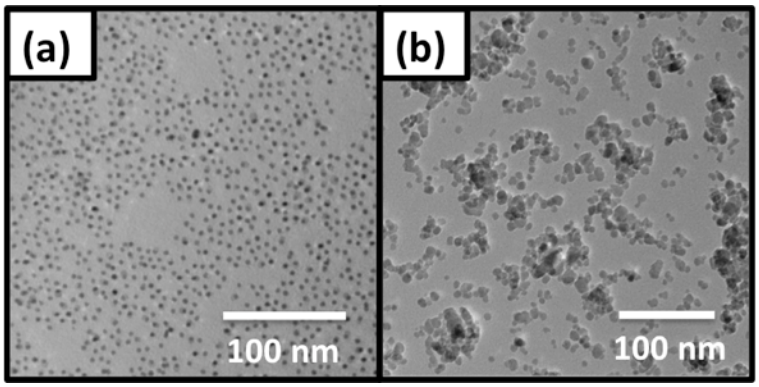

Figure 4.9 TEM images of (a) asymmetric X=3-4 nm, Y=5-7 nm FePt-GA NPs in DMF solution and (b) surface modified commercial MNPs (15-20 nm according to supplier) in 1,2-propendiol and ethanol, stabilized with HBA.

The morphology of imprinted films on Si substrate was then characterized by the AFM and SEM top-view (Figure 4.10). Qualities of Fe_3O_4 and FePt NPs imprinting films seemed to have the best results with the 500 nm PDMS stamp. The pitch and width of the master were completely transferred to the MNPs films while the height was left with an average height of 300 nm, which resulted from the evaporation of solvent. The height or

width of pillars may have further shrinkage under thermal calcination treatment.[81] In spite of the good control over the feature size, there are still remaining aggregated NPs on top of imprinted film, which was obvious in the SEM images. To get rid of these grains, smaller MNPs or better commercial suspension would be ideal.

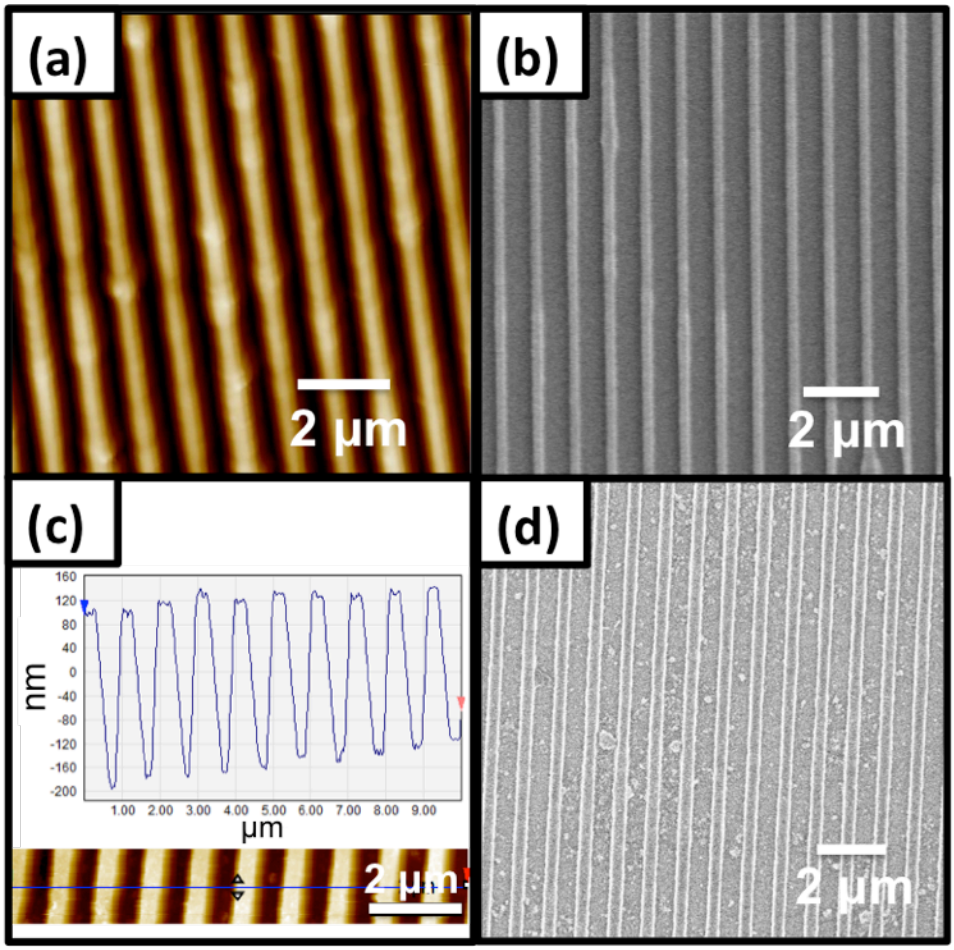

Figure 4.10 Morphology of imprinted films on Si wafer: (a) and (c) AFM and height profiles imprinted MNPs films using 500 nm PDMS stamp; (b) and (d) SEM images of FePt and Fe_3O_4 films respectively. All scale bars are 2 μm.

Rest samples tested with other feature size or MNPs showed poor control of film quality. Limited ink stability, low concentrations and solvent viscosity were attributed to the phenomenon. In spite of limited exploration of this MNPs imprinting, this method

still proved to be very useful in patterning the functional NPs for ideal nanostructures without organic polymer matrix.

Figure 4.11 shows the preliminary FR measurement of FePt films, measured by Dr. Palash Gangopadhyay. The imprinted film contained much higher magnetic species and feature sizes were 2-3 times larger compared to BCP based composites. Active MO performances were observed as well as polymer/MNPs composite. However, there were remains of polarization plane rotation after removal of magnetic fields due to the highly ordered pillar structures.

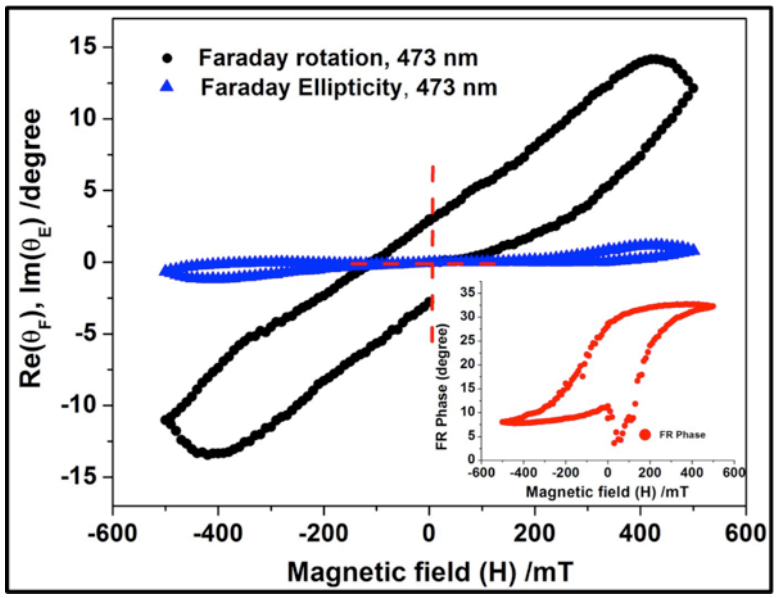

Figure 4.11 A preliminary FR response characterization of pillar structured FePt-GA NPs on glass substrate. The polarization plane of light can still be tilted after removal of the magnetic fields.

4.3.5 Summary

The self-assembly of MNPs and BCPs provides an effective strategy toward MO materials with Verdet constants up to ~ 10^4 °/T·m in the NIR regime at room temperature. The magnetic NPs introduce the improved FR performance, while neat polymer only has V~ 12 °/T·m under the same conditions. The Verdet constant of NP/BCP blends

decreased with increased measurement wavelength, consistent with paramagnetic composite behavior. In general, this method provides a simple route toward fabrication of high-performance MO material through a solution process. The method is compatible with dropcast-, spin-, rod- and blade-coating, providing the possibilities for the roll-to-roll processing over large area of next-generation functional materials.

The author acknowledges the Norwood group for the equal contributions and useful discussions of contents of Chapter 4.

4.4 References

(1) Frey, N. A.; Peng, S.; Cheng, K.; Sun, S. Magnetic Nanoparticles: Synthesis, Functionalization, and Applications in Bioimaging and Magnetic Energy Storage. *Chem. Soc. Rev.* **2009**, *38*, 2532–2542.

(2) Pankhurst, Q. a.; Thanh, N. T. K.; Jones, S. K.; Dobson, J. Progress in Applications of Magnetic Nanoparticles in Biomedicine. *J. Phys. D. Appl. Phys.* **2009**, *42*, 224001.

(3) Reddy, L. H.; Arias, J. L.; Nicolas, J.; Couvreur, P. Magnetic Nanoparticles: Design and Characerization,Toxicity and Biocompatibility,Pharmaceutical and Biomedical Applications. *Chem. Rev.* **2012**, *112*, 5818–5878.

(4) Sun, S. Recent Advances in Chemical Synthesis, Self-Assembly, and Applications of FePt Nanoparticles. *Adv. Mater.* **2006**, *18*, 393–403.

(5) Dong, Q.; Li, G.; Ho, C. L.; Faisal, M.; Leung, C. W.; Pong, P. W. T.; Liu, K.; Tang, B. Z.; Manners, I.; Wong, W. Y. A Polyferroplatinyne Precursor for the Rapid Fabrication of L1 0-FePt-Type Bit Patterned Media by Nanoimprint Lithography. *Adv. Mater.* **2012**, *24*, 1034–1040.

(6) Guo, Q.; Teng, X.; Yang, H. Fabrication of Magnetic FePt Patterns from Langmuir-Blodgett Films of Platinum-Iron Oxide Core-Shell Nanoparticles. *Adv. Mater.* **2004**, *16*, 1337–1341.

(7) Suits, J. C. Faraday and Kerr Effects in Magnetic Compounds. *IEEE Trans. Magn.* **1972**, *8*, 95–105.

(8) Zvezdin, A. K.; Kotov, V. A. *Studies in Condensed Matter Physics. Mordern Magnetooptics and Magnetooptical Materials*; Coey, J. M. D.; Tilley, D. R., Eds.; Institute of Physics Publishing: London, 1997, pp3-38.

(9) Bahuguna, R.; Mina, M.; Tioh, J. W.; Weber, R. J. Magneto-Optic-Based Fiber Switch for Optical Communications. *IEEE Trans. Magn.* **2006**, *42*, 3099–3101.

(10) Belotelov, V. I.; Kreilkamp, L. E.; Akimov, I. A.; Kalish, A. N.; Bykov, D. A.; Kasture, S.; Yallapragada, V. J.; Gopal, A. V.; Grishin, A. M.; Khartsev, S. I.; *et al.* Plasmon-Mediated Magneto-Optical Transparency. *Nat. Commun.* **2013**, *4*, 2128.

(11) Belotelov, V. I.; Akimov, I. a.; Pohl, M.; Kotov, V. a; Kasture, S.; Vengurlekar, a S.; Gopal, A. V.; Yakovlev, D. R.; Zvezdin, a K.; Bayer, M. Enhanced Magneto-Optical Effects in Magnetoplasmonic Crystals. *Nat. Nanotechnol.* **2011**, *6*, 370–376.

(12) Caicedo, M.; Pascu, O.; Jos, A.; Fontcuberta, J.; Roig, A.; Herranz, G.; Uab, C.; Juana, C. S. Magnetophotonic Response of Three- Dimensional Opals. *ACS Nano* **2011**, *5*, 2957–2963.

(13) Silva, R. M.; Martins, H.; Nascimento, I.; Baptista, J. M.; Ribeiro, A. L.; Santos, J. L.; Jorge, P.; Frazão, O. Optical Current Sensors for High Power Systems: A Review. *Appl. Sci.* **2012**, *2*, 602–628.

(14) Stadler, B. J. H.; Mizumoto, T. Integrated Magneto-Optical Materials and Isolators: A Review. *IEEE Photonics J.* **2014**, *6*, 600215.

(15) Taccola, S.; Greco, F.; Zucca, A.; Innocenti, C.; Fernandez, C.; Campo, G.; Sangregorio, C.; Mazzolai, B.; Mattoli, V. Characterization of Free-Standing PEDOT:PSS/iron Oxide Nanoparticle Composite Thin Films and Application as Conformable Humidity Sensors. *ACS Appl. Mater. Interfaces* **2013**, *5*, 6324–6332.

(16) Ziolo, R. F.; Giannelis, E. P.; Weinstein, B. A.; O'Horo, M. P.; Ganguly, B. N.; Mehrota, V.; Russel, M. W.; Huffman, D. R. Matrix-Mediated Synthesis of Nanocrystalline Y-Fe3O4: A New Optically Transparente Magnetic Material. *Science.* **1992**, *257*, 219–223.

(17) Zu, P.; Chan, C. C.; Koh, G. W.; Lew, W. S.; Jin, Y.; Liew, H. F.; Wong, W. C.; Dong, X. Enhancement of the Sensitivity of Magneto-Optical Fiber Sensor by Magnifying the Birefringence of Magnetic Fluid Film with Loyt-Sagnac Interferometer. *Sensors Actuators, B Chem.* **2014**, *191*, 19–23.

(18) https://en.wikipedia.org/wiki/Faraday_effect.

(19) Ando, K.; Saito, H.; Jin, Z.; Fukumura, T.; Kawasaki, M.; Matsumoto, Y.; Koinuma, H. Magneto-Optical Properties of ZnO-Based Diluted Magnetic Semiconductors. *J. Appl. Phys.* **2001**, *89*, 7284–7286.

(20) Crassee, I.; Levallois, J.; Walter, A. L.; Ostler, M.; Bostwick, A.; Rotenberg, E.; Seyller, T.; van der Marel, D.; Kuzmenko, A. B. Giant Faraday Rotation in Single- and Multilayer Graphene. *Nat. Phys.* **2010**, *7*, 48–51.

(21) Demir, V.; Gangopadhyay, P.; Norwood, R. A.; Peyghambarian, N. Faraday Rotation of Cobalt Ferrite Nanoparticle Polymer Composite Films at Cryogenic Temperatures. *Appl. Opt.* **2014**, *53*, 2087–2092.

(22) Gangopadhyay, P.; Voorakaranam, R.; Lopez-Santiago, A.; Foerier, S.; Thomas, J.; Norwood, R. A.; Persoons, A.; Peyghambarian, N. Faraday Rotation Measurements on Thin Films of Regioregular Alkyl-Substituted Polythiophene Derivatives. *J. Phys. Chem. C* **2008**, *112*, 8032–8037.

(23) Pustelny, S.; Wojciechowski, A.; Gring, M.; Kotyrba, M.; Zachorowski, J.; Gawlik, W. Magnetometry Based on Nonlinear Magneto-Optical Rotation with Amplitude-Modulated Light. *J. Appl. Phys.* **2008**, *103*, 63108.

(24) Shuto, Y.; Tanaka, M.; Sugahara, S. Magneto-Optical Properties of Group-IV Ferromagnetic Semiconductor Ge 1 − X Fe X Grown by Low-Temperature Molecular Beam Epitaxy. *J. Appl. Phys.* **2006**, *99*, 08D516.

(25) Yumoto, G.; Yoo, J. Y.; Matsunaga, R.; Tanabe, S.; Hibino, H.; Morimoto, T.; Aoki, H.; Shimano, R. Quantum Faraday and Kerr Rotations in Graphene. *Nat. Commun.* **2013**, *4*, 1841–1846.

(26) Schmidt, M. A.; Wondraczek, L.; Lee, H. W.; Granzow, N.; Da, N.; Russell, P. S. J. Complex Faraday Rotation in Microstructured Magneto-Optical Fiber Waveguides. *Adv. Mater.* **2011**, *23*, 2681–2688.

(27) Gao, G.; Winterstein-Beckmann, A.; Surzhenko, O.; Dubs, C.; Dellith, J.; Schmidt, M. a.; Wondraczek, L. Faraday Rotation and Photoluminescence in Heavily Tb3+-Doped GeO2-B2O3-Al2O3-Ga2O3 Glasses for Fiber-Integrated Magneto-Optics. *Sci. Rep.* **2015**, *5*, 8942.

(28) Borrelli, N. Faraday Rotation in Glasses. *J. Chem. Phys.* **1964**, *41*, 3289–3293.

(29) Zayat, M.; Del Monte, F.; Del Puerto Morales, M.; Rosa, G.; Guerrero, H.; Serna, C. J.; Levy, D. Highly Transparent Fe2O3/Vycor-Glass Magnetic Nanocomposites Exhibiting Faraday Rotation. *Adv. Mater.* **2003**, *15*, 1809–1812.

(30) Majeed, H.; Shaheen, A.; Anwar, M. Complete Stokes Polarimetry of Magneto-Optical Faraday Effect in a Terbium Gallium Garnet Crystal at Cryogenic Temperatures. *Opt. Express* **2013**, *21*, 25148–25158.

(31) Mikhaylovskiy, R. V.; Hendry, E.; Kruglyak, V. V. Ultrafast Inverse Faraday Effect in a Paramagnetic Terbium Gallium Garnet Crystal. *Phys. Rev. B* **2012**, *86*, 100405(R).

(32) Villaverde, A. B.; Donatti, D. A.; Bozinis, D. G. Terbium Gallium Garnet Verdet Constant Measurements with Pulsed Magnetic Field. *J. Phys. C Solid State Phys.* **1978**, *11*, L495–L498.

(33) Laulajainen, M.; Paturi, P.; Raittila, J.; Huhtinen, H.; Abrahamsen, A. B.; Andersen, N. H.; Laiho, R. BixY3-xFe5O12 Thin Films Prepared by Laser Ablation for Magneto-Optical Imaging of Superconducting Thin Films. *J. Magn. Magn. Mater.* **2004**, *279*, 218–223.

(34) Lacklison, D. E.; Scott, G. B.; Ralph, H. I.; Page, J. L. Garnets with High Magnetooptic Figures of Merit in the Visible Region. *IEEE Trans. Magn.* **1973**, *9*, 457–460.

(35) Sung, S. Y.; Qi, X.; Stadler, B. J. H. Integrating Yttrium Iron Garnet onto Nongarnet Substrates with Faster Deposition Rates and High Reliability. *Appl. Phys. Lett.* **2005**, *87*, 121111.

(36) Doormann, V.; Krumme, J. P.; Lenz, H. Optical and Magneto-Optical Tensor Spectra of Bismuth-Substituted Yttrium-Iron-Garnet Films. *J. Appl. Phys.* **1990**, *68*, 3544–3553.

(37) Veis, M.; Liskova, E.; Antos, R.; Visnovsky, S.; Kumar, N.; Misra, D. S.; Venkataramani, N.; Prasad, S.; Krishnan, R. Polar and Longitudinal Magneto-Optical Spectroscopy of Bismuth Substituted Yttrium Iron Garnet Films Grown by Pulsed Laser Deposition. *Thin Solid Films* **2011**, *519*, 8041–8046.

(38) Takeuchi, H. The Faraday Effect of Bismuth Substituted Rare-Earth Iron Garnet. *Jpn. J. Appl. Phys.* **1975**, *14*, 1903–1910.

(39) Beecroft, L. L.; Ober, C. K. Nanocomposite Materials for Optical Applications. *Chem. Mater.* **1997**, *9*, 1302–1317.

(40) Yogo, T.; Nakamura, T.; Sakamoto, W.; Hirano, S. Synthesis of Transparent Magnetic Particle/organic Hybrid Film Using Iron-Organics. *J. Mater. Res.* **2000**, *15*, 2114–2120.

(41) Cui, H.; Wang, M.; Ren, W.; Liu, Y.; Zhao, Y. Highly Transparent Silica Monoliths Embedded with High Concentration Oxide Nanoparticles. *J. Sol-Gel Sci. Technol.* **2013**, *66*, 512–517.

(42) García, R.; Ramírez-Del-Solar, M.; González-Leal, J. M.; Blanco, E.; Domínguez, M. Improving Magnetooptical Faraday Effect of Maghemite/silica Nanocomposites. *Mater. Chem. Phys.* **2015**, *154*, 1–9.

(43) Domínguez, M.; Ortega, D.; Garitaonandía, J. S.; Litrán, R.; Barrera-Solano, C.; Blanco, E.; Ramírez-del-Solar, M. Magneto-Optic Faraday Effect in Maghemite Nanoparticles/silica Matrix Nanocomposites Prepared by the Sol-Gel Method. *J. Magn. Magn. Mater.* **2008**, *320*, e725–e729.

(44) Moreno, E. M.; Zayat, M.; Morales, M. P.; Serna, C. J.; Roig, A.; Levy, D. Prepartion of Narrow Size Distribution Superparamagnetic γ -Fe 2 O 3 Nanoparticles in a Sol-Gel Transparent SiO2 Matrix. *Langmuir* **2002**, *18*, 4972–4978.

(45) Tartaj, P.; González-Carreño, T.; Serna, C. J. Single-Step Nanoengineering of Silica Coated Maghemite Hollow Spheres with Tunable Magnetic Properties. *Adv. Mater.* **2001**, *13*, 1620–1624.

(46) Zhou, Z. H.; Xue, J. M.; Chan, H. S. O.; Wang, J. Transparent Magnetic Composites of ZnFe2O4 Nanoparticles in Silica. *J. Appl. Phys.* **2001**, *90*, 4169–4174.

(47) Bonanni, V.; Bonetti, S.; Pakizeh, T.; Pirzadeh, Z.; Chen, J.; Nogués, J.; Vavassori, P.; Hillenbrand, R.; Åkerman, J.; Dmitriev, A. Designer Magnetoplasmonics with Nickel Nanoferromagnets. *Nano Lett.* **2011**, *11*, 5333–5338.

(48) Armelles, G.; Cebollada, A.; García-Martín, A.; González, M. U. Magnetoplasmonics: Combining Magnetic and Plasmonic Functionalities. *Adv. Opt. Mater.* **2013**, *1*, 10–35.

(49) Wang, L.; Clavero, C.; Huba, Z.; Carroll, K. J.; Carpenter, E. E.; Gu, D.; Lukaszew, R. A. Plasmonics and Enhanced Magneto-Optics in Core− Shell Co− Ag Nanoparticles. *Nano Lett.* **2011**, *11*, 1237–1240.

(50) Jain, P. K.; Xiao, Y.; Walsworth, R.; Cohen, A. E. Surface Plasmon Resonance Enhanced Magneto-Optics (SuPREMO): Faraday Rotation Enhancement in Gold-Coated Iron Oxide Nanocrystals. *Nano Lett.* **2009**, *9*, 1644–1650.

(51) Moocarme, M.; Dominguez-Juarez, J. L.; Vuong, L. T. Ultra-Low-Intensity Magneto-Optical and Mechanical Effects in Metal Nanocolloids. *Nano Lett.* **2014**, *14*.

(52) Lopez-Santiago, A.; Grant, H. R.; Gangopadhyay, P.; Voorakaranam, R.; Norwood, R. A.; Peyghambarian, N. Cobalt Ferrite Nanoparticles Polymer Composites Based All-Optical Magnetometer. *Opt. Mater. Express* **2012**, *2*, 978–986.

(53) Lopez-Santiago, A.; Gangopadhyay, P.; Thomas, J.; Norwood, R. A.; Persoons, A.; Peyghambarian, N. Faraday Rotation in Magnetite-Polymethylmethacrylate Core-Shell Nanocomposites with High Optical Quality. *Appl. Phys. Lett.* **2009**, *95*, 143302.

(54) Savchuk, A. I.; Stolyarchuk, I. D.; Makoviy, V. V; Savchuk, O. A. Magneto-Optical Faraday Rotation of Semiconductor Nanoparticles Embedded in Dielectric Matrices. *Appl. Opt.* **2014**, *53*, B22–B26.

(55) Kim, T. Y.; Yamazaki, Y.; Hirano, T. Magneto-Optical Properties of Bi-YIG Nanoparticle with Polymethacrylate Matrix Materials. *Phys. Status Solidi* **2004**, *241*, 1601–1604.

(56) Hayashi, K.; Fujikawa, R.; Sakamoto, W.; Inoue, M.; Yogo, T. Synthesis of Highly Transparent Lithium Ferrite Nanoparticle/polymer Hybrid Self-Standing Films Exhibiting Faraday Rotation in the Visible Region. *J. Phys. Chem. C* **2008**, *112*, 14255–14261.

(57) Kumar, G.; Mahajan, S. M. Wavelength Dispersion of Verdet Constant in E-Field Oriented Iron Oxide Doped Polymer Nanocomposites. *Proc. IEEE Sensors* **2013**, 6–8.

(58) Bockstaller, M. R.; Mickiewicz, R. a.; Thomas, E. L. Block Copolymer Nanocomposites: Perspectives for Tailored Functional Materials. *Adv. Mater.* **2005**, *17*, 1331–1349.

(59) Lee, J.-Y.; Thompson, R. B.; Jasnow, D.; Balazs, A. C. Entropically Driven Formation of Hierarchically Ordered Nanocomposites. *Phys. Rev. Lett.* **2002**, *89*, 155503.

(60) Lopes, W. A.; Jaeger, H. M. Hierarchical Self-Assembly of Metal Nanostructures on Diblock Copolymer Scaffolds. *Nature* **2001**, *414*, 735–738.

(61) Balazs, A. C.; Emrick, T.; Russell, T. P. Nanoparticle Polymer Composites: Where Two Small Worlds Meet. *Science.* **2006**, *314*, 1107–1110.

(62) Kao, J.; Thorkelsson, K.; Bai, P.; Rancatore, B. J.; Xu, T. Toward Functional Nanocomposites: Taking the Best of Nanoparticles, Polymers, and Small Molecules. *Chem. Soc. Rev.* **2013**, *42*, 2654–2678.

(63) Jang, S. G.; Kramer, E. J.; Hawker, C. J. Controlled Supramolecular Assembly of Micelle-like Gold Nanoparticles in PS-B-P2VP Diblock Copolymers via Hydrogen Bonding. *J. Am. Chem. Soc.* **2011**, *133*, 16986–16996.

(64) Song, D. P.; Lin, Y.; Gai, Y.; Colella, N. S.; Li, C.; Liu, X. H.; Gido, S.; Watkins, J. J. Controlled Supramolecular Self-Assembly of Large Nanoparticles in Amphiphilic Brush Block Copolymers. *J. Am. Chem. Soc.* **2015**, *137*, 3771–3774.

(65) Song, D. P.; Li, C.; Colella, N. S.; Xie, W.; Li, S.; Lu, X.; Gido, S.; Lee, J. H.; Watkins, J. J. Large-Volume Self-Organization of Polymer/Nanoparticle Hybrids with Millimeter-Scale Grain Sizes Using Brush Block Copolymers. *J. Am. Chem. Soc.* **2015**, *137*, 12510–12513.

(66) Jang, S. G.; Khan, A.; Hawker, C. J.; Kramer, E. J. Morphology Evolution of PS-B-P2VP Diblock Copolymers via Supramolecular Assembly of Hydroxylated Gold Nanoparticles. *Macromolecules* **2012**, *45*, 1553–1561.

(67) Lin, Y.; Daga, V. K.; Anderson, E. R.; Gido, S. P.; Watkins, J. J. Nanoparticle-Driven Assembly of Block Copolymers: A Simple Route to Ordered Hybrid Materials. *J. Am. Chem. Soc.* **2011**, *133*, 6513–6516.

(68) Ye, T.; Chen, X.; Fan, X.; Shen, Z. Ordered Gold Nanoparticle Arrays Obtained with Supramolecular Block Copolymers. *Soft Matter* **2013**, *9*, 4715–4724.

(69) Zhao, Y.; Thorkelsson, K.; Mastroianni, A. J.; Schilling, T.; Luther, J. M.; Rancatore, B. J.; Matsunaga, K.; Jinnai, H.; Wu, Y.; Poulsen, D.; *et al.* Small-Molecule-Directed Nanoparticle Assembly towards Stimuli-Responsive Nanocomposites. *Nat. Mater.* **2009**, *8*, 979–985.

(70) Yao, L.; Lin, Y.; Watkins, J. J. Ultrahigh Loading of Nanoparticles into Ordered Block Copolymer Composites. *Macromolecules* **2014**, *47*, 1844–1849.

(71) Wei, Q.; Lin, Y.; Anderson, E. R.; Briseno, A. L.; Gido, S. P.; Watkins, J. J. Additive-Driven Assembly of Block Copolymer-Nanoparticle Hybrid Materials for Solution Processable Floating Gate Memory. *ACS Nano* **2012**, *6*, 1188–1194.

(72) Song, D.-P.; Li, C.; Li, W.; Watkins, J. J. Block Copolymer Nanocomposites with High Refractive Index Contrast for One-Step Photonics. *ACS Nano* **2016**, *10*, 1216–1223.

(73) Song, D. P.; Li, C.; Colella, N. S.; Lu, X.; Lee, J.-H.; Watkins, J. J. Thermally Tunable Metallodielectric Photonic Crystals from the Self-Assembly of Brush Block Copolymers and Gold Nanoparticles. *Adv. Opt. Mater.* **2015**, *3*, 1169–1175.

(74) Yang, X.; Liu, C.; Ahner, J.; Yu, J.; Klemmer, T.; Johns, E.; Weller, D. Fabrication of FePt Nanoparticles for Self-Organized Magnetic Array. *J. Vac. Sci. Technol. B* **2004**, *22*, 31–34.

(75) Bublat, T.; Goll, D. Large-Area Hard Magnetic L10-FePt Nanopatterns by Nanoimprint Lithography. *Nanotechnology* **2011**, *22*, 315301.

(76) Gerritsma, R.; Whitlock, S.; Fernholz, T.; Schlatter, H.; Luigjes, J. A.; Thiele, J. U.; Goedkoop, J. B.; Spreeuw, R. J. C. Lattice of Microtraps for Ultracold Atoms Based on Patterned Magnetic Films. *Phys. Rev. A* **2007**, *76*, 33408.

(77) Sun, S. C.B. Murray, D. Weller, L. Folks, A. M. Monodisperse FePt Nanoparticles and Ferromagnetic FePt Nanocrystal Superlattices. *Science.* **2000**, *287*, 1989–1992.

(78) Nandwana, V.; Nandwana, V.; Elkins, K. E.; Elkins, K. E.; Poudyal, N.; Poudyal, N.; Chaubey, G. S.; Chaubey, G. S.; Yano, K.; Yano, K.; *et al.* Size and Shape Control of Monodisperse FePt Nanoparticles. *J. Phys. Chem. C* **2007**, *111*, 4185–4189.

(79) Wang, X.; Tilley, R. D.; Watkins, J. J. Simple Ligand Exchange Reactions Enabling Excellent Dispersibility and Stability of Magnetic Nanoparticles in Polar Organic, Aromatic, and Protic Solvents. *Langmuir* **2014**, *30*, 1514–1521.

(80) Wang, X. Thesis: Functional Nanocomposites from Self-Assembly of Block Copolymers with Nanoparticles, University of Massachusetts, Amherst, 2014.

(81) Kothari, R. Thesis: (I) Polymer Nanocomposites : Rheology and Processing for Mesoporous Materials and (II) Nanopatterning of Metal Oxides Using Soft Lithography, University of Massachusetts, Amherst, 2016.

CHAPTER 5

SUMMARY AND OUTLOOK

5.1 Incorporation of Large Functional Nanoparticles into Ordered Composite

The first project systematically investigated the spatial distribution of gold nanoparticles (NP) ranging in size up to 0.8 times that of the target domain width in symmetric polystyrene-*block*-poly (2-vinylpyridine) (PS-*b*-P2VP) using hydrogen bonding-mediated (H-bonding) assembly. NP with core diameters (d_{core}) 2 nm, 5 nm, 9 nm and 15 nm, are coated with ligands bearing phenol groups as the hydrogen donating sites for H-bonding including 2-(11-mercaptoundecyl) hydroquinone and thiol-terminated poly (4-hydroxystyrene). These hydroxylated NPs are selectively incorporated into the P2VP block (domain width L = 7-37nm) over a wide range of volume fractions (ϕ = 3 vol %- 26 vol %). Particles distributions are biased towards the center of in the P2VP domains when d_{core}/L is greater than 0.3 and are otherwise uniformly distributed within the target domain. The H-bonding interactions between NP and BCP provide favorable enthalpic interaction to overcome the inherent entropy penalties mainly arising from polymer chain stretching upon the sequestration of large particles. This strong thermodynamic driving force provides a means of incorporating relatively large NPs within BCP templates to further enable the preparation of well-ordered composites that can take advantage of the attractive size-dependent properties of NPs.

Recently, our group has demonstrated a simple strategy for preparation of large-area porous hybrid films containing silica, carbon and gold on flexible substrate via photothermal processing (Figure 5.1).[1] The films was constructed by self-assembly of sacrificial BCPs, Au NPs and cross-linked silsesquioxane, in which the polymer and

silica source provided the frame of mesopores and the Au NPs served as nanoheaters to transform light as heat.

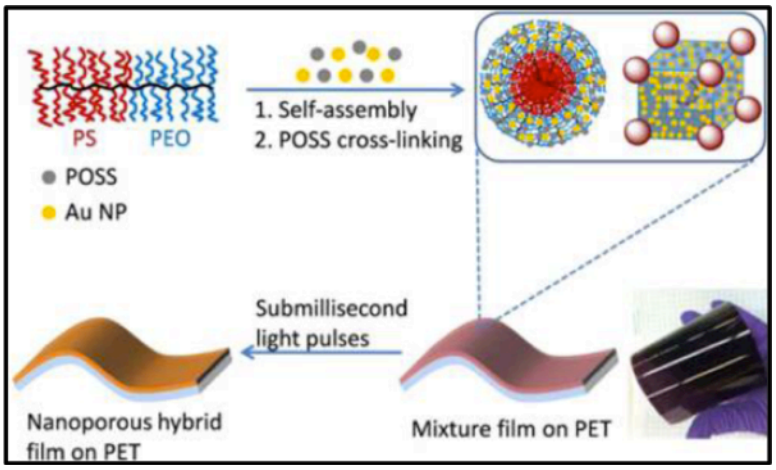

Figure 5.1 Illustration of a rapid and scalable process for the synthesis of hierarchical porous hybrid films of silica, carbon and gold on flexible substrate via photothermal treatment (adapted from reference 1 in Chapter 5).

After photothermal treatment, the organic residues were removed and the films formed with uniform mesopores from 44-48 nm and interconnected macropores of more than 50 nm. Such hybrid material can be utilized in the electrode material due to the large surface area of conductive carbon and Au composition. The rapid photothermal treatment was completed in submillisecond, providing the opportunities for scaling-up to roll-to-roll processing of large area electronic device.

In the future, such hybrid porous materials are not limited to Au NPs, utilization of cheaper additives including iron oxides, graphene or graphene oxides, silicon NPs provides more possibilities for photothermal treatment. The resulting films are next-generation promising electrode materials for lithium ion batteries or super-capacitors.[2–5]

5.2 High Molecular Mobility of Brush Block Copolymers

A systematic study was conducted to investigate the morphology transitions that occur in polystyrene-*block*-poly (ethylene oxide) (PS-*b*-PEO) bottlebrush block copolymers (BBCP) upon varying PEO volume fraction (f_{PEO}) from 22 % to 81 %. A series of PS-*b*-PEO BBCPs with different PEO side chain lengths were prepared using ring opening metathesis polymerization (ROMP) of PEO-norbornene (PEO-NB) (M_n ~ 0.75, 2.0 or 5.0 kg/mol) and PS-norbornene (PS-NB) (M_n ~ 3.5 kg/mol) macromonomers (MM). A map of f_{PEO} *versus* side chain asymmetry (M_n (PEO-NB)/M_n (PS-NB)) was constructed to describe the BBCP phase behavior. Symmetric and asymmetric lamellar morphologies were observed in the BBCPs over an exceptionally wide range of f_{PEO} from 28 % to 72 %. At high f_{PEO}, crystallization of PEO was evident. Temperature controlled SAXS and WAXS revealed the presence of high order reflections arising from phase segregation above the PEO melting point. A microphase transition temperature T_{MST} was observed over a temperature range of 150-180 °C. This temperature was relatively insensitive to both side chain length and volume fraction variations. The findings in this study provide insight into the rich phase behavior of this relatively new class of macromolecules, and may lay the groundwork for their use as templates directing the fabrication of functional materials.

The morphology investigation of BBCP was not enough. Recently, our group also has demonstrated the rheological study of PS-*b*-PEO BBCPs and provides the solid proof that such macromolecules have high molecular mobility (Figure 5.2).[6] The dynamic master curves of G' (storage modulus) and G"(loss modulus) of BBCPs were built up at a reference temperature of 120 °C. In the intermediate regime, on rubbery plateau was

observed, which usually appeared in the linear polymer rheological response. The absence of rubbery plateau confirmed that the short side chain of BBCP did not have chain entanglement. Even at lower frequency, the entanglement of norbornene backbone was not observed either. The integral performance confirmed that high molecular mobility of BBCP of short side branches.

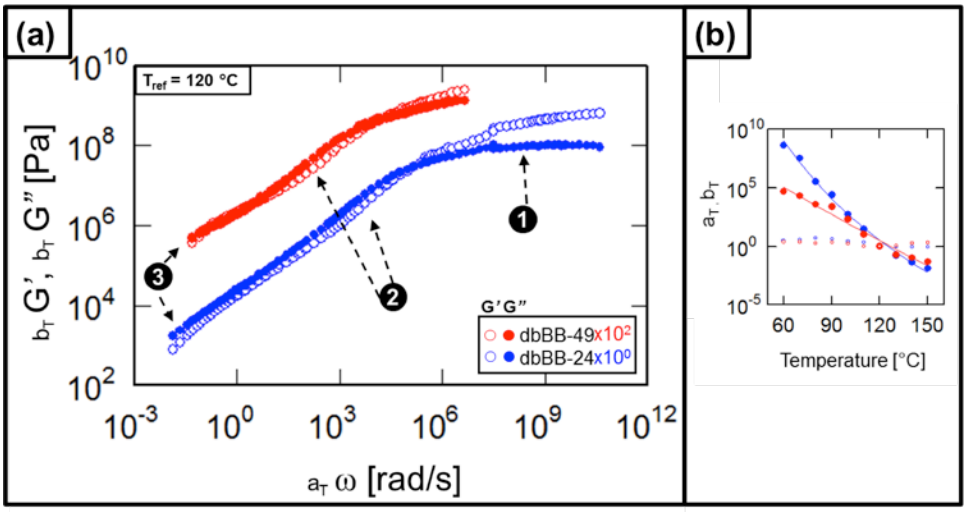

Figure 5.2 Dynamic Master Curves of G' (open symbols) and G" (closed symbols) for PS-*b*-PEO BBCP samples at a reference temperature of T_{ref} = 120 °C. Labels indicate the following features (1) Glassy region, (2) Intermediate (Backbone) Relaxation, (3) Confined Terminal Flow. Curves shifted vertically by indicated scaling factors to provide clarity. b) Time Temperature Superposition shift factors a_T (closed symbols) and b_T (open symbols) for master curve. Line shows fit to WLF equation (adapted from reference 6 in Chapter 5).

More questions of the BBCP linear viscoelasticity needed to be answered. Due to the testing temperature, rheological behavior under low frequency was not quite clear. The phase segregation of BBCPs may play a role in the "terminal flow" regime and the rheological response should differ from the homo-brush polymers.[7–9] There are several limitations current PS-*b*-PEO BBCPs for rheology study: (1) crystallization of PEO block, (2) glass transition of PS block and (3) the relatively weak long range ordering. In

order to better investigate the BBCPs behavior at low frequency, samples of long-range ordering and non-crystallized blocks would be of great interest.

5.3 Anisotropic Magnetic Nanocomposite

Magneto-optical (MO) composites with excellent Faraday rotation (FR) response were fabricated using iron platinum (FePt) nanoparticles (NPs) and polystyrene-*block*-poly (2-vinyl pyridine) (PS-*b*-P2VP) block copolymers (BCPs). Gallic acid (GA) functionalized FePt NPs with average core diameters (d_{core}) of 1.9, 4.9, 5.7 and 9.3 nm have been selectively incorporated into a P2VP domain through hydrogen bonding interactions. The use of copolymer templates to selectively arrange the magnetic NPs guaranteed high MO performance with little trade-off in terms of scattering loss, providing a simple strategy to preparing functional materials for MO applications. As a result, Verdet constants of a 10 wt % loaded 4.9 nm FePt NP composite reached absolute magnitudes as high as ~ -6×10^4 °/T·m at 845 nm, as determined by FR measurements at room temperature. The dependence of the nanocomposite FR properties on particle diameter, loading (from 0.1 wt % to 10 wt %) and composite nanostructure were systematically investigated at four infrared wavelengths (845, 980, 1310 and 1550 nm).

In the future, the interpretation of NPs size or loading effects of films MO performance needed to be investigated in more details. Acknowledgement to the Norwood group, they propose to use number density and Figure of merit to discuss the results rather than use the NPs loading directly. From some perspective, this method is quite reasonable. NPs of different batches usually have various core weight percent and size, thus the comparison of loading including the organic ligand may be meaningless. On the other hand, the Figure of merit takes both Verdet constant and absorption

coefficient into the consideration, which gives a better evaluation of material integral performance. The preparation of films needs improvement as well. In the third project, a drop-cast method on flat stage was utilized. In spite of relatively roughness errors for most film, 2-3 samples still show poor control of films homogeneity (Table 4.2). To acquire consistent results, films using spin- or rod coating may be quite necessary in the next stage.

The MO materials are not limited to the nanospherical additives. Magnetic nanorods (NRs) become quite popular in electrical or optical material fabrication because their geometries introduce anisotropic electronic or ionic orientations or transportations.[10–12] Thanks to Lacroix group at Institut National des Sciences Appliquées de Toulouse (France), narrow distributed of high aspect ratio cobalt NRs have been synthesized (Figure 5.3). Integration of such kind of NRs into brush block copolymers or imprinting of these NRs ink as pillar structures are of great promise to generate materials of anisotropic FR response. Using the selective hydrogen bonding donor group ligands as stabilizer, these NRs have possibilities to be well dispersed in the polar solvent for subsequent blending.

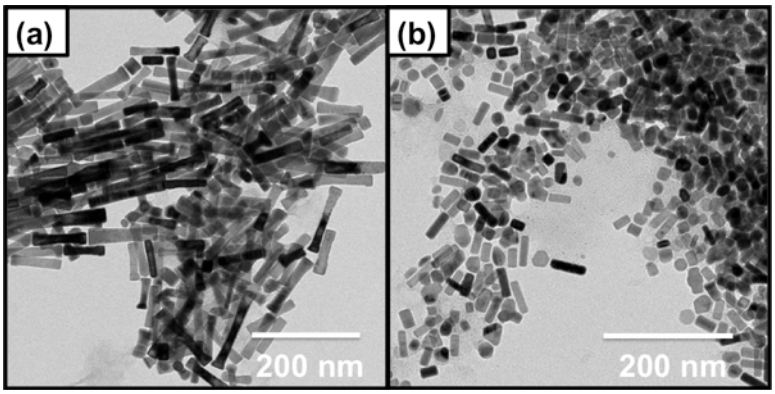

Figure 5.3 TEM images of cobalt NRs in ethanol suspension: (a) average core diameter 19 nm, length 100 nm and (b) average core diameter 14.5 nm, length 20-40 nm (courtesy to Lacroix group at Institut National des Sciences Appliquées de Toulouse, France).

5.4 References

(1) Song, D.-P.; Naik, A.; Li, S.; Ribbe, A.; Watkins, J. J. Rapid, Large-Area Synthesis of Hierarchical Nanoporous Silica Hybrid Films on Flexible Substrates. *J. Am. Chem. Soc.* **2016**, *138*, 13473–13476.

(2) Chen, L.; Zhang, X.; Liang, H.; Kong, M.; Guan, Q.; Chen, P.; Wu, Z.-Y.; Yu, S.-H. Synthesis of Nitrogen-Doped Porous Carbon Nanofibers as an Efficient Electrode Material for Supercapacitors. *ACS Nano* **2012**, *6*, 7092–7102.

(3) Han, J.; Zhang, L. L.; Lee, S.; Oh, J.; Lee, K.; Potts, J. R.; Ji, J.; Zhao, X.; Ruoff, R. S.; Park, S. Generation of B – Doped Graphene Nanoplatelets Using a Solution Process and Their Supercapacitor Applications. *ACS Nano* **2013**, *7*, 19–26.

(4) Shao, Y.; El-Kady, M. F.; Wang, L. J.; Zhang, Q.; Li, Y.; Wang, H.; Mousavi, M. F.; Kaner, R. B. Graphene-Based Materials for Flexible Supercapacitors. *Chem. Soc. Rev.* **2015**, *44*, 3639–3665.

(5) Yan, J.; Wang, Q.; Wei, T.; Fan, Z. Recent Advances in Design and Fabrication of Electrochemical Supercapacitors with High Energy Densities. *Adv. Energy Mater.* **2014**, *4*, 1300816.

(6) Yavitt, B. M.; Gai, Y.; Song, D.-P.; Winter, H. H.; Watkins, J. J. High Molecular Mobility and Viscoelasticity of Microphase-Separated Bottlebrush Diblock Copolymer Melts. *Macromolecules* **2017**, *50*, 396–405.

(7) Dalsin, S. J.; Hillmyer, M. A.; Bates, F. S. Linear Rheology of Polyolefin-Based Bottlebrush Polymers. *Macromolecules* **2015**, *48*, 4680–4691.

(8) Dalsin, S. J.; Hillmyer, M. A.; Bates, F. S. Molecular Weight Dependence of Zero-Shear Viscosity in Atactic Polypropylene Bottlebrush Polymers. *ACS Macro Lett.* **2014**, *3*, 423–427.

(9) Fredrickson, G. H.; Bates, F. S. Dynamics of Block Copolymers: Theory and Experiment. *Annu. Rev. Mater. Sci.* **1996**, *26*, 501–550.

(10) Burda, C.; Chen, X.; Narayanan, R.; El-Sayed, M. A. Chemistry and Properties of Nanocrystals of Different Shapes. *Chem. Rev.* **2005**, *105*, 1025–1102.

(11) Puntes, V. F.; Krishnan, K. M.; Alivisatos, A. P. Colloidal Nanocrystal Shape and Size Control: The Case of Cobalt. *Science.* **2001**, *291*, 2115–2117.

(12) Xia, Y.; Yang, P.; Sun, Y.; Wu, Y.; Mayers, B.; Gates, B.; Yin, Y.; Kim, F.; Yan, H. One-Dimensional Nanostructures: Synthesis, Characterization, and Applications. *Adv. Mater.* **2003**, *15*, 353–389.

BIBLIOGRAPHY

(1) Akimov, Y. A.; Koh, W. S.; Sian, S. Y.; Ren, S. Nanoparticle-Enhanced Thin Film Solar Cells: Metallic or Dielectric Nanoparticles? *Appl. Phys. Lett.* **2010**, *96*, 73111.

(2) Anderson, M. S. Enhanced Infrared Absorption with Dielectric Nanoparticles. *Appl. Phys. Lett.* **2003**, *83*, 2964–2966.

(3) Ando, K.; Saito, H.; Jin, Z.; Fukumura, T.; Kawasaki, M.; Matsumoto, Y.; Koinuma, H. Magneto-Optical Properties of ZnO-Based Diluted Magnetic Semiconductors. *J. Appl. Phys.* **2001**, *89*, 7284–7286.

(4) Armelles, G.; Cebollada, A.; García-Martín, A.; González, M. U. Magnetoplasmonics: Combining Magnetic and Plasmonic Functionalities. *Adv. Opt. Mater.* **2013**, *1*, 10–35.

(5) Bahuguna, R.; Mina, M.; Tioh, J. W.; Weber, R. J. Magneto-Optic-Based Fiber Switch for Optical Communications. *IEEE Trans. Magn.* **2006**, *42*, 3099–3101.

(6) Balazs, A. C.; Emrick, T.; Russell, T. P. Nanoparticle Polymer Composites: Where Two Small Worlds Meet. *Science.* **2006**, *314*, 1107–1110.

(7) Bang, J.; Jeong, U.; Ryu, D. Y.; Russell, T. P.; Hawker, C. J. Block Copolymer Nanolithography: Translation of Molecular Level Control to Nanoscale Patterns. *Adv. Mater.* **2009**, *21*, 4769–4792.

(8) Bates, F. S.; Fredrickson, G. H. Block Copolymer Thermodynamics: Theory and Experiment. *Annu. Rev. Phys. Chem.* **1990**, *41*, 525–557.

(9) Bates, F. S.; Fredrickson, G. H. Block Copolymers—Designer Soft Materials. *Phys. Today* **1999**, *52*, 32–38.

(10) Beecroft, L. L.; Ober, C. K. Nanocomposite Materials for Optical Applications. *Chem. Mater.* **1997**, *9*, 1302–1317.

(11) Belotelov, V. I.; Kreilkamp, L. E.; Akimov, I. A.; Kalish, A. N.; Bykov, D. A.; Kasture, S.; Yallapragada, V. J.; Gopal, A. V.; Grishin, A. M.; Khartsev, S. I.; *et al.* Plasmon-Mediated Magneto-Optical Transparency. *Nat. Commun.* **2013**, *4*, 2128.

(12) Belotelov, V. I.; Akimov, I. a.; Pohl, M.; Kotov, V. a; Kasture, S.; Vengurlekar, a S.; Gopal, A. V.; Yakovlev, D. R.; Zvezdin, A. K.; Bayer, M. Enhanced Magneto-Optical Effects in Magnetoplasmonic Crystals. *Nat. Nanotechnol.* **2011**, *6*, 370–376.

(13) Bockstaller, M. R.; Lapetnikov, Y.; Margel, S.; Thomas, E. L. Size-Selective Organization of Enthalpic Compatibilized Nanocrystals in Ternary Block Copolymer / Particle Mixtures. *J. Am. Chem. Soc.* **2003**, *125*, 5276–5277.

(14) Bockstaller, M. R.; Mickiewicz, R. A.; Thomas, E. L. Block Copolymer Nanocomposites: Perspectives for Tailored Functional Materials. *Adv. Mater.* **2005**, *17*, 1331–1349.

(15) Bockstaller, M. R.; Ryu, H. J.; Ojha, S.; Choi, J. 1D Periodic Bimetallic Superstructures by Co-Assembly of Ternary Block Copolymer/nanoparticle Blends. *J. Mater. Chem.* **2010**, *20*, 9339.

(16) Bolton, J.; Bailey, T. S.; Rzayev, J. Large Pore Size Nanoporous Materials from the Self-Assembly of Asymmetric Bottlebrush Block Copolymers. *Nano Lett.* **2011**, 998–1001.

(17) Bolton, J.; Rzayev, J. Tandem RAFT-ATRP Synthesis of Polystyrene - Poly(methyl Methacrylate) Bottlebrush Block Copolymers and Their Self-Assembly into Cylindrical Nanostructures. *ACS Macro Lett.* **2012**, *1*, 15–18.

(18) Bonanni, V.; Bonetti, S.; Pakizeh, T.; Pirzadeh, Z.; Chen, J.; Nogués, J.; Vavassori, P.; Hillenbrand, R.; Åkerman, J.; Dmitriev, A. Designer Magnetoplasmonics with Nickel Nanoferromagnets. *Nano Lett.* **2011**, *11*, 5333–5338.

(19) Borrelli, N. Faraday Rotation in Glasses. *J. Chem. Phys.* **1964**, *41*, 3289–3293.

(20) Brust, M.; Fink, J.; Bethell, D.; Schiffrin, D. J.; Kiely, C. Synthesis and Reactions of Functionalised Gold Nanoparticles. *J. Chem. Soc. Chem. Commun.* **1995**, 1655–1656.

(21) Brust, M.; Walker, M.; Bethell, D.; Schiffrin, D. J.; Whyman, R. Synthesis of Thiol-Derivatised Gold Nanoparticles in a Two-Phase Liquid-Liquid System. *J.Chem. Soc.,Chem. Commun.* **1994**, 801–802.

(22) Bublat, T.; Goll, D. Large-Area Hard Magnetic L10-FePt Nanopatterns by Nanoimprint Lithography. *Nanotechnology* **2011**, *22*, 315301.

(23) Burda, C.; Chen, X.; Narayanan, R.; El-Sayed, M. A. Chemistry and Properties of Nanocrystals of Different Shapes. *Chem. Rev.* **2005**, *105*, 1025–1102.

(24) Byun, M.; Bowden, N. B.; Lin, Z. Hierarchically Organized Structures Engineered from Controlled Evaporative Self-Assembly. *Nano Lett.* **2010**, *10*, 3111–3117.

(25) Caicedo, M.; Pascu, O.; Jos, A.; Fontcuberta, J.; Roig, A.; Herranz, G.; Uab, C.; Juana, C. S. Magnetophotonic Response of Three- Dimensional Opals. *ACS Nano* **2011**, *5*, 2957–2963.

(26) Cava, R. J. Dielectric Materials for Applications in Microwave Communications. *J. Mater. Chem.* **2001**, *11*, 54–62.

(27) Chen, L.; Zhang, X.; Liang, H.; Kong, M.; Guan, Q.; Chen, P.; Wu, Z.-Y.; Yu, S.-H. Synthesis of Nitrogen-Doped Porous Carbon Nanofibers as an Efficient Electrode Material for Supercapacitors. *ACS Nano* **2012**, *6*, 7092–7102.

(28) Cheng, C.; Khoshdel, E.; Wooley, K. L. ATRP from a Norbornenyl-Functionalized Initiator: Balancing of Complementary Reactivity for the Preparation of α-Norbornenyl Macromonomers/ω-Haloalkyl Macroinitiators. *Macromolecules* **2005**, *38*, 9455–9465.

(29) Cheng, C.; Qi, K.; Khoshdel, E.; Wooley, K. L. Tandem Synthesis of Core-Shell Brush Copolymers and Their Transformation to Peripherally Cross-Linked and Hollowed Nanostructures. *J. Am. Chem. Soc.* **2006**, *128*, 6808–6809.

(30) Cheng, J. Y.; Ross, C. A.; Smith, H. I.; Thomas, E. L. Templated Self-Assembly of Block Copolymers: Top-down Helps Bottom-Up. *Adv. Mater.* **2006**, *18*, 2505–2521.

(31) Chiu, J. J.; Kim, B. J.; Kramer, E. J.; Pine, D. J. Control of Nanoparticle Location in Block Copolymers. *J. Am. Chem. Soc.* **2005**, *127*, 5036–5037.

(32) Chiu, J. J.; Kim, B. J.; Yi, G. R.; Bang, J.; Kramer, E. J.; Pine, D. J. Distribution of Nanoparticles in Lamellar Domains of Block Copolymers. *Macromolecules* **2007**, *40*, 3361–3365.

(33) Choi, C. L.; Alivisatos, A. P. From Artificial Atoms to Nanocrystal Molecules: Preparation and Properties of More Complex Nanostructures. *Annu. Rev. Phys. Chem.* **2010**, *61*, 369–389.

(34) Choo, Y.; Mahajan, L. H.; Gopinadhan, M.; Ndaya, D.; Deshmukh, P.; Kasi, R. M.; Osuji, C. O. Phase Behavior of Polylactide-Based Liquid Crystalline Brushlike Block Copolymers. *Macromolecules* **2015**, *48*, 8315–8322.

(35) Chremos, A.; Theodorakis, P. E. Morphologies of Bottle-Brush Block Copolymers. *ACS Macro Lett.* **2014**, *3*, 1096–1100.

(36) Crassee, I.; Levallois, J.; Walter, A. L.; Ostler, M.; Bostwick, A.; Rotenberg, E.; Seyller, T.; van der Marel, D.; Kuzmenko, A. B. Giant Faraday Rotation in Single- and Multilayer Graphene. *Nat. Phys.* **2010**, *7*, 48–51.

(37) Cui, H.; Chen, Z.; Zhong, S.; Wooley, K. L.; Pochan, D. J. Block Copolymer Assembly via Kinetic Control. *Science.* **2007**, *317*, 647–650.

(38) Cui, H.; Wang, M.; Ren, W.; Liu, Y.; Zhao, Y. Highly Transparent Silica Monoliths Embedded with High Concentration Oxide Nanoparticles. *J. Sol-Gel Sci. Technol.* **2013**, *66*, 512–517.

(39) Dalsin, S. J.; Rions-Maehren, T. G.; Beam, M. D.; Bates, F. S.; Hillmyer, M. A.; Matsen, M. W. Bottlebrush Block Polmers: Quantitative Theory and Experiments. *ACS Nano* **2015**, *9*, 12233–12245.

(40) Dalsin, S. J.; Hillmyer, M. A.; Bates, F. S. Linear Rheology of Polyolefin-Based Bottlebrush Polymers. *Macromolecules* **2015**, *48*, 4680–4691.

(41) Dalsin, S. J.; Hillmyer, M. A.; Bates, F. S. Molecular Weight Dependence of Zero-Shear Viscosity in Atactic Polypropylene Bottlebrush Polymers. *ACS Macro Lett.* **2014**, *3*, 423–427.

(42) Daniel, M. C. M.; Astruc, D. Gold Nanoparticles: Assembly, Supramolecular Chemistry, Quantum-Size Related Properties and Applications toward Biology, Catalysis and Nanotechnology. *Chem. Rev.* **2004**, *104*, 293–346.

(43) Demir, V.; Gangopadhyay, P.; Norwood, R. A.; Peyghambarian, N. Faraday Rotation of Cobalt Ferrite Nanoparticle Polymer Composite Films at Cryogenic Temperatures. *Appl. Opt.* **2014**, *53*, 2087–2092.

(44) Discher, D. E.; Eisenberg, A. Polymer Vesicles. *Science.* **2002**, *297*, 967–973.

(45) Djalali, R.; Li, S. Y.; Schmidt, M. Amphipolar Core-Shell Cylindrical Brushes as Templates for the Formation of Gold Clusters and Nanowires. *Macromolecules* **2002**, *35*, 4282–4288.

(46) Domínguez, M.; Ortega, D.; Garitaonandía, J. S.; Litrán, R.; Barrera-Solano, C.; Blanco, E.; Ramírez-del-Solar, M. Magneto-Optic Faraday Effect in Maghemite Nanoparticles/silica Matrix Nanocomposites Prepared by the Sol-Gel Method. *J. Magn. Magn. Mater.* **2008**, *320*, e725–e729.

(47) Dong, Q.; Li, G.; Ho, C. L.; Faisal, M.; Leung, C. W.; Pong, P. W. T.; Liu, K.; Tang, B. Z.; Manners, I.; Wong, W. Y. A Polyferroplatinyne Precursor for the Rapid Fabrication of L1 0-FePt-Type Bit Patterned Media by Nanoimprint Lithography. *Adv. Mater.* **2012**, *24*, 1034–1040.

(48) Doormann, V.; Krumme, J. P.; Lenz, H. Optical and Magneto-Optical Tensor Spectra of Bismuth-Substituted Yttrium-Iron-Garnet Films. *J. Appl. Phys.* **1990**, *68*, 3544–3553.

(49) Dumestre, F.; Chaudret, B.; Amiens, C.; Respaud, M.; Fejes, P.; Renaud, P.; Zurcher, P. Unprecedented Crystalline Super-Lattices of Monodisperse Cobalt Nanorods. *Angew. Chemie Int. Ed.* **2003**, *42*, 5213–5216.

(50) Edrington, A. C.; Urbas, A. M.; Derege, P.; Chen, C. X.; Swager, T. M.; Hadjichristidis, N.; Xenidou, M.; Fetters, L. J.; Joannopoulos, J. D.; Fink, Y.; *et al.* Polymer-Based Photonic Crystals. *Adv. Mater.* **2001**, *13*, 421–425.

(51) Elghanian, R. Selective Colorimetric Detection of Polynucleotides Based on the Distance-Dependent Optical Properties of Gold Nanoparticles. *Science (80-.).* **2007**, *277*, 1078–1081.

(52) Enustun, B. V.; Turkevich, J. Coagulation of Colloidal Gold. *J. Am. Chem. Soc.* **1963**, *85*, 3317–3328.

(53) Fenyves, R.; Schmutz, M.; Horner, I. J.; Bright, F. V; Rzayev, J. Aqueous Self-Assembly of Giant Bottlebrush Block Copolymer Surfactants as Shape-Tunable Building Blocks. *J. Am. Chem. Soc.* **2014**, *136*, 7762–7770.

(54) Fredrickson, G. H.; Bates, F. S. Dynamics of Block Copolymers: Theory and Experiment. *Annu. Rev. Mater. Sci.* **1996**, *26*, 501–550.

(55) Fredrickson, G. H.; Bates, F. S. Dynamics of Block Copolymers: Theory and Experiment. *Annu. Rev. Mater. Sci.* **1996**, *26*, 501–550.

(56) Frey, N. A.; Peng, S.; Cheng, K.; Sun, S. Magnetic Nanoparticles: Synthesis, Functionalization, and Applications in Bioimaging and Magnetic Energy Storage. *Chem. Soc. Rev.* **2009**, *38*, 2532–2542.

(57) Frey, N. A.; Peng, S.; Cheng, K.; Sun, S. Magnetic Nanoparticles: Synthesis, Functionalization, and Applications in Bioimaging and Magnetic Energy Storage. *Chem. Soc. Rev.* **2009**, *38*, 2532–2542.

(58) Gangopadhyay, P.; Voorakaranam, R.; Lopez-Santiago, A.; Foerier, S.; Thomas, J.; Norwood, R. A.; Persoons, A.; Peyghambarian, N. Faraday Rotation Measurements on Thin Films of Regioregular Alkyl-Substituted Polythiophene Derivatives. *J. Phys. Chem. C* **2008**, *112*, 8032–8037.

(59) Gao, G.; Winterstein-Beckmann, A.; Surzhenko, O.; Dubs, C.; Dellith, J.; Schmidt, M. a.; Wondraczek, L. Faraday Rotation and Photoluminescence in Heavily Tb3+-Doped GeO2-B2O3-Al2O3-Ga2O3 Glasses for Fiber-Integrated Magneto-Optics. *Sci. Rep.* **2015**, *5*, 8942.

(60) Gao, H.; Matyjaszewski, K. Synthesis of Molecular Brushes By "grafting Onto" method: Combination of ATRP and Click Reactions. *J. Am. Chem. Soc.* **2007**, *129*, 6633–6639.

(61) García, R.; Ramírez-Del-Solar, M.; González-Leal, J. M.; Blanco, E.; Domínguez, M. Improving Magnetooptical Faraday Effect of Maghemite/silica Nanocomposites. *Mater. Chem. Phys.* **2015**, *154*, 1–9.

(62) Gerritsma, R.; Whitlock, S.; Fernholz, T.; Schlatter, H.; Luigjes, J. A.; Thiele, J. U.; Goedkoop, J. B.; Spreeuw, R. J. C. Lattice of Microtraps for Ultracold Atoms Based on Patterned Magnetic Films. *Phys. Rev. A* **2007**, *76*, 33408.

(63) Ghosh, S. K.; Pal, T. Interparticle Coupling Effect on the Surface Plasmon Resonance of Gold Nanoparticles: From Theory to Applications. *Chem. Rev.* **2007**, *107*, 4797–4862.

(64) Gollu, S. R.; Sharma, R.; Srinivas, G.; Kundu, S.; Gupta, D. Incorporation of SiO2 Dielectric Nanoparticles for Performance Enhancement in P3HT:PCBM Inverted Organic Solar Cells. *Org. Electron.* **2015**, *24*, 43–50.

(65) Gu, W.; Huh, J.; Hong, S. W.; Sveinbjornsson, B. R.; Park, C.; Grubbs, R. H.; Russell, T. P. Self-Assembly of Symmetric Brush Diblock Copolymers. *ACS Nano* **2013**, *7*, 2551–2558.

(66) Guo, Q.; Teng, X.; Yang, H. Fabrication of Magnetic FePt Patterns from Langmuir-Blodgett Films of Platinum-Iron Oxide Core-Shell Nanoparticles. *Adv. Mater.* **2004**, *16*, 1337–1341.

(67) Ha, J. M.; Wolf, J. H.; Hillmyer, M. A.; Ward, M. D. Polymorph Selectivity under Nanoscopic Confinement. *J. Am. Chem. Soc.* **2004**, *126*, 3382–3383.

(68) Hamley, I. W. Nanostructure Fabrication Using Block Copolymers. *Nanotechnology* **2003**, *14*, R39–R54.

(69) Han, J.; Zhang, L. L.; Lee, S.; Oh, J.; Lee, K.; Potts, J. R.; Ji, J.; Zhao, X.; Ruoff, R. S.; Park, S. Generation of B – Doped Graphene Nanoplatelets Using a Solution Process and Their Supercapacitor Applications. *ACS Nano* **2013**, *7*, 19–26.

(70) Hayashi, K.; Fujikawa, R.; Sakamoto, W.; Inoue, M.; Yogo, T. Synthesis of Highly Transparent Lithium Ferrite Nanoparticle/polymer Hybrid Self-Standing Films Exhibiting Faraday Rotation in the Visible Region. *J. Phys. Chem. C* **2008**, *112*, 14255–14261.

(71) Hillmyer, M. A. Effect of MolecularWeight and Temperature on Physical Aging of ThinGlassy Poly(2,6-Dimethyl-1,4-Phenylene Oxide) Films. *J. Polym. Sci. Part B Polym. Phys.* **2007**, *45*, 3249–3251.

(72) Ho, R. M.; Chiang, Y. W.; Tsai, C. C.; Lin, C. C.; Ko, B. T.; Huang, B. H. Three-Dimensionally Packed Nanohelical Phase in Chiral Block Copolymers. *J. Am. Chem. Soc.* **2004**, *126*, 2704–2705.

(73) Hu, M.; Chen, J.; Li, Z.-Y.; Au, L.; Hartland, G. V; Li, X.; Marquez, M.; Xia, Y. Gold Nanostructures: Engineering Their Plasmonic Properties for Biomedical Applications. *Chem. Soc. Rev.* **2006**, *35*, 1084–1094.

(74) Huang, K.; Ma, H.; Liu, J.; Huo, S.; Kumar, A.; Wei, T.; Zhang, X.; Jin, S.; Gan, Y.; Wang, P. C.; *et al.* Size-Dependent Localization and Pene- Tration of Ultrasmall Gold Nano- Particles in Cancer Cells, Multicellular Spheroids, and Tumors in Vivo. *ACS Nano* **2012**, *6*, 4483–4493.

(75) Huang, K.; Rzayev, J. Well-Defined Organic Nanotubes from Multicomponent Bottlebrush Copolymers. *J. Am. Chem. Soc.* **2009**, *131*, 6880–6885.

(76) Huang, X.; Jiang, P. Core-Shell Structured High- K Polymer Nanocomposites for Energy Storage and Dielectric Applications. *Adv. Mater.* **2015**, *27*, 546–554.

(77) Huh, J.; Ginzburg, V. V.; Balazs, A. C. Thermodynamic Behavior of Particle/diblock Copolymer Mixtures: Simulation and Theory. *Macromolecules* **2000**, *33*, 8085–8096.

(78) Huynh, W. U.; Dittmer, J. J.; Alivisatos, A. P. Hybrid Nanorod-Polymer Solar Cells. *Science.* **2002**, *295*, 2425–2427.

(79) Jackson, E. A.; Hillmyer, M. A. Nanoporous Membranes Derived from Block Copolymers: From Drug Delivery to Water Filtration. *ACS Nano* **2010**, *4*, 3548–3553.

(80) Jain, P. K.; Lee, K. S.; El-Sayed, I. H.; El-Sayed, M. A. Calculated Absorption and Scattering Properties of Gold Nanoparticles of Different Size, Shape, and Composition: Applications in Biological Imaging and Biomedicine. *J. Phys. Chem. B* **2006**, *110*, 7238–7248.

(81) Jain, P. K.; Xiao, Y.; Walsworth, R.; Cohen, A. E. Surface Plasmon Resonance Enhanced Magneto-Optics (SuPREMO): Faraday Rotation Enhancement in Gold-Coated Iron Oxide Nanocrystals. *Nano Lett.* **2009**, *9*, 1644–1650.

(82) Jain, P. K.; Huang, X.; El-Sayed, I. H.; El-Sayed, M. A. Review of Some Interesting Surface Plasmon Resonance-Enhanced Properties of Noble Metal Nanoparticles and Their Applications to Biosystems. *Plasmonics* **2007**, *2*, 107–118.

(83) Jana, N. R.; Chen, Y.; Peng, X. Size- and Shape-Controlled Magnetic (Cr , Mn , Fe , Co , Ni) Oxide Nanocrystals via a Simple and General Approach. *Chem. Mater.* **2004**, *16*, 3931–3935.

(84) Jana, N. R.; Gearheart, L.; Murphy, C. J. Seeding Growth for Size Control of 5-40 Nm Diameter Gold Nanoparticles. *Langmuir* **2001**, *17*, 6782–6786.

(85) Jang, S. G.; Khan, A.; Hawker, C. J.; Kramer, E. J. Morphology Evolution of PS-B-P2VP Diblock Copolymers via Supramolecular Assembly of Hydroxylated Gold Nanoparticles. *Macromolecules* **2012**, *45*, 1553–1561.

(86) Jang, S. G.; Kim, B. J.; Hawker, C. J.; Kramer, E. J. Bicontinuous Block Copolymer Morphologies Produced by Interfacially Active, Thermally Stable Nanoparticles. *Macromolecules* **2011**, *44*, 9366–9373.

(87) Jang, S. G.; Kramer, E. J.; Hawker, C. J. Controlled Supramolecular Assembly of Micelle-like Gold Nanoparticles in PS-B-P2VP Diblock Copolymers via Hydrogen Bonding. *J. Am. Chem. Soc.* **2011**, *133*, 16986–16996.

(88) Jang, S. G.; Kramer, E. J.; Hawker, C. J. Controlled Supramolecular Assembly of Micelle-like Gold Nanoparticles in PS-B-P2VP Diblock Copolymers via Hydrogen Bonding. *J. Am. Chem. Soc.* **2011**, *133*, 16986–16996.

(89) Jaramillo, T. F.; Baeck, S. H.; Cuenya, B. R.; McFarland, E. W. Catalytic Activity of Supported Au Nanoparticles Deposited from Block Copolymer Micelles. *J. Am. Chem. Soc.* **2003**, *125*, 7148–7149.

(90) Johnson, S. R.; Evans, S. D.; Brydson, R. Influence of a Terminal Functionality on the Physical Properties of Surfactant-Stabilized Gold Nanoparticles. *Langmuir* **1998**, *14*, 6639–6647.

(91) Joly, S.; Kane, R.; Radzilowski, L.; Wang, T.; Wu, A.; Cohen, R. E.; Thomas, E. L.; Rubner, M. F. Multilayer Nanoreactors for Metallic and Semiconducting Particles. *Langmuir* **2000**, *16*, 1354–1359.

(92) Kanaras, A. G.; Kamounah, F. S.; Schaumburg, K.; Kiely, C. J.; Brust, M. Thioalkylated Tetraethylene Glycol: A New Ligand for Water Soluble Monolayer Protected Gold Clusters. *Chem. Commun.* **2002**, 2294–2295.

(93) Kang, Y.; Walish, J. J.; Gorishnyy, T.; Thomas, E. L. Broad-Wavelength-Range Chemically Tunable Block-Copolymer Photonic Gels. *Nat. Mater.* **2007**, *6*, 957–960.

(94) Kao, J.; Thorkelsson, K.; Bai, P.; Rancatore, B. J.; Xu, T. Toward Functional Nanocomposites: Taking the Best of Nanoparticles, Polymers, and Small Molecules. *Chem. Soc. Rev.* **2013**, *42*, 2654–2678.

(95) Kao, J.; Thorkelsson, K.; Bai, P.; Rancatore, B. J.; Xu, T. Toward Functional Nanocomposites: Taking the Best of Nanoparticles, Polymers, and Small Molecules. *Chem. Soc. Rev.* **2013**, *42*, 2654–2678.

(96) Kawamoto, K.; Zhong, M.; Gadelrab, K. R.; Cheng, L.-C.; Ross, C. A.; Alexander-Katz, A.; Johnson, J. A. Graft-through Synthesis and Assembly of Janus Bottlebrush Polymers from A- Branch -B Diblock Macromonomers. *J. Am. Chem. Soc.* **2016**, *138*, 11501–11504.

(97) Khandpur, A. K.; Forster, S.; Bates, F. S.; Hamley, I. W.; Ryan, A. J.; Bras, W.; Almdal, K.; Mortensen, K. Polyisoprene-Polystyrene Diblock Copolymer Phase Diagram near the Order-Disorder Transition. *Macromolecules* **1995**, *28*, 8796–8806.

(98) Kim, B. J.; Bang, J.; Hawker, C. J.; Chiu, J. J.; Pine, J.; Jang, S. G.; Yang, S.; Kramer, E. J.; Pine, D. J. Creating Surfactant Nanoparticles for Block Copolymer Composites through Surface Chemistry. *Langmuir* **2007**, *23*, 12693–12703.

(99) Kim, B. J.; Bang, J.; Hawker, C. J.; Kramer, E. J. Effect of Areal Chain Density on the Location of Polymer-Modified Gold Nanoparticles in a Block Copolymer Template. *Macromolecules* **2006**, *39*, 4108–4114.

(100) Kim, D. H.; Sun, Z.; Russell, T. P.; Knoll, W.; Gutmann, J. S. Organic-Inorganic Nanohybridization by Block Copolymer Thin Films. *Adv. Funct. Mater.* **2005**, *15*, 1160–1164.

(101) Kim, J. U.; O'Shaughnessy, B. Morphology Selection of Nanoparticle Dispersions by Polymer Media. *Phys. Rev. Lett.* **2002**, *89*, 238301.

(102) Kim, S.; Yoo, M.; Kang, N.; Moon, B.; Kim, B. J.; Choi, S. H.; Kim, J. U.; Bang, J. Nanoporous Bicontinuous Structures via Addition of Thermally-Stable Amphiphilic Nanoparticles within Block Copolymer Templates. *ACS Appl. Mater. Interfaces* **2013**, *5*, 5659–5666.

(103) Kim, T. Y.; Yamazaki, Y.; Hirano, T. Magneto-Optical Properties of Bi-YIG Nanoparticle with Polymethacrylate Matrix Materials. *Phys. Status Solidi* **2004**, *241*, 1601–1604.

(104) Kim, Y.; Chen, H.; Alexander-Katz, A. Free Energy Landscape and Localization of Nanoparticles at Block Copolymer Model Defects. *Soft Matter* **2014**, *10*, 3284–3291.

(105) Klok, H. A.; Lecommandoux, S. Supramolecular Materials via Block Copolymer Self-Assembly. *Adv. Mater.* **2001**, *13*, 1217–1229.

(106) Kothari, R. Thesis: (I) Polymer Nanocomposites : Rheology and Processing for Mesoporous Materials and (II) Nanopatterning of Metal Oxides Using Soft Lithography, University of Massachusetts, Amherst, 2016.

(107) Ku, K. H.; Shin, J. M.; Kim, M. P.; Lee, C. H.; Seo, M. K.; Yi, G. R.; Jang, S. G.; Kim, B. J. Size-Controlled Nanoparticle-Guided Assembly of Block Copolymers for Convex Lens-Shaped Particles. *J. Am. Chem. Soc.* **2014**, *136*, 9982–9989.

(108) Kumar, G.; Mahajan, S. M. Wavelength Dispersion of Verdet Constant in E-Field Oriented Iron Oxide Doped Polymer Nanocomposites. *Proc. IEEE Sensors* **2013**, 6–8.

(109) Lacklison, D. E.; Scott, G. B.; Ralph, H. I.; Page, J. L. Garnets with High Magnetooptic Figures of Merit in the Visible Region. *IEEE Trans. Magn.* **1973**, *9*, 457–460.

(110) Lanson, D.; Ariura, F.; Schappacher, M.; Borsali, R.; Deffieux, A. Comb Copolymers with Polystyrene and Polyisoprene Branches: Effect of Block Topology on Film Morphology. *Macromolecules* **2009**, *42*, 3942–3950.

(111) Lanson, D.; Schappacher, M.; Borsali, R.; Deffieux, A. Synthesis of (Poly (Chloroethyl Vinyl Ether)-G-Polystyrene) Comb-B-(Poly (Chloropyran Ethoxy Vinyl Ether)- G-Polyisoprene) Comb Copolymers and Study of Hyper-Branched Micelle Formation in Dilute Solutions. *Macromolecules* **2007**, *40*, 5559–5565.

(112) Laulajainen, M.; Paturi, P.; Raittila, J.; Huhtinen, H.; Abrahamsen, A. B.; Andersen, N. H.; Laiho, R. BixY3-xFe5O12 Thin Films Prepared by Laser Ablation for Magneto-Optical Imaging of Superconducting Thin Films. *J. Magn. Magn. Mater.* **2004**, *279*, 218–223.

(113) Lee, H. Il; Matyjaszewski, K.; Sherryl, Y. S.; Sheiko, S. S. Hetero-Grafted Block Brushes with PCL and PBA Side Chains. *Macromolecules* **2008**, *41*, 6073–6080.

(114) Lee, J.-Y.; Thompson, R. B.; Jasnow, D.; Balazs, A. C. Entropically Driven Formation of Hierarchically Ordered Nanocomposites. *Phys. Rev. Lett.* **2002**, *89*, 155503.

(115) Leibler, L. Theory of Microphase Separation in Block Copolymers. *Macromolecules* **1980**, *13*, 1602–1617.

(116) Leong, W. L.; Lee, P. S.; Lohani, A.; Lam, Y. M.; Chen, T.; Zhang, S.; Dodabalapur, A.; Mhaisalkar, S. G. Non-Volatile Organic Memory Applications Enabled by in Situ Synthesis of Gold Nanoparticles in a Self-Assembled Block Copolymer. *Adv. Mater.* **2008**, *20*, 2325–2331.

(117) Lin, Y.; Daga, V. K.; Anderson, E. R.; Gido, S. P.; Watkins, J. J. Nanoparticle-Driven Assembly of Block Copolymers: A Simple Route to Ordered Hybrid Materials. *J. Am. Chem. Soc.* **2011**, *133*, 6513–6516.

(118) Link, S.; El-Sayed, M. a. Size and Temperature Dependence of the Plasmon Absorption of Colloidal Gold Nanoparticles. *J. Phys. Chem. B* **1999**, *103*, 4212–4217.

(119) Liu, X.; Xu, H.; Xia, H.; Wang, D. Rapid Seeded Growth of Monodisperse, Quasi-Spherical, Citrate- Stabilized Gold Nanoparticles via H 2 O 2 Reduction. *Langmuir* **2012**, 13720–13726.

(120) Lopes, W. A.; Jaeger, H. M. Hierarchical Self-Assembly of Metal Nanostructures on Diblock Copolymer Scaffolds. *Nature* **2001**, *414*, 735–738.

(121) Lopes, W. A.; Jaeger, H. M. Hierarchical Self-Assembly of Metal Nanostructures on Diblock Copolymer Scaffolds. *Nature* **2001**, *414*, 735–738.

(122) Lopez-Santiago, A.; Gangopadhyay, P.; Thomas, J.; Norwood, R. A.; Persoons, A.; Peyghambarian, N. Faraday Rotation in Magnetite-Polymethylmethacrylate Core-Shell Nanocomposites with High Optical Quality. *Appl. Phys. Lett.* **2009**, *95*, 143302.

(123) Lopez-Santiago, A.; Grant, H. R.; Gangopadhyay, P.; Voorakaranam, R.; Norwood, R. A.; Peyghambarian, N. Cobalt Ferrite Nanoparticles Polymer Composites Based All-Optical Magnetometer. *Opt. Mater. Express* **2012**, *2*, 978–986.

(124) Lu, A. H.; Salabas, E. L.; Schüth, F. Magnetic Nanoparticles: Synthesis, Protection, Functionalization, and Application. *Angew. Chemie - Int. Ed.* **2007**, *46*, 1222–1244.

(125) Lu, A. H.; Schmidt, W.; Matoussevitch, N.; Bönnemann, H.; Spliethoff, B.; Tesche, B.; Bill, E.; Kiefer, W.; Schüth, F. Nanoengineering of a Magnetically Separable Hydrogenation Catalyst. *Angew. Chemie - Int. Ed.* **2004**, *43*, 4303–4306.

(126) Lynd, N. A.; Hillmyer, M. A.; Matsen, M. W. Theory of Polydisperse Block Copolymer Melts: Beyond the Schulz-Zimm Distribution. *Macromolecules* **2008**, *41*, 4531–4533.

(127) Lynd, N. A.; Hillmyer, M. A. Influence of Polydispersity on the Self-Assembly of Diblock Copolymers. *Macromolecules* **2005**, *38*, 8803–8810.

(128) Lynd, N. A.; Hillmyer, M. A. Effects of Polydispersity on the Order - Disorder Transition in Block Copolymer Melts. *Macromolecules* **2007**, *40*, 8050–8055.

(129) Lynd, N. A.; Meuler, A. J.; Hillmyer, M. A. Polydispersity and Block Copolymer Self-Assembly. *Prog. Polym. Sci.* **2008**, *33*, 875–893.

(130) Majeed, H.; Shaheen, A.; Anwar, M. Complete Stokes Polarimetry of Magneto-Optical Faraday Effect in a Terbium Gallium Garnet Crystal at Cryogenic Temperatures. *Opt. Express* **2013**, *21*, 25148–25158.

(131) Mannion, A. M.; Bates, F. S.; MacOsko, C. W. Synthesis and Rheology of Branched Multiblock Polymers Based on Polylactide. *Macromolecules* **2016**, *49*, 4587–4598.

(132) Mikhaylovskiy, R. V.; Hendry, E.; Kruglyak, V. V. Ultrafast Inverse Faraday Effect in a Paramagnetic Terbium Gallium Garnet Crystal. *Phys. Rev. B* **2012**, *86*, 100405(R).

(133) Miyake, G. M.; Weitekamp, R. A.; Piunova, V. A.; Grubbs, R. H. Synthesis of Isocyanate-Based Brush Block Copolymers and Their Rapid Self-Assembly of Brush Block Copolymers to Photonic Crystals. *J. Am. Chem. Soc.* **2012**, *134*, 14249–14254.

(134) Miyake, G. M.; Piunova, V. A.; Weitekamp, R. A.; Grubbs, R. H. Precisely Tunable Photonic Crystals From Rapidly Self-Assembling Brush Block Copolymer Blends. *Angew. Chemie Int. Ed.* **2012**, *51*, 11246–11248.

(135) Moocarme, M.; Dominguez-Juarez, J. L.; Vuong, L. T. Ultra-Low-Intensity Magneto-Optical and Mechanical Effects in Metal Nanocolloids. *Nano Lett.* **2014**, *14*.

(136) Moreno, E. M.; Zayat, M.; Morales, M. P.; Serna, C. J.; Roig, A.; Levy, D. Prepartion of Narrow Size Distribution Superparamagnetic γ -Fe 2 O 3 Nanoparticles in a Sol-Gel Transparent SiO2 Matrix. *Langmuir* **2002**, *18*, 4972–4978.

(137) Mosallaei, H.; Sarabandi, K. Magneto-Dielectrics in Electromagnetics: Concept and Applications. *IEEE Trans. Antennas Propag.* **2004**, *52*, 1558–1567.

(138) Murphy, C. J.; Sau, T. K.; Gole, A. M.; Orendoff, C. J.; Gao, J.; Gou, L.; Hunyadi, S. E.; Li, T. Anisotropic Metal Nanoparticles: Synthesis, Assembly and Optical Applications. *J. Phys. Chem B.* **2005**, *109*, 13857–13870.

(139) Nandwana, V.; Nandwana, V.; Elkins, K. E.; Elkins, K. E.; Poudyal, N.; Poudyal, N.; Chaubey, G. S.; Chaubey, G. S.; Yano, K.; Yano, K.; *et al.* Size and Shape Control of Monodisperse FePt Nanoparticles. *J. Phys. Chem. C* **2007**, *111*, 4185–4189.

(140) Noro, A.; Higuchi, K.; Sageshima, Y.; Matsushita, Y. Preparation and Morphology of Hybrids Composed of a Block Copolymer and Semiconductor Nanoparticles via Hydrogen Bonding. *Macromolecules* **2012**, *45*, 8013–8020.

(141) Oskam, G. Metal Oxide Nanoparticles: Synthesis, Characterization and Application. *J. Sol-Gel Sci. Technol.* **2006**, *37*, 161–164.

(142) Pankhurst, Q. a.; Thanh, N. T. K.; Jones, S. K.; Dobson, J. Progress in Applications of Magnetic Nanoparticles in Biomedicine. *J. Phys. D. Appl. Phys.* **2009**, *42*, 224001.

(143) Paraffin, T.; Shell, C.; Balasubramanian, B.; Kraemer, K. L.; Reding, N. A.; Skomski, R.; Ducharme, S.; Sellmyer, D. J. Synthesis of Monodisperse Properties. *ACS Nano* **2010**, *4*, 1893–1900.

(144) Patton, D. L.; Advincula, R. C. A Versatile Synthetic Route to Macromonomers via RAFT Polymerization. *Macromolecules* **2006**, *39*, 8674–8683.

(145) Procedures, E.; Milli-q, M. Communications to the Editor. *Water* **1990**, 2415–2416.

(146) Puntes, V. F.; Krishnan, K. M.; Alivisatos, a P. Colloidal Nanocrystal Shape and Size Control: The Case of Cobalt. *Science.* **2001**, *291*, 2115–2117.

(147) Pustelny, S.; Wojciechowski, A.; Gring, M.; Kotyrba, M.; Zachorowski, J.; Gawlik, W. Magnetometry Based on Nonlinear Magneto-Optical Rotation with Amplitude-Modulated Light. *J. Appl. Phys.* **2008**, *103*, 63108.

(148) Q. A. Pankhurst; Connolly, J.; S. K. Jones; Dobson, J. Applications of Magnetic Nanoparticles in Biomedicine. *J. Phys. D Appl. Phys.* **2003**, *36*, R167–R181.

(149) Reddy, L. H.; Arias, J. L.; Nicolas, J.; Couvreur, P. Magnetic Nanoparticles: Design and Characerization,Toxicity and Biocompatibility,Pharmaceutical and Biomedical Applications. *Chem. Rev.* **2012**, *112*, 5818–5878.

(150) Rosa, C. De; Auriemma, F.; Girolamo, R. Di; Pepe, G. P.; Napolitano, T.; Scaldaferri, R. Enabling Strategies in Organic Electronics Using Ordered Block Copolymer Nanostructures. *Adv. Mater.* **2010**, *22*, 5414–5419.

(151) Runge, M. B.; Bowden, N. B. Synthesis of High Molecular Weight Comb Block Copolymers and Their Assembly into Ordered Morphologies in the Solid State. *J. Am. Chem. Soc.* **2007**, *129*, 10551–10560.

(152) Runge, M. B.; Dutta, S.; Bowden, N. B. Synthesis of Comb Block Copolymers by ROMP, ATRP, and ROP and Their Assembly in the Solid State. *Macromolecules* **2006**, *39*, 498–508.

(153) Runge, M. B.; Lipscomb, C. E.; Ditzler, L. R.; Mahanthappa, M. K.; Tivanski, A. V.; Bowden, N. B. Investigation of the Assembly of Comb Block Copolymers in the Solid State. *Macromolecules* **2008**, *41*, 7687–7694.

(154) Ruzette, A.-V.; Leibler, L. Block Copolymers in Tomorrow's Plastics. *Nat. Mater.* **2005**, *4*, 19–31.

(155) Rzayev, J. Synthesis of Polystyrene-Polylactide Bottlebrush Block Copolymers and Their Melt Self-Assembly into Large Domain Nanostructures. *Macromolecules* **2009**, *42*, 2135–2141.

(156) Sabir, T. S.; Rowland, L. K.; Milligan, J. R.; Yan, D.; Aruni, A. W.; Chen, Q.; Boskovic, D. S.; Kurti, R. S.; Perry, C. C. Mechanistic Investigation of Seeded Growth in Triblock Copolymer Stabilized Gold Nanoparticles. *Langmuir* **2013**, *29*, 3903–3911.

(157) Saha, S.; Pal, A.; Kundu, S.; Basu, S.; Pal, T. Photochemical Green Synthesis of Calcium-Alginate-Stabilized Ag and Au Nanoparticles and Their Catalytic Application to 4-Nitrophenol Reduction. *Langmuir* **2010**, *26*, 2885–2893.

(158) Sahagún, E.; Sáenz, J. J. Dielectric Nanoparticles: Polarizability Reveals Identity. *Nat. Mater.* **2012**, *11*, 748–749.

(159) Sakamoto, N.; Hashimoto, T. Order-Disorder Transition of Low Molecular Weight Polystyrene-Block-Polyisoprene. 1. SAXS Analysis of Two Characteristic Temperatures. *Macromolecules* **1995**, *28*, 6825–6834.

(160) Sarangi, S. N.; Hussain, A. M. P.; Sahu, S. N. Strong UV Absorption and Emission from L-Cysteine Capped Monodispersed Gold Nanoparticles. *Appl. Phys. Lett.* **2009**, *95*, 73109.

(161) Savchuk, A. I.; Stolyarchuk, I. D.; Makoviy, V. V; Savchuk, O. A. Magneto-Optical Faraday Rotation of Semiconductor Nanoparticles Embedded in Dielectric Matrices. *Appl. Opt.* **2014**, *53*, B22–B26.

(162) Savelev, R. S.; Yulin, A. V.; Krasnok, A. E.; Kivshar, Y. S. Solitary Waves in Chains of High-Index Dielectric Nanoparticles. *ACS Photonics* **2016**, *3*, 1869–1876.

(163) Schappacher, M.; Deffieux, A. From Combs to Comb-G-Comp Centipedes. *Macromolecules* **2005**, *38*, 7209–7213.

(164) Schmidt, M. A.; Wondraczek, L.; Lee, H. W.; Granzow, N.; Da, N.; Russell, P. S. J. Complex Faraday Rotation in Microstructured Magneto-Optical Fiber Waveguides. *Adv. Mater.* **2011**, *23*, 2681–2688.

(165) Shao, Y.; El-Kady, M. F.; Wang, L. J.; Zhang, Q.; Li, Y.; Wang, H.; Mousavi, M. F.; Kaner, R. B. Graphene-Based Materials for Flexible Supercapacitors. *Chem. Soc. Rev.* **2015**, *44*, 3639–3665.

(166) Sheiko, S. S.; Möller, M. Visualization of Macromolecules - A First Step to Manipulation and Controlled Response. *Chem. Rev.* **2001**, *101*, 4099–4123.

(167) Shimizu, T.; Teranishi, T.; Hasegawa, S.; Miyake, M. Size Evolution of Alkanethiol-Protected Gold Nanoparticles by Heat Treatment in the Solid State. *J. Phys. Chem. B* **2003**, *107*, 2719–2724.

(168) Shuto, Y.; Tanaka, M.; Sugahara, S. Magneto-Optical Properties of Group-IV Ferromagnetic Semiconductor Ge 1 − X Fe X Grown by Low-Temperature Molecular Beam Epitaxy. *J. Appl. Phys.* **2006**, *99*, 08D516.

(169) Silva, R. M.; Martins, H.; Nascimento, I.; Baptista, J. M.; Ribeiro, A. L.; Santos, J. L.; Jorge, P.; Frazão, O. Optical Current Sensors for High Power Systems: A Review. *Appl. Sci.* **2012**, *2*, 602–628.

(170) Sinev, I.; Iorsh, I.; Bogdanov, A.; Permyakov, D.; Komissarenko, F.; Mukhin, I.; Samusev, A.; Valuckas, V.; Kuznetsov, A. I.; Luk'yanchuk, B. S.; *et al.* Polarization Control over Electric and Magnetic Dipole Resonances of Dielectric Nanoparticles on Metallic Films. *Laser Photon. Rev.* **2016**, *8*, 1–8.

(171) Sinturel, C.; Vayer, M.; Morris, M.; Hillmyer, M. A. Solvent Vapor Annealing of Block Polymer Thin Films. *Macromolecules*, 2013, *46*, 5399–5415.

(172) Sohn, B. H.; Choi, J. M.; Yoo, S. Il; Yun, S. H.; Zin, W. C.; Jung, J. C.; Kanehara, M.; Hirata, T.; Teranishi, T. Directed Self-Assembly of Two Kinds of Nanoparticles Utilizing Monolayer Films of Diblock Copolymer Micelles. *J. Am. Chem. Soc.* **2003**, *125*, 6368–6369.

(173) Song, D. P.; Li, C.; Colella, N. S.; Lu, X.; Lee, J.-H.; Watkins, J. J. Thermally Tunable Metallodielectric Photonic Crystals from the Self-Assembly of Brush Block Copolymers and Gold Nanoparticles. *Adv. Opt. Mater.* **2015**, *3*, 1169–1175.

(174) Song, D. P.; Li, C.; Colella, N. S.; Xie, W.; Li, S.; Lu, X.; Gido, S.; Lee, J. H.; Watkins, J. J. Large-Volume Self-Organization of Polymer/Nanoparticle Hybrids with Millimeter-Scale Grain Sizes Using Brush Block Copolymers. *J. Am. Chem. Soc.* **2015**, *137*, 12510–12513.

(175) Song, D. P.; Lin, Y.; Gai, Y.; Colella, N. S.; Li, C.; Liu, X. H.; Gido, S.; Watkins, J. J. Controlled Supramolecular Self-Assembly of Large Nanoparticles in Amphiphilic Brush Block Copolymers. *J. Am. Chem. Soc.* **2015**, *137*, 3771–3774.

(176) Song, D.-P.; Li, C.; Li, W.; Watkins, J. J. Block Copolymer Nanocomposites with High Refractive Index Contrast for One-Step Photonics. *ACS Nano* **2016**, *10*, 1216–1223.

(177) Song, D.-P.; Lin, Y.; Gai, Y.; Colella, N. S.; Li, C.; Liu, X.-H.; Gido, S.; Watkins, J. J. Controlled Supramolecular Self-Assembly of Large Nanoparticles in Amphiphilic Brush Block Copolymers. *J. Am. Chem. Soc.* **2015**, *137*, 3771–3774.

(178) Song, D.-P.; Naik, A.; Li, S.; Ribbe, A.; Watkins, J. J. Rapid, Large-Area Synthesis of Hierarchical Nanoporous Silica Hybrid Films on Flexible Substrates. *J. Am. Chem. Soc.* **2016**, *138*, 13473–13476.

(179) Sperling, R. A.; Gil, P. R.; Zhang, F.; Zanella, M.; Parak, W. J. Biological Applications of Gold Nanoparticles. *Chem. Soc. Rev.* **2008**, *37*, 1896–1908.

(180) Spitalsky, Z.; Tasis, D.; Papagelis, K.; Galiotis, C. Carbon Nanotube-Polymer Composites: Chemistry, Processing, Mechanical and Electrical Properties. *Prog. Polym. Sci.* **2010**, *35*, 357–401.

(181) Stadler, B. J. H.; Mizumoto, T. Integrated Magneto-Optical Materials and Isolators: A Review. *IEEE Photonics J.* **2014**, *6*, 600215.

(182) Suits, J. C. Faraday and Kerr Effects in Magnetic Compounds. *IEEE Trans. Magn.* **1972**, *8*, 95–105.

(183) Sumerlin, B. S.; Neugebauer, D.; Matyjaszewski, K. Initiation Efficiency in the Synthesis of Molecular Brushes by Grafting from via Atom Transfer Radical Polymerization. *Macromolecules* **2005**, *38*, 702–708.

(184) Sun, S. C.B. Murray, D. Weller, L. Folks, A. M. Monodisperse FePt Nanoparticles and Ferromagnetic FePt Nanocrystal Superlattices. *Science.* **2000**, *287*, 1989–1992.

(185) Sun, S. Recent Advances in Chemical Synthesis, Self-Assembly, and Applications of FePt Nanoparticles. *Adv. Mater.* **2006**, *18*, 393–403.

(186) Sun, Y.; Xia, Y. Shape-Controlled Synthesis of Gold and Silver Nanoparticles. *Science.* **2002**, *298*, 2176–2179.

(187) Sung, S. Y.; Qi, X.; Stadler, B. J. H. Integrating Yttrium Iron Garnet onto Nongarnet Substrates with Faster Deposition Rates and High Reliability. *Appl. Phys. Lett.* **2005**, *87*, 121111.

(188) Sveinbjornsson, B. R.; Weitekamp, R. A.; Miyake, G. M.; Xia, Y.; Atwater, H. A.; Grubbs, R. H. Rapid Self-Assembly of Brush Block Copolymers to Photonic Crystals. *Proc. Natl. Acad. Sci.* **2012**, *109*, 14332–14336.

(189) Taccola, S.; Greco, F.; Zucca, A.; Innocenti, C.; Fernandez, C.; Campo, G.; Sangregorio, C.; Mazzolai, B.; Mattoli, V. Characterization of Free-Standing PEDOT:PSS/iron Oxide Nanoparticle Composite Thin Films and Application as Conformable Humidity Sensors. *ACS Appl. Mater. Interfaces* **2013**, *5*, 6324–6332.

(190) Takeuchi, H. The Faraday Effect of Bismuth Substituted Rare-Earth Iron Garnet. *Jpn. J. Appl. Phys.* **1975**, *14*, 1903–1910.

(191) Talapin, D. V.; Lee, J.-S.; Kovalenko, M. V.; Shevchenko, E. V. Prospects of Colloidal Nanocsrystals for Electronic and Optoelectronic Applications. *Chem. Rev.* **2010**, *110*, 389–458.

(192) Tang, C.; Dufour, B.; Kowalewski, T.; Matyjaszewski, K. Synthesis and Morphology of Molecular Brushes with Polyacrylonitrile Block Copolymer Side Chains and Their Conversion into Nanostructured Carbons. *Macromolecules* **2007**, *40*, 6199–6205.

(193) Tang, C.; Lennon, E. M.; Fredrickson, G. H.; Kramer, E. J.; Hawker, C. J. Evolution of Block Copolymer Lithography to Highly Ordered Square Arrays. *Science.* **2008**, *322*, 429–432.

(194) Tang, Z.; Kotov, N. A. One-Dimensional Assemblies of Nanoparticles: Preparation, Properties, and Promise. *Adv. Mater.* **2005**, *17*, 951–962.

(195) Tartaj, P.; González-Carreño, T.; Serna, C. J. Single-Step Nanoengineering of Silica Coated Maghemite Hollow Spheres with Tunable Magnetic Properties. *Adv. Mater.* **2001**, *13*, 1620–1624.

(196) Thompson, R. B.; Ginzburg, V. V; Matsen, M. W.; Balazs, a C. Predicting the Mesophases of Copolymer-Nanoparticle Composites. *Science.* **2001**, *292*, 2469–2472.

(197) Thorkelsson, K.; Mastroianni, A. J.; Ercius, P.; Xu, T. Direct Nanorod Assembly Using Block Copolymer-Based Supramolecules. *Nano Lett.* **2012**, *12*, 498–504.

(198) Thurn-Albrecht, T.; Schotter, J.; Kästle, G. a; Emley, N.; Shibauchi, T.; Krusin-Elbaum, L.; Guarini, K.; Black, C. T.; Tuominen, M. T.; Russell, T. P. Ultrahigh-Density Nanowire Arrays Grown in Self-Assembled Diblock Copolymer Templates. *Science.* **2000**, *290*, 2126–2129.

(199) Tyagi, S.; Lee, J. Y.; Buxton, G. a; Balazs, A. C. Using Nanocomposite Coatings To Heal Surface Defects. *Macromolecules* **2004**, *37*, 9160–9168.

(200) Veis, M.; Liskova, E.; Antos, R.; Visnovsky, S.; Kumar, N.; Misra, D. S.; Venkataramani, N.; Prasad, S.; Krishnan, R. Polar and Longitudinal Magneto-Optical Spectroscopy of Bismuth Substituted Yttrium Iron Garnet Films Grown by Pulsed Laser Deposition. *Thin Solid Films* **2011**, *519*, 8041–8046.

(201) Verduzco, R.; Li, X.; Pesek, S. L.; Stein, G. E. Structure, Function, Self-Assembly, and Applications of Bottlebrush Copolymers. *Chem. Soc. Rev.* **2015**, *44*, 2405–2420.

(202) Villaverde, A. B.; Donatti, D. A.; Bozinis, D. G. Terbium Gallium Garnet Verdet Constant Measurements with Pulsed Magnetic Field. *J. Phys. C Solid State Phys.* **1978**, *11*, L495–L498.

(203) Wang, L.; Clavero, C.; Huba, Z.; Carroll, K. J.; Carpenter, E. E.; Gu, D.; Lukaszew, R. A. Plasmonics and Enhanced Magneto-Optics in Core− Shell Co− Ag Nanoparticles. *Nano Lett.* **2011**, *11*, 1237–1240.

(204) Wang, T. C.; Rubner, M. F.; Cohen, R. E. Polyelectrolyte Multilayer Nanoreactors for Preparing Silver Nanoparticle Composites:Controlling Metal Concentration and Nanoparticle Size. *Langmuir* **2002**, *18*, 3370–3375.

(205) Wang, X. Thesis: Functional Nanocomposites from Self-Assembly of Block Copolymers with Nanoparticles, University of Massachusetts, Amherst, 2014.

(206) Wang, X.; Tilley, R. D.; Watkins, J. J. Simple Ligand Exchange Reactions Enabling Excellent Dispersibility and Stability of Magnetic Nanoparticles in Polar Organic, Aromatic, and Protic Solvents. *Langmuir* **2014**, *30*, 1514–1521.

(207) Wei, Q.; Lin, Y.; Anderson, E. R.; Briseno, A. L.; Gido, S. P.; Watkins, J. J. Additive-Driven Assembly of Block Copolymer-Nanoparticle Hybrid Materials for Solution Processable Floating Gate Memory. *ACS Nano* **2012**, *6*, 1188–1194.

(208) Xia, Y.; Yang, P.; Sun, Y.; Wu, Y.; Mayers, B.; Gates, B.; Yin, Y.; Kim, F.; Yan, H. One-Dimensional Nanostructures: Synthesis, Characterization, and Applications. *Adv. Mater.* **2003**, *15*, 353–389.

(209) Xia, Y.; Kornfield, J. A.; Grubbs, R. H. Efficient Syntheses of Brush Polymers via Living Ring Opening Metathesis Polymerization of Macromonomers. *Macromolecules* **2009**, *42*, 3761–3766.

(210) Xia, Y.; Olsen, B. D.; Kornfield, J. A.; Grubbs, R. H. Efficient Synthesis of Narrowly Dispersed Brush Copolymers and Study of Their Assemblies: The Importance of Side Chain Arrangement. *J. Am. Chem. Soc.* **2009**, *131*, 18525–18532.

(211) Xiang, J.; Lu, W.; Hu, Y.; Wu, Y.; Yan, H.; Lieber, C. M. Ge/Si Nanowire Heterostructures as High-Performance Field-Effect Transistors. *Nature* **2006**, *441*, 489–493.

(212) Yan, J.; Wang, Q.; Wei, T.; Fan, Z. Recent Advances in Design and Fabrication of Electrochemical Supercapacitors with High Energy Densities. *Adv. Energy Mater.* **2014**, *4*, 1300816.

(213) Yang, K.; Huang, X.; Huang, Y.; Xie, L.; Jiang, P. Fluoro-Polymer@BaTiO3 Hybrid Nanoparticles Prepared via RAFT Polymerization: Toward Ferroelectric Polymer Nanocomposites with High Dielectric Constant and Low Dielectric Loss for Energy Storage Application. *Chem. Mater.* **2013**, *25*, 2327–2338.

(214) Yang, X.; Liu, C.; Ahner, J.; Yu, J.; Klemmer, T.; Johns, E.; Weller, D. Fabrication of FePt Nanoparticles for Self-Organized Magnetic Array. *J. Vac. Sci. Technol. B* **2004**, *22*, 31–34.

(215) Yao, L.; Lu, X.; Chen, S.; Watkins, J. J. Formation of Helical Phases in Achiral Diblock Copolymers Induced by Small Chiral Additives. *Macromolecules* **2014**, *47*, 6547–6553.

(216) Yao, L.; Lin, Y.; Watkins, J. J. Ultrahigh Loading of Nanoparticles into Ordered Block Copolymer Composites. *Macromolecules* **2014**, *47*, 1844–1849.

(217) Yavitt, B. M.; Gai, Y.; Song, D.-P.; Winter, H. H.; Watkins, J. J. High Molecular Mobility and Viscoelasticity of Microphase-Separated Bottlebrush Diblock Copolymer Melts. *Macromolecules* **2017**, *50*, 396–405.

(218) Ye, T.; Chen, X.; Fan, X.; Shen, Z. Ordered Gold Nanoparticle Arrays Obtained with Supramolecular Block Copolymers. *Soft Matter* **2013**, *9*, 4715–4724.

(219) Yeh, S.; Wei, K.; Sun, Y.; Jeng, U.; Liang, K. S. Morphological Transformation of PS-B-PEO Diblock Copolymer by Selectively Dispersed Collidal CdS Quantum Dots. *Macromolecules* **2003**, *36*, 7903–7907.

(220) Yogo, T.; Nakamura, T.; Sakamoto, W.; Hirano, S. Synthesis of Transparent Magnetic Particle/organic Hybrid Film Using Iron-Organics. *J. Mater. Res.* **2000**, *15*, 2114–2120.

(221) Yoo, M.; Kim, S.; Bang, J. Design and Fabrication of Thermally Stable Nanoparticles for Well-Defined Nanocomposites. *J. Polym. Sci. Part B Polym. Phys.* **2013**, *51*, 494–507.

(222) Yumoto, G.; Yoo, J. Y.; Matsunaga, R.; Tanabe, S.; Hibino, H.; Morimoto, T.; Aoki, H.; Shimano, R. Quantum Faraday and Kerr Rotations in Graphene. *Nat. Commun.* **2013**, *4*, 1841–1846.

(223) Zayat, M.; Del Monte, F.; Del Puerto Morales, M.; Rosa, G.; Guerrero, H.; Serna, C. J.; Levy, D. Highly Transparent Fe2O3/Vycor-Glass Magnetic Nanocomposites Exhibiting Faraday Rotation. *Adv. Mater.* **2003**, *15*, 1809–1812.

(224) Zhang, M.; Estournès, C.; Bietsch, W.; Müller, A. H. E. Superparamagnetic Hybrid Nanocylinders. *Adv. Funct. Mater.* **2004**, *14*, 871–882.

(225) Zhang, M.; Drechsler, M.; Müller, A. H. E. Template-Controlled Synthesis of Wire-Like Cadmium Sulfide Nanoparticle Assemblies within Core-Shell Cylindrical Polymer Brushes. *Chem. Mater.* **2004**, *16*, 537–543.

(226) Zhang, M.; Müller, A. H. E. Cylindrical Polymer Brushes. *J. Polym. Sci. Part A Polym. Chem.* **2005**, *43*, 3461–3481.

(227) Zhao, Y.; Thorkelsson, K.; Mastroianni, A. J.; Schilling, T.; Luther, J. M.; Rancatore, B. J.; Matsunaga, K.; Jinnai, H.; Wu, Y.; Poulsen, D.; *et al.* Small-Molecule-Directed Nanoparticle Assembly towards Stimuli-Responsive Nanocomposites. *Nat. Mater.* **2009**, *8*, 979–985.

(228) Zhou, Z. H.; Xue, J. M.; Chan, H. S. O.; Wang, J. Transparent Magnetic Composites of ZnFe2O4 Nanoparticles in Silica. *J. Appl. Phys.* **2001**, *90*, 4169–4174.

(229) Ziolo, R. F.; Giannelis, E. P.; Weinstein, B. A.; O'Horo, M. P.; Ganguly, B. N.; Mehrota, V.; Russel, M. W.; Huffman, D. R. Matrix-Mediated Synthesis of Nanocrystalline Y-Fe3O4: A New Optically Transparente Magnetic Material. *Science.* **1992**, *257*, 219–223.

(230) Zu, P.; Chan, C. C.; Koh, G. W.; Lew, W. S.; Jin, Y.; Liew, H. F.; Wong, W. C.; Dong, X. Enhancement of the Sensitivity of Magneto-Optical Fiber Sensor by Magnifying the Birefringence of Magnetic Fluid Film with Loyt-Sagnac Interferometer. *Sensors Actuators, B Chem.* **2014**, *191*, 19–23.

(231) Zvezdin, A. K.; Kotov, V. A. *Studies in Condensed Matter Physics. Mordern Magnetooptics and Magnetooptical Materials*; Coey, J. M. D.; Tilley, D. R., Eds.; Institute of Physics Publishing: London, 1997.

(232) https://en.wikipedia.org/wiki/Faraday_effect.